

# UC Berkeley

## UC Berkeley Electronic Theses and Dissertations

### Title

Microengineered Platforms For Assessing Cell-Cell Communication And Single-Cell Influences On Adult Neural Stem Cell Fate

### Permalink

<https://escholarship.org/uc/item/1v56p22g>

### Author

Chen, Siyu

### Publication Date

2012

Peer reviewed|Thesis/dissertation

Microengineered Platforms For Assessing Cell-Cell Communication and  
Single-Cell Influences on Adult Neural Stem Cell Fate

by

Siyu Chen

A dissertation submitted in partial satisfaction of the

requirements for the degree of

Joint Doctor of Philosophy

with the University of California, San Francisco

in

Bioengineering

in the

Graduate Division

of the

University of California, Berkeley

Committee in charge:

Professor Michel M. Maharbiz, Chair

Professor David V. Schaffer

Professor Henk Roelink

Professor Zev Gartner, UCSF

Spring 2012





# Microengineered Platforms For Assessing Cell-Cell Communication and Single-Cell Influences on Adult Neural Stem Cell Fate

By

Siyu Chen

Joint Doctor of Philosophy in Bioengineering

University of California, Berkeley

University of California, San Francisco

Professor Michel M. Maharbiz, Chair

The signaling environment experienced by a single cell is highly dependent on its interactions with its neighbors, which may secrete locally acting factors or act via membrane bound receptor-ligand systems. Stem cells are particularly sensitive to these signals, which act in concert to regulate self-renewal and discrete transitions into distinct fates. In the case of the adult neural stem cell, decades of *in vivo* and *in vitro* work have illustrated specific roles for different types of niche cells and some of the molecular mediators of their instructive roles. However, these studies have not investigated the strengths of these fate-inducing or fate-repressing cues as presented by single neighboring cells at endogenous expression levels. In this work, we have developed and applied microengineered tools to examine the transmission of signals between small populations of cells and to assess their impact on neural stem cell fate.

First, we measured gap junction coupling between cells by using microfluidic flow focusing of calcein/AM dye and timelapse imaging to measure the dynamics of dye transfer through gap-junction coupled glioma cells. Secondly, we developed single-cell micropatterning methods to investigate the potential for single neural progenitor cells to influence their neighbor's fate. Size-matched circular and hourglass shaped polystyrene microwells achieved up to 80% efficiency in capturing single and paired neural progenitor cells, a large improvement over Poisson-distributed random seeding. In conjunction, we also developed a method to fabricate and align PDMS meshes to corral patterned cells into non-connected arenas so that single cells and cell pairs can be grown in isolation for six days before immunostaining for fate markers. Lastly, we applied a simplified micropatterning technique in conjunction with automated high-throughput imaging to enforce persistent interactions between initially patterned cells. We discovered that single neural progenitor cells can significantly bias their neighbor's fate in mixed differentiation medium. Although the initial number of cells on a pattern did not affect the overall distribution of different fates, we saw reduced fate asymmetry on patterns with initially paired cells, indicating that single cells may

be inducing a similar fate in their neighbors, or repressing differentiation. By tracking cell populations on micropatterns on every day of the experiment via brightfield imaging, we also ascertained that the initial patterning state was maintained for approximately two days, suggesting that fate specification or repression occurred early in the process. Our discovery that a single as-yet undifferentiated neural stem cell can significantly bias its neighbor's fate paves the road for future work in elucidating how conflicting signals from various types of niche cells are arbitrated in a single recipient stem cell.

For my laolao

Ezekiel excoriates as false prophets those who have “not gone up into the gaps.” The gaps are the thing. The gaps are the spirit’s one home, the altitudes and latitudes so dazzlingly spare and clean that the spirit can discover itself for the first time like a once-blind man unbound. The gaps are the clifts in the rock where you cower to see the back parts of God; they are the fissures between mountains and cells the wind lances through, the ice narrowing fjords splitting the cliffs of mystery. Go up into the gaps. Stalk the gaps. Squeak into a gap in the soil and turn to unlock - more than a maple - a universe.

-Annie Dillard, *Pilgrim at Tinker Creek*

# Table of Contents

---

List of Figures .....	v
List of Equations.....	vii
Introduction .....	viii
Acknowledgements .....	ix

<b>CHAPTER 1 : BACKGROUND .....</b>	<b>1</b>
1.1. STEM CELL BIOLOGY .....	1
1.1.1 Modes of Interactions in the Stem Cell Niche: Lessons From an Invertebrate Model .....	3
1.1.2 Adult Neural Stem Cells and Their Niche .....	5
1.2. MICROTECHNOLOGIES FOR MODULATING CELL-TO-CELL SIGNALING .....	7
1.2.1 Static 2D Micropatterns Reveal Autoregulatory Signaling Loops .....	9
1.2.2 Investigating Morphogenesis in Patterned 3D Gels.....	9
1.2.3 Removing Paracrine Factors By Flow.....	10
1.2.4 Biomimetic Co-Cultures in Configurable Devices.....	10
1.2.5 Micropatterning With Single Cell Resolution .....	11
1.3 REFERENCES .....	13
<b>CHAPTER 2 : NON-INVASIVE MICROFLUIDIC GAP JUNCTION ASSAY .....</b>	<b>19</b>
2.1 INTRODUCTION.....	19
2.2 PRINCIPLE OF OPERATION .....	22
2.3. METHODS.....	22
2.3.1 Microfluidics Device Fabrication .....	22
2.3.2 Cell Culture.....	23
2.3.3 Device Operation.....	23
2.3.4 Fluorescence Imaging and Data Analysis .....	24
2.4. RESULTS.....	24
2.4.1 Device Design, Simulation, and Characterization .....	24
2.4.2 Dye Transfer in Cx43+ C6 Glioma .....	26
2.5 DISCUSSION .....	30
2.5 REFERENCES .....	32
<b>CHAPTER 3 : TRAP AND CORRAL: A TWO-STEP APPROACH FOR CONSTRUCTING AND CONSTRAINING DYNAMIC CELL CONTACT EVENTS IN DIFFERENTIATING PROGENITOR CELL POPULATIONS.....</b>	<b>34</b>
3.1 INTRODUCTION.....	34
3.2. MATERIALS AND METHODS .....	36
3.2.1 Polystyrene Microwell Fabrication .....	36
3.2.2 Alignment Jig Fabrication and Assembly .....	37
3.2.3 Mesh Fabrication .....	38
3.2.4 Cell Culture.....	38
3.2.5 Trap and Corral Experimental Procedure .....	39
3.2.6 Timelapse Microscopy.....	40
3.2.7 Data Processing.....	40
3.2.8 Scanning Electron Microscopy.....	40
3.2.9 Immunostaining .....	40
3.3. RESULTS.....	41

3.3.1 Material Choice in Rapid Prototyping .....	41
3.3.2 Microwell Traps Achieve High Efficiency in Cell Pairing .....	44
3.3.3 Outward Migration in NPC Differentiation Medium .....	44
3.3.4 Fabrication of PDMS Mesh With Through-Holes .....	46
3.3.5 PDMS Sealing Under Liquids.....	48
3.3.6 Trap and Corral.....	48
3.4 CONCLUSIONS.....	51
3.5 REFERENCES .....	52
<b>CHAPTER 4 : MICROPATTERNING PERSISTENT INTERACTIONS BETWEEN NEURAL PROGENITOR CELLS REVEALS SINGLE CELL INFLUENCES ON CELL FATE .....</b>	<b>54</b>
4.1 INTRODUCTION.....	54
4.2. MATERIALS AND METHODS .....	55
4.2.1 Cell Culture.....	55
4.2.2 Imaging .....	56
4.2.3 Micropatterning .....	56
4.2.4 Cell Seeding on Micropatterns.....	57
4.2.5 Immunostaining .....	58
4.2.6 Automated and Manual Image Processing.....	58
4.3. RESULTS.....	60
4.3.1 Image Processing.....	60
4.3.2 Neuronal Differentiation Increased at Higher Densities.....	62
4.3.3 Hippocampal Astrocytes Increase Astrocyte Differentiation.....	63
4.3.4 Population Dynamics of Micropatterned NPCs.....	63
4.3.5 Initial Cell Number Does Not Affect Overall Fate Distributions In Micropatterned NPCs	64
4.3.6 Paired Cells Yield Unexpectedly Low Fate Asymmetry .....	65
4.3.7 Single Hippocampal Astrocytes Promote Neuronal Differentiation in Single NPCs.....	67
4.4 DISCUSSION .....	68
4.5 REFERENCES .....	71
<b>CHAPTER 5 : CONCLUDING REMARKS .....</b>	<b>74</b>
REFERENCES.....	77
<b>APPENDIX A – MATLAB CODE .....</b>	<b>79</b>
A-1 RESHIST .....	79
A-2 CELLSTACKCOUNTER.....	82
<b>APPENDIX B – ANNOTATED AUTOCAD DESIGNS FOR CHAPTER 3 .....</b>	<b>89</b>

# List of Figures

---

## CHAPTER 1

*Figure 1-1. Overview of different modes of cell-cell interactions. .... 2*

*Figure 1-2. Contrasting the Drosophila ovary niche with the adult neural stem cell niche. \_ 4*

*Figure 1-3. Microscale technologies for cell biology. .... 8*

## CHAPTER 2

*Figure 2-1. Methods for loading dye into a subset of contacting cells. .... 20*

*Table 1. Advantages and limitations of gap junction assays. .... 23*

*Figure 2-2. Dye focusing in bare devices and over confluent cells. .... 27*

*Figure 2-4 Fluorescence intensity profiles over time. .... 27*

*Figure 2-5 Dye spread and effective diffusivity. .... 29*

*Figure 2-6 Dose response of 18 $\alpha$ -GA and washout experiment. .... 29*

*Figure 2-7 Further evidence that dye transfer is indeed gap junction mediated. .... 30*

## CHAPTER 3

*Figure 3-1 Experimental scheme. .... 35*

*Figure 3-2 The fabrication of microwells in polystyrene. .... 37*

*Figure 3-3 Trap and corral alignment jig. .... 42*

*Figure 3-4 Microwells achieve high efficiencies in trapping single and paired cells. .... 43*

*Figure 3-5 Outward migration from microwells in mixed differentiation media. .... 45*

*Figure 3-6 PDMS mesh fabrication. .... 46*

*Figure 3-7 Migration of cell pairs. .... 50*

*Figure 3-8 Immunostained cells in corrals. .... 51*



## CHAPTER 4

<i>Figure 4-1 Micropattern generation.....</i>	<i>57</i>
<i>Figure 4-2 CellProfiler segmentation. ....</i>	<i>59</i>
<i>Figure 4-3 Training classifiers in the CellProfiler Analyst interface.....</i>	<i>60</i>
<i>Figure 4-4 Individual patterns during 5 days of brightfield imaging and after immunostaining. ....</i>	<i>61</i>
<i>Figure 4-5 Control cultures show differentiation dependence on NPC density and astrocyte co-culture.....</i>	<i>62</i>
<i>Figure 4-6 Proliferation rate depends on initial number of cells and cell fate propensity. ..</i>	<i>64</i>
<i>Figure 4-7 Single NPCs differentiating into Tuj1+ neurons (top) or GFAP+ astrocytes.....</i>	<i>65</i>
<i>Figure 4-8 Fate distributions of micropatterned NPCs.....</i>	<i>66</i>
<i>Figure 4-9 Patterns with mixed populations of NPCs and hippocampal astrocytes.....</i>	<i>68</i>

## List of Equations

---

Equation 2-1 – Channel Resistance.....	24
Equation 4-1 – Population Growth ... ..	63
Equation 4-2 – Probability of Asymmetric Fate for Two Founder Cells.....	65
Equation 4-3 - Probability of Asymmetric Fate for Three Founder Cells .....	65
Equation 4-4 - Probability of Asymmetric Fate for Four Founder Cells .....	65

## Introduction

---

Stem cell biology holds enormous promise for therapeutic medicine in the 21<sup>st</sup> century. The ability to isolate and grow pluripotent stem cells and then differentiate them into tissues for replacement therapy will pave the way for the treatment of previously incurable diseases. However, the environment that a stem cell natively or ectopically occupies is chemically complex and architecturally intricate. Understanding the “niche” of signals and cells that regulate a stem cell’s behavior is integral to constructing a picture of how normal development progresses, how signaling dysregulation can give rise to pathologies and cancers, and how implanted cells and tissues may be regulated and integrated within their new environment.

The major motivation behind this work is to develop and apply microtechnologies that measure and control local cell-cell interactions that are important for stem cell biology. Because microtechnologies exhibit spatial resolution on the size scale of individual cells, they provide attractive tools for measuring the transmission of signals from cell to cell, and constraining cell-cell interactions for extended periods.

In the first chapter, I will discuss some major concepts behind stem cell biology, and specifically the biology of adult neural stem cells and their niche signals. In the second half of this chapter, I will also provide an overview of existing microtechnology and its capabilities and limitations. Chapter 2 presents work on a microfluidic device for assaying gap junction coupling between cells cultured in monolayers by using hydrodynamic focusing over cells. Although this work was done in transformed glioma cells (C6), not stem cells, the principles behind it can be extended to any cell type. Chapter 3 presents the design and fabrication of an alignment device for trapping and *in situ* corralling defined numbers of neural stem cells. This technology was developed to understand whether intercellular feedback between differentiating cells could bias cell fate, driving fate asymmetry. The microwell trapping described here achieved up to 80% efficiency in cell pairing, a dramatic improvement on Poisson distributed random-seeding. In Chapter 4, I discuss our efforts in using a simpler micropatterning method in conjunction with automated high-throughput imaging to assess whether single differentiating cells exert feedback on their neighbors to instruct their fate. My results show that paired NPCs in the process of differentiating exhibit reduced fate asymmetry, indicating that single cells can exert lateral fate induction or repression of differentiation. I conclude in Chapter 5 with a brief discussion on how open questions regarding stem cell integration of conflicting niche signals can be addressed with the aid of microscale positional control and timelapse imaging.

## Acknowledgements

---

I am honored to acknowledge the many people who have helped and inspired me during the time I have spent in graduate school. Above all, I would like to thank my mentors Michel and Dave, for their intellectual support and advice throughout the years. Your collective insights into the scientific process, as well as the practical realities of academic life, will remain invaluable to me throughout my career.

I thank my committee members Henk Roelink and Zev Gartner for providing useful advice and support. Additionally, I would like to acknowledge Luke Lee for training me during the first portion of my graduate career.

I would also like to thank my colleagues and labmates for showing me the ropes and broadening my intellectual horizons: Frankie Myers, David Breslauer (who knows I'm pretty), Rick Ruby Henrikson, Megan Dueck, Tanner Nevill, Liz Wu, Robin Held, Randall Janairo, Raptor Dan, Gabriel Lavella, Peter Ledochowitsch, Jaehyun Park, Noem Ramey, Mary West, Randy Ashton, Albert Keung, Priya Shah, Ashley Fritz, Shawdee Eshghi, Lukasz Bugaj. Thanks for all that you have taught me and for making it so much fun at the same time.

I also thank my dedicated and hardworking undergraduates - Edward Ha, Nikit Patel, and Eva Li - for their intellectual and experimental contributions.

Everyone who made the MBL Physiology 2009 course happen will have a special place in my heart, especially Wallace Marshall, whose intellectual curiosity and sheer excitement about science is truly inspiring.

To a few of my friends - Maddie Girard, Katy Guimond, Gabrielle Miller-Messner, and Shirali Pandya - you ladies are beyond awesome. Thanks for all the fascinating discussions, for the late night bat-making sessions, for teaching me about marine invertebrates, and for always being willing to lend an ear throughout the years.

Mark DeWitt, I am always grateful for your support and eternal optimism.

I am indebted to my parents and my laolao for giving me not only every opportunity possible, but also the freedom to develop my own passions and life path. I will always be impressed by the examples you have set and strive to match your perseverance and strength of character.

Lastly, I would also like to acknowledge my funding sources, the National Science Foundation Graduate Fellowship, the National Defense Science and Engineering Graduate Fellowship, and the Berkeley Sensors and Actuators Center.

# Chapter 1: Background

---

## *1.1. Stem Cell Biology*

Stem cells have two essential qualities: the capacity to differentiate into one or more specialized cell types and the capacity to self-renew, or indefinitely maintain themselves in an immature state. Collectively, these two qualities endow stem cells with enormous potential to regenerate damaged and diseased tissues. Specifically, the field of regenerative medicine aims to develop approaches to amplify stem cells *in vitro* to clinically relevant quantities, differentiate the resulting cultures into specific cells of therapeutic interest, and implant them into a site of disease<sup>1</sup> or injury. In addition to this clinical potential, stem cells can serve as models for the basic investigation of developmental processes<sup>2</sup> or human disease<sup>3</sup>.

What does it mean for a cell to differentiate? At the most basic level, differentiation is the process whereby a cell alters the regulation of its genes so that it may serve a specialized function. These differences in gene regulation are a result of epigenetic changes, which are non-genetic but heritable. Specifically, direct covalent modification of chromatin is known to be responsible for regulating gene expression levels during differentiation. In mammals, the methylation of the cytosine in dinucleotide CpG sites in gene promoters during the differentiation process often has the effect of silencing those genes. Since dedicated methyltransferases ensure that cytosines on both strands of the site are methylated, the pattern is maintained through cell divisions<sup>4</sup>. Modifications of the histone proteins that wrap DNA are also implicated in gene regulation, but whether they are heritable is up for debate<sup>5</sup>.

In addition to these direct chromatin modifications, self-sustaining transcriptional loops<sup>6,7</sup> and small noncoding RNAs<sup>8</sup> have also been shown to be important for perpetuating changes in expression patterns. The fact that differentiated cells can be made to revert to an undifferentiated state demonstrates that even a fully differentiated phenotype is not permanent<sup>9</sup>. Rather differentiation states are regarded as “metastable,” and step-by-step transitions between states<sup>10</sup> can be extrinsically guided by presenting a series of external stimuli.

*In vivo*, cells exist in a dynamic and spatially complex local environment presenting these signals which can be orthogonal, synergistic, or at times conflicting. First described as a “niche” by Schofield in 1978<sup>11</sup>, the stem cell microenvironment is comprised of many elements: extracellular matrix structures, soluble factors, immobilized growth factors and morphogens<sup>12</sup>, mechanical forces<sup>13</sup>, and signals from numerous neighboring cells<sup>14</sup>. These extrinsic cues trigger signaling pathways within the stem cells that regulate their hallmark properties of self-renewal and differentiation (Figure 1-1). A reductionist approach that involves piecewise analysis and reconstitution of this microenvironment has led to the identification of numerous signals that can in turn be manipulated for biomedical applications.

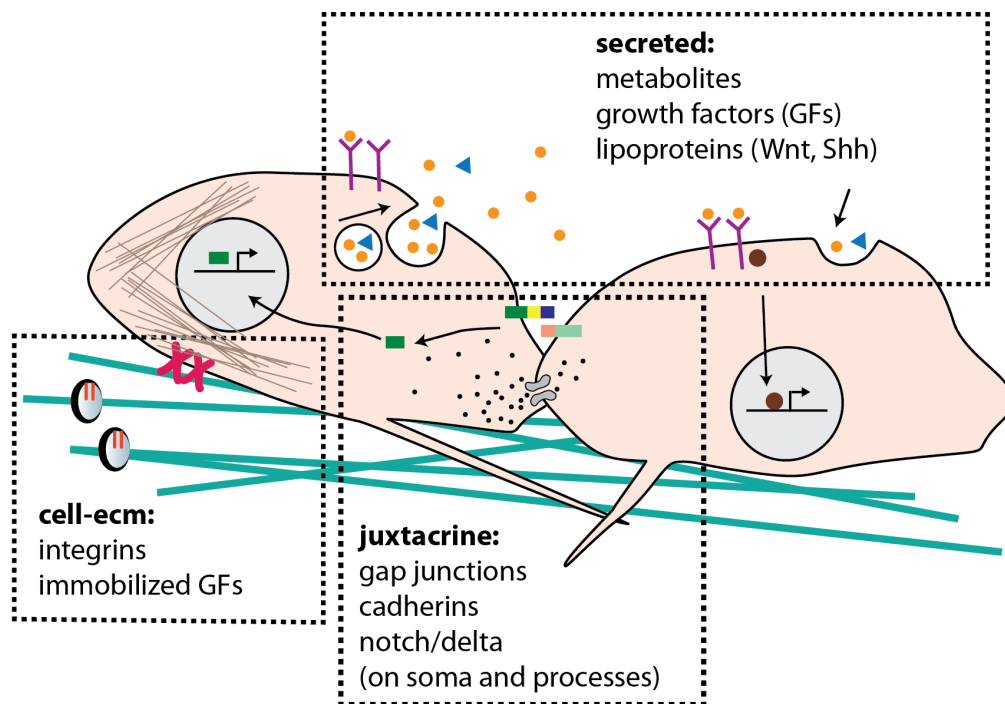


Figure 1-1. Overview of different modes of cell-cell interactions. Cells can secrete molecules (signaling ligands, metabolites) which bind to receptors expressed by themselves or by nearby cells. Secreted molecules can also be endocytosed and processed. Juxtacrine interactions include the diffusion of small molecules (<1kDa) through transmembrane gap junctions, mechanical forces through cadherin engagement (not shown) or membrane bound signaling through pathways such as Notch/Delta and Eph/ephrin. The membrane compartment where these signals take place (either soma or dendritic processes) affect the signaling properties. Additionally, cells can signal through the extracellular environment by secreting or degrading latent immobilized growth factors (such as TGF-beta) or producing mechanical forces on the extracellular matrix through integrin engagement. These interactions also affect neighboring cells which may take up latent immobilized signals or respond to mechanical perturbations in the ECM.

Of these microenvironmental factors, direct signaling from a neighboring cell to a stem cell is arguably one of the most difficult to study. Since cells signal through a variety of different mechanisms – by secreting chemical factors, signaling through contact-dependent receptor-ligand systems<sup>15,16</sup>, and exerting mechanical forces – their net effect cannot be approximated by stimulating one pathway alone, and their simultaneous transmission of these various types of regulatory information to a stem cell renders a reductionist approach challenging. Cells also present time-varying signals that are responsive to environmental cues<sup>17</sup>, suggesting that intercellular feedback mechanisms could be responsible for instructing stem cells to generate specific distributions of differentiated progeny<sup>18</sup>. Most importantly, correlating these interactions to final fate decisions is difficult since the effects of early regulatory signaling events may not be manifested until later when fate markers can be detected, making it difficult to establish causal ties between complex input signals and cell fate outcomes.

### *1.1.1 Modes of Interactions in the Stem Cell Niche: Lessons From an Invertebrate Model*

Although the concept of a stem cell niche was first introduced in reference to a mammalian system<sup>11</sup>, stem cell niches are most well-articulated in invertebrates. For example, we now have a mostly complete portrait (Figure 1-2a) of the cellular players and molecular pathways comprising the *Drosophila* ovary, which houses and regulates the division and differentiation of germline stem cells (GSCs). With the aid of sophisticated molecular and genetic tools allowing tissue-specific overexpression of particular genes, researchers have found that GSCs rely on signaling from various neighboring cell types. Normally GSCs are maintained in contact through adherens junctions to cap cells, which are found at the apical end of the structure. Cap cells maintain GSC self-renewal mainly by secreting the ligand decapentaplegic (Dpp, a member of the BMP pathway). Although the secreted Dpp is sufficient for dictating the fate of each GSC, cadherin engagement is necessary to keep cells anchored within reach of the Dpp-secreting cap cells. When the GSC divides, one daughter cell may lose contact with the cap cell and move away from the cap cell, thus reducing its exposure to Dpp and initiating its differentiation into an egg cyst. This differentiation process is also dependent on gap junctions, which are small intercellular pores formed by transmembrane connexin proteins, that allow the lateral transfer of essential small molecules from neighboring cells<sup>19</sup>. Other somatic stem cells also exist in the niche, continuously replenishing the sheath and follicle cells that envelop the egg cyst as it prepares to exit the ovary. To remain anchored at the correct positions, the follicle stem cells bind via integrins to a self-secreted extracellular matrix protein, laminin<sup>19</sup>.

What the *Drosophila* ovary demonstrates is that very local cell-cell interactions can dictate cell fate. Paracrine signaling through secreted factors like Dpp can have an effective range of only one cell diameter due to its low solubility<sup>20</sup>. Juxtacrine signaling through membrane bound ligands, such as Delta, binding to their cognate receptors (Notch) is important for regulating the niche size during development<sup>21,22</sup>. Cellular adhesion proteins can be necessary to localize cells to other cells (via cadherins) or to extracellular matrix structures (via integrins), which may be reciprocally modified by the very cells they are anchoring. Intercellular coupling through gap junctions may be needed to ensure cellular homeostasis.

Additionally, cellular movements as a result of division (or chemoattraction or differential adhesive properties) may change the signaling environment experienced by a cell.

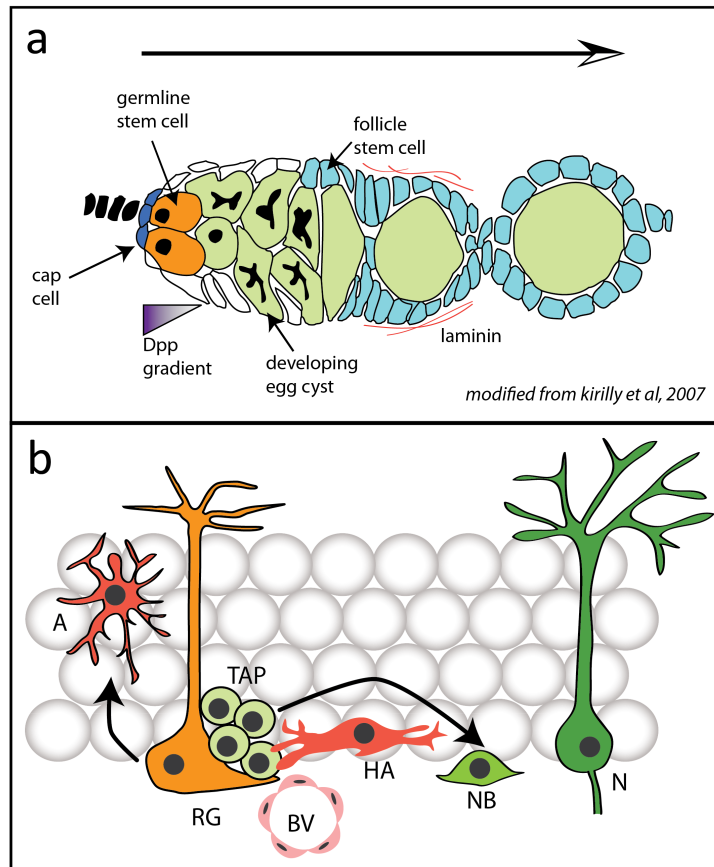


Figure 1-2. Contrasting the *Drosophila* ovary niche (a) with the adult neural stem cell niche (b). In the ovary, cap cells secrete Dpp to maintain the dedifferentiated state of the germline stem cell at short range. Cadherin mediated adhesion keeps germline stem cells anchored in place. Diving germline stem cells that lose contact differentiate into egg cysts, while moving out of the ovary. Follicle stem cells anchor themselves in place by secreting laminin and continuously divide to form follicle cells that surround the egg as it exits the ovary. In the subgranular zone of the dentate gyrus (b), stem cells (which are radial glia - RG) divide to form astrocytes (A), oligodendrocytes (not shown) or transit-amplifying progenitors (TAP) which are neuronally restricted. Initially in clusters at the base of radial glia, transit-amplifying progenitors further differentiate into migratory neuroblasts (NB), which then give rise to granule neurons (N) that integrate into the granule cell layer. Both the stem and progenitor cells receive signaling cues from adjacent granule neurons (gray circles), existing hippocampal astrocytes (HA), blood vessels (BV), and other stem and progenitor cells. Unlike in the *Drosophila* ovary, it is not well understood how these signaling cues are integrated to trigger self-renewal or differentiation in neural stem cells.

The picture is much less complete for many adult mammalian stem cell niches. While we know that some of the same molecular players are important for mammalian cells, it can be difficult to measure subtle phenotypes, identify the source of the signaling molecules, study their dynamic regulation, or investigate intercellular feedback mechanisms. In mammals, stem cells are often more difficult to identify and study due to their extreme rarity, lack of reliable markers, and capacity to remain quiescent for extremely long periods of time<sup>23</sup>. Additionally, many niches are not architecturally stereotypical at the single-cell level, as they are in insects



(with the exception of the single intestinal crypt stem cell that regenerates the intestinal epithelia<sup>24</sup>). The long timeframe of mammalian genetics and the difficulty of visualizing the niche environment *in vivo* for extended periods are major limitations that slow the process of discovery. Since mammalian cells can be more easily transduced *in vitro* to express reporter genes, mutant genes or shRNAs for gene knockdown, developing *in vitro* platforms to investigate intercellular interactions could yield important discoveries that can later be validated *in vivo*.

### 1.1.2 Adult Neural Stem Cells and Their Niche

The process of adult neurogenesis plays critical roles in spatial learning and memory<sup>25,26</sup>. The generation of new neurons in the adult mammalian brain occurs in two locations: the subventricular zone (SVZ) and the subgranular zone (SGZ) of the dentate gyrus (DG) in the hippocampus. New neurons generated within the subventricular zone move along the rostral migratory stream (RMS) to the olfactory bulb and along the medial migratory stream (MMS) to the ventromedial prefrontal cortex in humans<sup>27</sup>. SGZ neural stem cells generate neurons that integrate within the hippocampal granule layer above contributing to the formation of spatial memory networks<sup>26</sup>. The neural stem cells used for our experiments are derived from the SGZ so we will primarily restrict our discussion to SGZ neural stem cells.

A true neural stem cell possesses the capacity to self-renew, remain quiescent, and generate progeny that differentiate into mature neurons, astrocytes, and oligodendrocytes. In both the SGZ and the SVZ, radial glial cells are typically believed to be the resident neural stem cells<sup>28-30</sup>. These radial glia, also known as Type I neural stem cells, have their soma embedded at the bottom of the granule cell layer and processes extending into the upper molecular layer of the DG<sup>31</sup>. They divide horizontally with their processes in place, creating Type II transit-amplifying progenitors that are GFAP-, Sox2+, nestin+, and S100β-. These transit amplifying progenitors then proliferate and generate neurons that integrate into the granule layer, though some studies suggest that these Sox2+ nonradial precursors may be the true stem cells<sup>32,33</sup>. They tend to be found in small clusters cradled between the radial glial cell and the somas of granule neurons, interacting frequently with nearby horizontal (non-stem cell) astrocytes<sup>34</sup> and the endothelial cells lining blood vessels<sup>35,36</sup>.

The radial glial origin of adult neural stem cells is not surprising since radial glia are known to generate the cortex during embryonic development. These cells are anchored apically at the ventricles and extend long processes through the developing cortex where they are basally anchored to blood vessel in the marginal zone<sup>30</sup>. Early in embryonic development, these radial glia divide asymmetrically to form neural progenitors that migrate in chains along the radial glia fiber to integrate into developing cortex<sup>37,38</sup>. At late stages in embryonic development, both cell-intrinsic<sup>39</sup> and cell-extrinsic changes<sup>40</sup> trigger a switch to mostly gliogenesis<sup>41</sup>.

However, recent studies illustrating the transition from embryonic radial glia to adult radial glia showed that adult radial glia do not just retain the same radial processes as embryonic radial glia. Instead, at birth very few radial glia processes are present, with new GFAP+ radial processes extending postnatally from immature progenitors in the SGZ around P3.

Intriguingly, these do not stain for brain lipid binding protein (BLBP) which is present in embryonic radial glial processes<sup>42</sup>.

In addition to subtle differences in marker expression<sup>42</sup>, these adult stem cells exhibit a different pattern of proliferation and differentiation, as revealed by *in vivo* experiments using a sophisticated genetic technique known as tissue-specific Cre-lox recombination. A P1 bacteriophage recombinase, Cre mediates recombination events at specific sites known as loxP sites<sup>43</sup>. Cre expression under tissue-specific promoters can be used in combination with a GFP reporter gene<sup>44</sup> whose expression requires Cre-mediated excision of an upstream sequence. By expressing CreERT2 (a tamoxifen-inducible version of Cre) under the nestin promoter<sup>45</sup>, researchers can generate labeled clones originating from a single radial glial cell, showing that adult stem cells asymmetrically divide to form astrocytes and neuronal progenitors at roughly equal proportions<sup>29</sup>. Previous studies showing that neurogenesis was ten times more frequent<sup>46</sup> may be an artifact of the intermediate progenitor step, where proliferation increases the number of neurons generated. An astrocyte, on the other hand, was recently discovered to be specified through a single asymmetric division<sup>29</sup>.

Thus, whereas the fates of embryonic neural stem cells are specified at distinct temporal stages, adult neural stem cells can be specified into both neurons and astrocytes concomitantly. This fate decision hinges largely on signals received from their interactions with other progenitors, astrocytes, granule neurons, and the neighboring bloodstream through which hormones and other signaling molecules are delivered<sup>35,36</sup>.

The influence of these neighboring niche cells have been shown to affect the proliferation and differentiation of both type I and type II progenitors (Figure 1-2b). *In vitro*, astrocyte co-culture has been shown to induce proliferation and neuronal differentiation of adult NSCs<sup>47</sup> through both secreted and juxtacrine mechanisms. The molecular mediators of this neurogenic effect include Wnts<sup>48,49</sup> and ephrin<sup>50</sup>, whose effects have been confirmed both *in vitro* and *in vivo*. Wnts have also been shown to regulate the symmetry of divisions in neural stem cells<sup>51</sup>.

Additionally, Notch signaling between progenitors is required for self-renewal and expansion<sup>47</sup> by inhibiting neuronal differentiation<sup>52</sup>. E-cadherin expressed by neural stem cells, progenitors and neighboring niche cells have also been shown to be important for regulating proliferation and self-renewal of the pluripotent phenotype<sup>53</sup>. Genetic ablation of E-cadherin results in fewer pluripotent NSCs capable of forming neurospheres. The transfer of metabolites and small molecules through gap junctions also plays a role in the maintenance of type I radial glia *in vivo*<sup>54</sup>, and is important for neural-stem-cell mediated repair after injury<sup>55</sup>.

Neural stem cells can also be differentiated into subtypes specific to other regions of the brain. For example, ectopic transplantation of *in vitro*-expanded SGZ progenitors into the SVZ produced progeny that not only migrated along the same RMS to the olfactory bulb, but that also differentiated into the tyrosine hydroxylase-positive neurons commonly found

there<sup>56</sup>. This fate plasticity demonstrates clearly that the signaling environment is of utmost importance in regulating differentiation decisions.

Most of what is known about these stem and progenitor cells is uncovered by up- or down-regulating genes *in vivo* through known small molecule regulators of specific pathways<sup>48</sup>, retro- or lentiviral mediated gene delivery<sup>57</sup>, or as discussed, tissue-specific Cre-lox mediated recombination<sup>43</sup> to target genetic alterations to specific cell types and tissue compartments. BrdU techniques and immunohistochemical staining<sup>58</sup> can be used to label recently divided cells and cell fate using specific immunomarkers. However, even tissue-specific expression of mutant genes can have off-target effects, activating in non-target cells within the same or different organ causing premature death or unwanted side effects<sup>59</sup>. Additionally, these studies cannot provide dynamic information within the same organism due to technical and practical constraints for *in vivo* imaging<sup>60</sup>.

Thus, there are still many open questions about the population dynamics, kinetics, and bidirectionality of stem cell regulation by contact with neighboring cells. Is a single neighboring cell sufficient to strongly influence NSC fate decisions, or are contacts with multiple cells necessary? If the latter, how many cells of each type are minimally necessary to induce differentiation down a specific lineage or promote self-renewal? How long must these cells be in contact? How are these various signals integrated to result in a fate commitment decision? When one stem cell makes a fate commitment, is this information conveyed to neighboring NSCs and does it in turn influence their fate commitment<sup>15,61,62</sup>? The development and application of better *in vitro* tools for manipulating and spatially patterning individual cells will help to answer some of these questions.

## **1.2. Microtechnologies For Modulating Cell-To-Cell Signaling**

Simple forms of *in vitro* “niches” have been essential for many stem cell systems, including embryonic stem cells<sup>63-65</sup>, whose derivation and subsequent culture relied on mitotically inactivated fibroblasts as feeder layers. A homogenous culture of stem cells can be greatly affected by factors such as cell culture density<sup>66</sup> and whether the cells are passed as single cells or colonies<sup>67</sup>. The spatial organization of cell culture is an inherent physical property that underpins intercellular signaling processes and contributes to fate outcomes in a more deterministic way than previously appreciated<sup>68</sup>.

To gain mechanistic insight into how stem cells are dynamically regulated by other cells during differentiation and self-renewal processes, it is useful (and perhaps even necessary) to spatially monitor and control individual cells. While spatial organization has historically been controlled *for*, this can now be explicitly controlled by cellular micropatterning technologies that make it possible to position cells with defined connectivity and at single cell resolution.

The recent explosion of microfluidics and other microtechnologies for biological applications was made possible by the advent of soft lithography<sup>69</sup>, a set of simple techniques using elastomeric molding to perfectly replicate the microscale features of molds made through conventional cleanroom photolithography (Figure 1-3). Specifically, the field’s adoption of

polydimethylsiloxane (Figure 1-3b), a transparent and biocompatible elastomer, for the fabrication of microfluidic devices enabled rapid prototyping of devices for applications across cell biology, biochemistry, and increasingly, developmental biology. In addition to its optical clarity, PDMS is also gas-permeable which enables the culture of mammalian cells that typically require a 5% CO<sub>2</sub> environment for maintaining their bicarbonate buffered medium at pH 7.4<sup>70</sup>. Additionally PDMS can be bonded irreversibly to a clean glass substrate by treating both surfaces to create free silanol groups (-Si-OH). When the activated surfaces are brought together, a condensation reaction creates a covalent Si-O-Si bond. Thus PDMS can be used to mold open channels from lithographically defined features on a wafer, and then bonded to glass or other Si-OH containing materials to form microfluidic channels.

However, PDMS has some important drawbacks. It is permeable not only to gas and water, but also to hydrophobic molecules, which include important biomolecules such as lipids, steroids, or other small molecules that are used as agonists or antagonists of signaling pathways<sup>71</sup>. Additionally, typical preparations of PDMS often result in the retention of residual low-molecular weight oligomers that can constitute up to 5% w/w of the cured material and have been shown to incorporate into the cell membranes of breast cancer cells (MCF-7) on-chip<sup>71</sup>. These oligomers can be extracted through a succession of solvent washes<sup>72,73</sup>, but this step is often omitted.

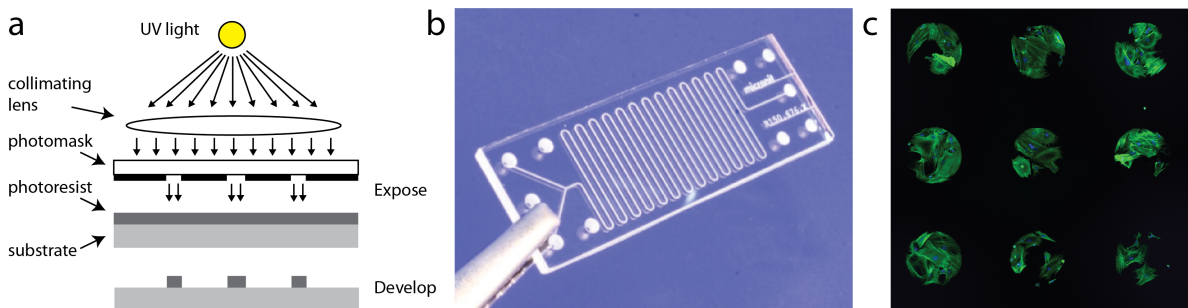


Figure 1-3. Microscale technologies for cell biology. Photolithography (a) enables the creation of micron-scale relief features that are used as molds to create microchannels in PDMS (b) or surface microposts that can be used for patterning proteins and cells (c). Here we show mouse embryonic fibroblasts grown on circular patterns stained with phalloidin-488 as an example.

Broadly, microscale technologies endow researchers with the ability to physically position cells, signaling ligands, or ECM molecules down to single-cell or sub-micron resolution. Surface micropatterns are created by patterning cytophilic and cytophobic regions on 2D cell culture substrates such as polystyrene or glass<sup>74,69,75</sup>. The elastomeric molds for stamping these patterns are typically cast using PDMS from wafers with relief structures defined by conventional photolithographic techniques. For many chemistries, these micropatterns can last for weeks in culture<sup>76</sup>, exerting a constant spatial boundary condition over the cells seeded on their surface (Figure 1-3c). 3D cellular patterns can also be generated by imprinting these molds directly into hydrogels to form cavities that support cell growth. Additionally, the patterned areas can be dynamically regulated by releasing patterns<sup>77</sup>, by using *in situ* photolithography processes<sup>78</sup> and other techniques<sup>79</sup>. Patterning multiple cell types can also be

achieved using microscope-based *in situ* photopatterning, micromachined interlocking substrates, and orthogonal chemistries. Since some of the technologies described here have not made the full leap from the engineer's workbench to the stem cell biologist's toolkit, examples using other cell models will at times be described to illustrate the potential of these approaches.

Depending on the implementation details, different functionalities are possible, ranging from simple micropatterns regulating colony size to heterotypic multicellular constructs with single cell resolution. In the next few pages, we draw on examples from the literature to illustrate how these technologies may be applied for stem cell systems and for investigating cell-cell signaling more broadly.

### *1.2.1 Static 2D Micropatterns Reveal Autoregulatory Signaling Loops*

Even very simple static micropatterns have yielded important insights, by using a single parameter such as size or shape to tune endogenous signaling. Motivated by the fact that hESC survival was dependent on colony passaging, Peerani et al. patterned hESCs into circles of varying size to investigate whether autoregulatory feedback loops governed self-renewal and differentiation<sup>80</sup>. Bigger colonies resulted in much better maintenance of the pluripotent state due to auto-regulatory signaling through the BMP pathway, members of the TGF-beta superfamily known to promote differentiation in hESCs. They observed that individual cells were highly influenced by their neighbors: cells which were surrounded by Oct4+ cells were more likely to remain positive for Oct4 and negative pSmad1, which is an important mediator of the BMP pathway. These Oct4+ cells were also shown to secrete antagonists of the BMP pathway, while their Oct4- neighbors secreted BMP itself.

Intriguingly, they found that small colonies (200  $\mu\text{m}$ ) were only 20% positive for the pluripotency marker, Oct4, whereas larger colonies (600 and 800  $\mu\text{m}$ ) were all 80% Oct4+. This bistability suggests the existence of intercellular feedback loops that maintain the pluripotency state of hESCs so long as the initial environment contains a threshold concentration of essential factors such as BMP antagonists. Extending this concept, the same group studied the effect of colony size in the presence of differentiation inducers (BMP and Activin A), finding that smaller patterns drive primitive endodermal differentiation and that larger patterns drive mesodermal differentiation<sup>81</sup>.

### *1.2.2 Investigating Morphogenesis in Patterned 3D Gels*

In a similar vein, studies applying simple morphological constraints on mammary epithelial tissue discovered fundamental mechanisms regulating branching morphogenesis and self-organization in the mammary gland. The mammary duct normally exists as a bilayered tubular network with a 3-dimensional branched structure. Nelson et al. showed that epithelial cells grown in embossed microcavities in collagen gels would self organize into hollow tubules. When stimulated to undergo branching morphogenesis, the tubules tended to invade into adjacent collagen at the tips of patterned tubules<sup>82</sup>. By immunostaining for putative growth factors, the authors discovered an increased concentration of TGF- $\beta$ 1 along the

midsection of the tubules, suggesting that autocrine secretion of TGF- $\beta$ 1 inhibited branching. Inhibition of TGF- $\beta$ 1 induced isotropic branching along the patterned tubule, and not just at areas of high convexity where the effective cell density was low. These experiments demonstrate that branching cues, at least in part, derive from the intrinsic geometry of existing epithelial ducts and not from signaling cues provided by surrounding cells.

Another study from the same group used stiffer cylindrical microcavities to investigate whether a mixture of two separate lineages of mammary epithelial cells could self-organize into bilayered structures<sup>83</sup>. This time, deposited cells could not adhere or invade the surrounding material (a synthetic elastomer), causing them to aggregate within the confined cavities. This *ex vivo* reconstitution of an *in vivo* structure normally formed through regulated morphogenetic processes was necessary to impose an initial disorganized state. Observation of the two lineages showed that over 48 hours they could self-segregate into the interior (luminal cells) or exterior (myoepithelial cells) of the structure, a process almost solely driven by dynamic E-cadherin-mediated cell-cell adhesions.

### *1.2.3 Removing Paracrine Factors By Flow*

From developmental studies, several major classes of paracrine signaling proteins are known to be critically important for stem cells, including fibroblast growth factors (FGF), epidermal growth factors (EGF), Hedgehogs, Wnts, and transforming growth factors (TGF- $\beta$ ). These pathways are important in regulating differentiation, proliferation, apoptosis, and spatial patterning processes such as tissue boundary formation and specifying limb bud polarity. For *in vitro* stem cell culture, factors such as FGF, EGF, BMP and LIF (two members of the TGF-beta family) are commonly used to maintain cells in a state of self-renewal or to induce differentiation. However, in addition to these major classes, cells secrete hundreds of different molecules, complicating the identification of which factor or combination of factors is relevant.

A novel way to assess the role of specific paracrine signaling pathways is to sweep away all paracrine signals and combinatorially re-introduce them and add factors back. Blagovic et al. found that continuously perfusing mouse ES cells in a microfluidic chamber with fresh differentiation medium disrupted neuroectodermal specification and expansion, indicating that auto-regulatory paracrine signaling was necessary<sup>84</sup>. Adding back FGF-4, a factor known to be secreted in the system, partially rescued the phenotype but was insufficient by itself. Further research using this system could help to identify whether paracrine signaling factors in ES cells can be reduced to a minimally sufficient set for both self-renewal and differentiation processes.

### *1.2.4 Biomimetic Co-Cultures in Configurable Devices*

Since all tissues and by extension, stem cell niches, are heterogeneous, positional control over multiple cell types would facilitate the creation of co-cultures that approximate the native properties of a complex tissue. Simple forms of two-component co-cultures has long been enabled by simple Transwell inserts, wherein cells grown on a porous membrane can signal in

trans to cells grown in the underlying well<sup>47,85</sup>. However, this system does not have controllable spatial parameters and its applicability is restricted to long-range diffusible signals. Novel microscale reconstructions of *in vivo* cellular microenvironments can reveal important insights about basic biological processes that are not observable by traditional techniques.

For example, the *ex vivo* culture of liver hepatocytes is known to require essential signals from stromal cells to maintain proper hepatocyte function. However, conditioned media from these cell types and transwell insert co-cultures have proven ineffective<sup>86</sup>, indicating that signaling must occur at a closer range. To investigate the dependence of hepatocyte function on signaling from these neighboring fibroblasts, Hui et al.<sup>79</sup> engineered microfabricated culture substrates whose relative distance could be adjusted. These micromechanical combs were fabricated in silicon wafers by deep reactive ion-etching. Two combs fit together by an integrated snap-lock mechanism at two positions to allow for distinct populations of cells to be cultured on the fingers in contact or gap mode. Using this system, they discovered that hepatocytes needed direct contact with neighboring stroma for the first 24 hours of *in vitro* culture, after which close-range soluble signals were sufficient for preserving hepatocyte viability and function. The molecular basis for this transient requirement for cell-cell contact has not been fully elucidated but the non-transmembrane T-cadherin is one candidate mediator<sup>87</sup>.

Another example demonstrating the potential of applying microscale technology to re-creating tissue microenvironments is in the novel design of a lung tissue mimic<sup>88</sup>. The authors of this study engineered a microfluidic device with a porous silicone membrane bisecting a microchannel. The porous membrane supported the growth of human alveolar epithelial cells on one side and microvascular endothelial cells on the other, forming a structural equivalent to the alveolar-capillary interface. After cells were grown to form tight monolayers, air was introduced to the alveolar compartment to mimic the air-liquid interface. Functional validation of this device showed properties – increased surfactant expression, increased electrical resistance across the bilayer, and greatly reduced trans-bilayer protein permeability – commensurate with *in vivo* observations. Additionally, the mechanical loading of physiological breathing could be simulated by applying cyclic pressure to two unconnected smaller channels flanking the central culture channel, stretching the cells cultured in the central channel. Using this device, they discovered that the harmful effects of nanoparticulate pollutants, as simulated by silica nanoparticles, were significantly enhanced by cyclic strain. Under conditions of cyclic strain, alveolar epithelia not only exhibited higher levels of cellular oxidative stress but they also transported nanoparticles to the endothelial compartment, effectively spreading the toxicity systemically. This system uniquely integrates mechanical and cellular features that are integral to a functional lung alveolus, enabling sustained *in vitro* observation in response to relevant stimuli.

### 1.2.5 Micropatterning With Single Cell Resolution

To truly recreate the structural complexity of a multicellular microenvironment, positional control of single cells can be extremely useful. Since the resolution of photolithography is far

smaller than that of a single cell, size-matched surface patterns<sup>89</sup> or physical well-based traps<sup>90,91</sup> allow contacts between individual cells to be precisely engineered. For example, bowtie and propeller-shaped micropatterns allowed researchers to decouple the effects of juxtacrine signaling from secreted factor signaling in regulating proliferation between individual endothelial cells<sup>89</sup>. Assessment of DNA synthesis revealed a biphasic relationship between cell contact and proliferation, with single cells and cell triplets proliferating less than cell pairs. Exogenous VE-cadherin stimulation was also sufficient to rescue proliferation in the single-cell state, indicating that VE-cadherin was solely responsible for enhancing proliferation by providing junctional attachments for cells to regulate their intracellular stiffness.

While patterning with single cell resolution can work for investigating behavior between homogenous cell types, heterotypic interactions are more difficult to engineer. Patterning multiple cell types at high resolution is not trivial, as all cell types express integrin adhesion receptors and engage with extracellular matrix proteins via integrin receptors. Since cells often express overlapping sets of integrins, it can in general be impossible challenging to find ECM molecules that bind one cell type but not the other can distinguish between cell types. Thus, patterning multiple cell types requires alternative technologies for orthogonal treatment of different cells.

One study succeeded in co-patterning 3T3 fibroblasts and mouse ES cells by exploiting a specific property of hyaluronic acid (HA). HA resists cell and most protein adsorption except collagen, making it an effective blocking layer until it is rendered cytophilic by collagen coating<sup>92</sup>. Another method to pattern multiple cell types is by *in situ* photopatterning of a bio-compatible cytophobic photoresist<sup>78</sup>. The photoresist can be exposed using the UV channel of a fluorescent microscope, revealing a biotinylated substrate that can bind avidin-bound ECM or antibody molecules for cell binding. Thus, different cells can be patterned in succession by serially exposing spots in the field of view. Finally, one very promising technology for patterning multiple cell types is by labeling cells with oligonucleotides<sup>93</sup> and capturing them on surfaces decorated with the complementary strand<sup>94</sup>. This approach lends itself well to multiplexing due to the combinatorial nature of DNA and can be a very powerful tool for patterning in both 2D<sup>94,95</sup> and 3D<sup>96</sup>.

Fine control over cellular positioning and other aspects of the cellular microenvironment is an important tool for discovery, especially in light of evidence that cell-to-cell variability can be largely determined by environmental factors<sup>68</sup>. The insights gained from *in vitro* reconstitution studies illuminate not only the necessary components for proper cell and tissue function, but also what is sufficient to recreate complex physiological processes such as stem cell self-renewal and differentiation.



### 1.3 References

- 1 Kim, J.-H. *et al.* Dopamine neurons derived from embryonic stem cells function in an animal model of Parkinson's disease. *Nature* **418**, 50-56,(2002).
- 2 ten Berge, D. *et al.* Wnt signaling mediates self-organization and axis formation in embryoid bodies. *Cell stem cell* **3**, 508-518,(2008).
- 3 Dimos, J. T. *et al.* Induced pluripotent stem cells generated from patients with ALS can be differentiated into motor neurons. *Science* **321**, 1218-1221,(2008).
- 4 Cedar, H. & Bergman, Y. Linking DNA methylation and histone modification: patterns and paradigms. *Nature reviews. Genetics* **10**, 295-304,(2009).
- 5 Ptashne, M. On the use of the word 'epigenetic'. *Curr Biol* **17**, R233-236,(2007).
- 6 Davey, R. E., Onishi, K., Mahdavi, A. & Zandstra, P. W. LIF-mediated control of embryonic stem cell self-renewal emerges due to an autoregulatory loop. *The FASEB journal : official publication of the Federation of American Societies for Experimental Biology* **21**, 2020-2032,(2007).
- 7 Laslo, P. *et al.* Multilineage transcriptional priming and determination of alternate hematopoietic cell fates. *Cell* **126**, 755-766,(2006).
- 8 Lakshminpathy, U., Davila, J. & Hart, R. P. MicroRNA in pluripotent stem cells. *Regen Med.* **5**, 545-555,(2010).
- 9 Takahashi, K. & Yamanaka, S. Induction of pluripotent stem cells from mouse embryonic and adult fibroblast cultures by defined factors. *Cell* **126**, 663-676,(2006).
- 10 Chang, H. H., Oh, P. Y., Ingber, D. E. & Huang, S. Multistable and multistep dynamics in neutrophil differentiation. *BMC cell biology* **7**, 11,(2006).
- 11 Schofield, R. The relationship between the spleen colony-forming cell and the haemopoietic stem cell. *Blood cells* **4**, 7-25,(1978).
- 12 Annes, J. P. Making sense of latent TGFbeta activation. *Journal of Cell Science* **116**, 217-224,(2003).
- 13 Discher, D. E., Mooney, D. J. & Zandstra, P. W. Growth factors, matrices, and forces combine and control stem cells. *Science (New York, N.Y.)* **324**, 1673-1677,(2009).
- 14 Fuchs, E., Tumber, T. & Guasch, G. Socializing with the neighbors: stem cells and their niche. *Cell* **116**, 769-778,(2004).
- 15 Artavanis-Tsakonas, S. Notch Signaling: Cell Fate Control and Signal Integration in Development. *Science* **284**, 770-776,(1999).
- 16 Pasquale, E. B. Eph-ephrin bidirectional signaling in physiology and disease. *Cell* **133**, 38-52,(2008).
- 17 Kholodenko, B. N. Cell-signalling dynamics in time and space. *Nature Cell Biology* **7**, 165-176,(2006).
- 18 Kirouac, D. C. *et al.* Cell-cell interaction networks regulate blood stem and progenitor cell fate. *Molecular systems biology* **5**, 293-293,(2009).
- 19 Kirilly, D. & Xie, T. The Drosophila ovary: an active stem cell community. *Cell research* **17**, 15-25,(2007).
- 20 Groppe, J. *et al.* Biochemical and biophysical characterization of refolded Drosophila DPP, a homolog of bone morphogenetic proteins 2 and 4. *J Biol Chem* **273**, 29052-29065,(1998).
- 21 Ward, E. J. *et al.* Stem cells signal to the niche through the Notch pathway in the

- Drosophila ovary. *Curr Biol* **16**, 2352-2358,(2006).
- 22 Ward, E. J., Zhou, X., Riddiford, L. M., Berg, C. A. & Ruohola-Baker, H. Border of Notch activity establishes a boundary between the two dorsal appendage tube cell types. *Dev Biol* **297**, 461-470,(2006).
- 23 Morrison, S. J. & Kimble, J. Asymmetric and symmetric stem-cell divisions in development and cancer. *Nature* **441**, 1068-1074,(2006).
- 24 Casali, A. & Batlle, E. Intestinal stem cells in mammals and Drosophila. *Cell stem cell* **4**, 124-127,(2009).
- 25 Gage, F., Kempermann, G., Song, H. & Laboratory, C. S. H. *Adult neurogenesis*. (Cold Spring Harbor Laboratory Press, 2008).
- 26 Zhang, C.-L., Zou, Y., He, W., Gage, F. H. & Evans, R. M. A role for adult TLX-positive neural stem cells in learning and behaviour. *Nature* **451**, 1004-1007,(2008).
- 27 Sanai, N. *et al.* Corridors of migrating neurons in the human brain and their decline during infancy. *Nature* **478**, 382-386,(2011).
- 28 Seri, B., Garcia-Verdugo, J. M., McEwen, B. S. & Alvarez-Buylla, A. Astrocytes give rise to new neurons in the adult mammalian hippocampus. *J Neurosci* **21**, 7153-7160,(2001).
- 29 Bonaguidi, M. A. *et al.* In vivo clonal analysis reveals self-renewing and multipotent adult neural stem cell characteristics. *Cell* **145**, 1142-1155,(2011).
- 30 Kriegstein, A. & Alvarez-Buylla, A. The glial nature of embryonic and adult neural stem cells. *Annu Rev Neurosci* **32**, 149-184,(2009).
- 31 Rickmann, M., Amaral, D. G. & Cowan, W. M. Organization of radial glial cells during the development of the rat dentate gyrus. *J Comp Neurol* **264**, 449-479,(1987).
- 32 Lugert, S. *et al.* Quiescent and active hippocampal neural stem cells with distinct morphologies respond selectively to physiological and pathological stimuli and aging. *Cell stem cell* **6**, 445-456,(2010).
- 33 Suh, H. *et al.* In vivo fate analysis reveals the multipotent and self-renewal capacities of Sox2+ neural stem cells in the adult hippocampus. *Cell stem cell* **1**, 515-528,(2007).
- 34 Seri, B., García-Verdugo, J. M., Collado-Morente, L., McEwen, B. S. & Alvarez-Buylla, A. Cell types, lineage, and architecture of the germinal zone in the adult dentate gyrus. *The Journal of comparative neurology* **478**, 359-378,(2004).
- 35 Willhoite, A. R., Gage, F. H. & Palmer, T. D. Vascular niche for adult hippocampal neurogenesis. *The Journal of Comparative Neurology* **425**, 479-494,(2000).
- 36 Miller, F. D. & Gauthier-Fisher, A. Home at last: neural stem cell niches defined. *Cell stem cell* **4**, 507-510,(2009).
- 37 Noctor, S. C., Flint, A. C., Weissman, T. A., Dammerman, R. S. & Kriegstein, A. R. Neurons derived from radial glial cells establish radial units in neocortex. *Nature* **409**, 714-720,(2001).
- 38 Nadarajah, B., Brunstrom, J. E., Grutzendler, J., Wong, R. O. & Pearlman, A. L. Two modes of radial migration in early development of the cerebral cortex. *Nat Neurosci* **4**, 143-150,(2001).
- 39 Shen, Q. *et al.* The timing of cortical neurogenesis is encoded within lineages of individual progenitor cells. *Nat Neurosci* **9**, 743-751,(2006).
- 40 Morrow, T., Song, M. R. & Ghosh, A. Sequential specification of neurons and glia by

- developmentally regulated extracellular factors. *Development* **128**, 3585-3594,(2001).
- 41 Bayer, S. A. & Altman, J. *Neocortical development*. (Raven Press, 1991).
- 42 Brunne, B. *et al.* Origin, maturation, and astroglial transformation of secondary radial  
glial cells in the developing dentate gyrus. *Glia* **58**, 1553-1569,(2010).
- 43 Lakso, M. *et al.* Targeted oncogene activation by site-specific recombination in  
transgenic mice. *Proc Natl Acad Sci U S A* **89**, 6232-6236,(1992).
- 44 Novak, A., Guo, C., Yang, W., Nagy, A. & Lobe, C. G. Z/EG, a double reporter  
mouse line that expresses enhanced green fluorescent protein upon Cre-mediated  
excision. *genesis* **28**, 147-155,(2000).
- 45 Balordi, F. & Fishell, G. Mosaic removal of hedgehog signaling in the adult SVZ  
reveals that the residual wild-type stem cells have a limited capacity for self-renewal.  
*J Neurosci* **27**, 14248-14259,(2007).
- 46 Steiner, B. *et al.* Differential regulation of gliogenesis in the context of adult  
hippocampal neurogenesis in mice. *Glia* **46**, 41-52,(2004).
- 47 Song, H., Stevens, C. F. & Gage, F. H. Astroglia induce neurogenesis from adult  
neural stem cells. *Nature* **417**, 39-44,(2002).
- 48 Lie, D.-C. *et al.* Wnt signalling regulates adult hippocampal neurogenesis. *Nature* **437**,  
1370-1375,(2005).
- 49 Wexler, E. M., Paucer, A., Kornblum, H. I., Palmer, T. D. & Geschwind, D. H.  
Endogenous Wnt signaling maintains neural progenitor cell potency. *Stem Cells* **27**,  
1130-1141,(2009).
- 50 Ashton, R. S., Conway, A. & Schaffer, D. V. *Astrocytes regulate adult hippocampal  
neurogenesis through ephrin-B signaling* (2012).
- 51 Piccin, D. & Morshead, C. M. Wnt signaling regulates symmetry of division of neural  
stem cells in the adult brain and in response to injury. *Stem Cells* **29**, 528-538,(2011).
- 52 Imayoshi, I., Sakamoto, M., Yamaguchi, M., Mori, K. & Kageyama, R. Essential roles  
of Notch signaling in maintenance of neural stem cells in developing and adult brains.  
*The Journal of Neuroscience* **30**, 3489-3498,(2010).
- 53 Karpowicz, P. *et al.* E-Cadherin regulates neural stem cell self-renewal. *The Journal  
of Neuroscience* **29**, 3885-3896,(2009).
- 54 Kunze, A. *et al.* Connexin expression by radial glia-like cells is required for  
neurogenesis in the adult dentate gyrus. *Proc Natl Acad Sci U S A* **106**,  
11336-11341,(2009).
- 55 Jäderstad, J. *et al.* Communication via gap junctions underlies early functional and  
beneficial interactions between grafted neural stem cells and the host. *Proceedings of  
the National Academy of Sciences of the United States of America* **107**,  
5184-5189,(2010).
- 56 Suhonen, J. O., Peterson, D. A., Ray, J. & Gage, F. H. Differentiation of adult  
hippocampus-derived progenitors into olfactory neurons in vivo. *Nature* **383**,  
624-627,(1996).
- 57 Consiglio, A. *et al.* Robust in vivo gene transfer into adult mammalian neural stem  
cells by lentiviral vectors. *Proc Natl Acad Sci U S A* **101**, 14835-14840,(2004).
- 58 Kee, N., Sivalingam, S., Boonstra, R. & Wojtowicz, J. M. The utility of Ki-67 and  
BrdU as proliferative markers of adult neurogenesis. *J Neurosci Methods* **115**,  
97-105,(2002).

- 59 Schmidt-Supprian, M. & Rajewsky, K. Vagaries of conditional gene targeting. *Nature immunology* **8**, 665-668,(2007).
- 60 Schroeder, T. Imaging stem-cell-driven regeneration in mammals. *Nature* **453**, 345-351,(2008).
- 61 Gaiano, N. & Fishell, G. The role of notch in promoting glial and neural stem cell fates. *Annual Review of Neuroscience* **25**, 471-490,(2002).
- 62 Selkoe, D. & Kopan, R. Notch and Presenilin: regulated intramembrane proteolysis links development and degeneration. *Annual Review of Neuroscience* **26**, 565-597,(2003).
- 63 Thomson, J. a. Embryonic Stem Cell Lines Derived from Human Blastocysts. *Science* **282**, 1145-1147,(1998).
- 64 Evans, M. J. K. M. H. Establishment in culture of pluripotential cells from mouse embryos. *Nature* **292**, 154-156,(1981).
- 65 Martin, G. R. Isolation of a Pluripotent Cell Line from Early Mouse Embryos Cultured in Medium Conditioned by Teratocarcinoma Stem Cells. *Proceedings of the National Academy of Sciences* **78**, 7634-7638,(1981).
- 66 Taupin, P. *et al.* FGF-2-responsive neural stem cell proliferation requires CCg, a novel autocrine/paracrine cofactor. *Neuron* **28**, 385-397,(2000).
- 67 Xu, Y. *et al.* Revealing a core signaling regulatory mechanism for pluripotent stem cell survival and self-renewal by small molecules. *Proceedings of the National Academy of Sciences of the United States of America* **107**, 8129-8134,(2010).
- 68 Snijder, B. & Pelkmans, L. Origins of regulated cell-to-cell variability. *Nat Rev Mol Cell Biol* **12**, 119-125,(2011).
- 69 Whitesides, G. M. & Xia, Y. Soft lithography. *Angew. Chem. Int. Ed* **37**, 550-575,(1998).
- 70 El-Ali, J., Sorger, P. K. & Jensen, K. F. Cells on chips. *Nature* **442**, 403-411,(2006).
- 71 Regehr, K. J. *et al.* Biological implications of polydimethylsiloxane-based microfluidic cell culture. *Lab Chip* **9**, 2132-2139,(2009).
- 72 Lee, J. N., Park, C. & Whitesides, G. M. Solvent compatibility of poly(dimethylsiloxane)-based microfluidic devices. *Analytical chemistry* **75**, 6544-6554,(2003).
- 73 Vickers, J. A., Caulum, M. M. & Henry, C. S. Generation of hydrophilic poly(dimethylsiloxane) for high-performance microchip electrophoresis. *Anal Chem* **78**, 7446-7452,(2006).
- 74 Chen, C. S., Ingber, D. E., Whitesides, G. M., Mrksich, M. & Huang, S. Geometric Control of Cell Life and Death. *Science* **276**, 1425-1428,(1997).
- 75 Ingber, D. E., Whitesides, G. M., Tien, J., Dike, L. E. & Mrksich, M. Using Microcontact Printing to Pattern the Attachment of Mammalian Cells to Self-Assembled Monolayers of Alkanethiolates on Transparent Films of Gold and Silver. *Experimental Cell Research* **235**, 305-313,(1997).
- 76 Nelson, C. M., Raghavan, S., Tan, J. L. & Chen, C. S. Degradation of Micropatterned Surfaces by Cell-Dependent and -Independent Processes. *Langmuir* **19**, 1493-1499,(2003).
- 77 Jiang, X., Ferrigno, R., Mrksich, M. & Whitesides, G. M. Electrochemical desorption of self-assembled monolayers noninvasively releases patterned cells from geometrical

- confinements. *Journal of the American Chemical Society* **125**, 2366-2367,(2003).
- 78 Kim, M. *et al.* Addressable micropatterning of multiple proteins and cells by  
microscope projection photolithography based on a protein friendly photoresist.  
*Langmuir* **26**, 12112-12118,(2010).
- 79 Hui, E. E. & Bhatia, S. N. Micromechanical control of cell-cell interactions.  
*Proceedings of the National Academy of Sciences of the United States of America* **104**,  
5722-5726,(2007).
- 80 Peerani, R. *et al.* Niche-mediated control of human embryonic stem cell self-renewal  
and differentiation. *The EMBO journal* **26**, 4744-4755,(2007).
- 81 Lee, L. H. *et al.* Micropatterning of human embryonic stem cells dissects the  
mesoderm and endoderm lineages. *Stem cell research* **2**, 155-162,(2009).
- 82 Nelson, C. M., VanDuijn, M. M., Inman, J. L., Fletcher, D. A. & Bissell, M. J. Tissue  
Geometry Determines Sites of Mammary Branching Morphogenesis in Organotypic  
Cultures. *Science* **314**, 298-300,(2006).
- 83 Chanson, L. *et al.* Self-organization is a dynamic and lineage-intrinsic property of  
mammary epithelial cells.(2010).
- 84 Blagovic, K., Kim, L. Y. & Voldman, J. Microfluidic Perfusion for Regulating  
Diffusible Signaling in Stem Cells. *PLoS ONE* **6**, e22892-e22892,(2011).
- 85 Shen, Q. *et al.* Endothelial cells stimulate self-renewal and expand neurogenesis of  
neural stem cells. *Science* **304**, 1338-1340,(2004).
- 86 Bhatia, S. N., Balis, U. J., Yarmush, M. L. & Toner, M. Effect of cell-cell interactions  
in preservation of cellular phenotype: cocultivation of hepatocytes and  
nonparenchymal cells. *The FASEB journal : official publication of the Federation of  
American Societies for Experimental Biology* **13**, 1883-1900,(1999).
- 87 Khetani, S. R., Chen, A. A., Ranscht, B. & Bhatia, S. N. T-cadherin modulates  
hepatocyte functions in vitro. *FASEB journal : official publication of the Federation of  
American Societies for Experimental Biology* **22**, 3768-3775,(2008).
- 88 Huh, D. *et al.* Reconstituting Organ-Level Lung Functions on a Chip. *Science* **328**,  
1662-1668,(2010).
- 89 Nelson, C. M. & Chen, C. S. Cell-cell signaling by direct contact increases cell  
proliferation via a PI3K-dependent signal. *FEBS Letters* **514**, 238-242,(2002).
- 90 Rettig, J. R. & Folch, A. Large-Scale Single-Cell Trapping And Imaging Using  
Microwell Arrays. *Analytical chemistry* **77**, 5628-5634,(2005).
- 91 Chen, S., Patel, N., Schaffer, D. V. & Maharbiz, M. M. Trap and Corral: A two-step  
approach for constructing and constraining dynamic cell contact events in  
differentiating progenitor cell populations. *Journal of Micromechanics and  
Microengineering*. **21**,(2011).
- 92 Fukuda, J. *et al.* Micropatterned cell co-cultures using layer-by-layer deposition of  
extracellular matrix components. *Biomaterials* **27**, 1479-1486,(2006).
- 93 Chandra, R. a., Douglas, E. S., Mathies, R. a., Bertozzi, C. R. & Francis, M. B.  
Programmable cell adhesion encoded by DNA hybridization. *Angewandte Chemie* **45**,  
896-901,(2006).
- 94 Hsiao, S. C. *et al.* Direct cell surface modification with DNA for the capture of  
primary cells and the investigation of myotube formation on defined patterns.  
*Langmuir* **25**, 6985-6991,(2009).

- 95 Douglas, E. S. *et al.* DNA-barcode directed capture and electrochemical metabolic analysis of single mammalian cells on a microelectrode array. *Lab on a chip* **9**, 2010-2015,(2009).
- 96 Gartner, Z. J. & Bertozzi, C. R. Programmed assembly of 3-dimensional microtissues with defined cellular connectivity. *Proceedings of the National Academy of Sciences of the United States of America* **106**, 4606-4610,(2009).

## **Chapter 2: Non-Invasive Microfluidic Gap Junction Assay**

---

### ***2.1 Introduction***

Gap junctions are protein channels between cells that allow direct electrical and metabolic coupling via the exchange of ions, metabolites, ATP and other small aqueous molecules. Gap junctions are mostly known to be integral in the proper functioning of cardiac and neuronal systems. However, they have also been shown to be important for neural stem cells. In radial glia, gap junctional coupling via Cx43 and Cx26 is vital for neurogenesis<sup>1</sup>. Additionally, gap junctions mediate the immediate neuroprotective effects of immature neural stem cells upon transplantation into recipient brain tissue<sup>2</sup>.

Each junction is comprised of two subunits, composed of six connexin proteins each, that dock together and form an open channel between cells. There is tremendous diversity in the way they are assembled, as they can be composed of either homogeneous or heterogeneous subunits, resulting in variance in pore sizes or electrochemical regulation (voltage, pH, ionic gating)<sup>3</sup>.

The biophysical properties of a gap junction, such as their conductance or regulation by small molecules and ions, can be readily characterized. Because gap junctional communication allows the fast equilibration of low molecular weight molecules, they are widely known to be involved in the control of cell growth and cell death<sup>4</sup>, and coordinate muscle contraction<sup>5-7</sup>. It is also known that aberrant gap junction physiology, as a result of connexin downregulation, improper trafficking or genetic mutations, can contribute to cancer<sup>8</sup>, cardiac, neurological, auditory, and skin diseases<sup>9</sup>. However, new roles are continually being discovered<sup>10</sup> implying that our understanding of their physiological role is far from complete. Thus, given the dizzying array of gap junctions, the tissues in which they are present, and the molecules that pass through them, it is vital to develop fast, versatile, and high-throughput cell biology platforms for functional studies across many dimensions of parameter space.

Currently researchers employ either physical injection, scrape-loading, electrophysiological, or electroporation techniques to assess dye transfer. In the microinjection method, a microneedle is used to deliver a bolus of drug or dye into a single cell, while monitoring dye spreading into neighboring cells (Figure 2-1a). In scrape loading/dye transfer (SL/DT), a scalpel is used to make an incision into a cell monolayer, allowing the loading of dye into cells whose membrane integrity has been compromised<sup>11</sup> (Figure 2-1b). However, these methods suffer several limitations. Single-cell microinjection is very precise and quantitative, but is also very technically challenging and low throughput. A highly skilled technician can reasonably perform only a limited number of microinjections per day. At the other end of the spectrum, scrape-loading dye transfer is fast and accessible, but highly unquantitative due to uneven dye loading and poor cell viability<sup>12</sup>.

In addition, many other methods<sup>13</sup> for studying gap junction communication also exist, including electrophysiological methods, which yield insight into current conduction but not the size limits of junctional permeability, fluorescence recovery<sup>14</sup> or activation<sup>15</sup>, which can be phototoxic and expensive, or radio-labeled metabolic assays, which require cloning steps and are limited in cell type. Electroporation has also been investigated as a way of spatially isolating dye loading<sup>16,17</sup>, but it is an invasive procedure that can adversely affect cell viability<sup>18</sup>. Each of these approaches is characterized by its own advantages and disadvantages (Table 1), and the most appropriate assay will naturally be application-dependent.

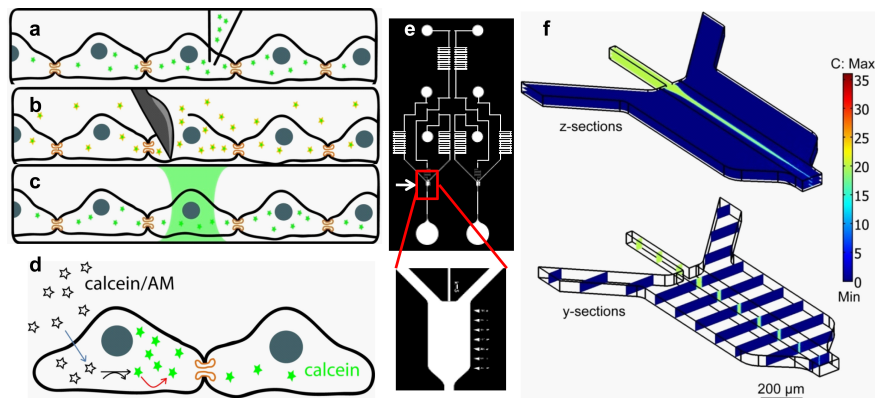


Figure 2-1. Methods for loading dye into a subset of contacting cells. Traditional approaches include microinjection (a) and scrape loading/dye transfer (b). Our approach uses microfluidic dye focusing (c), which can be achieved by focusing a stream of dye between two buffer streams. Calcein dye is used in our application because its acetomethoxy (AM) form is non-fluorescent and membrane permeable. However, once the AM ester is cleaved by intracellular esters, the molecule becomes fluorescent and can no longer exit the cell (d). This is a useful property for time-lapse monitoring. The photolithographic mask of the device is given in (e), showing the serpentine fluidic resistors at the inputs. (f) A COMSOL simulation shows dye focusing of calcein dye ( $D = 2.5 \times 10^{-10} \text{m}^2/\text{s}$ ).

Here we demonstrate a non-invasive microfluidic gap junction assay, which is repeatable, quantitative, and simple to operate. Previous microfluidic devices for assaying gap junction mediated dye transfer<sup>19</sup> work by vacuum suction trapping two cells adjacent to one another and loading calcein into one of the cells. However, this approach retains the cells in a rounded non-adherent state, in which cell-cell junctions may not be able to form. In contrast, the method we have developed integrates adherent cell culture with the subsequent assay, thus allowing the



cells ample time to adhere and express functional junctions. With this method, we can selectively deliver dye by using hydrodynamic focusing of fluids at low Reynolds number ( $Re < 1$ ) into a column of cells within a confluent cell culture chamber, and monitor subsequent dye transfer by fluorescent microscopy. Although, historically hydrodynamic focusing has long been used in flow cytometry for sorting applications, the principle has now garnered attention as a method for precise fluidic delivery of small molecules into cells<sup>20-22</sup>.

Table 1. Advantages and limitations of various gap junction assays.

Method	Advantages	Disadvantages
Microinjection	<ul style="list-style-type: none"> <li>• precise and quantitative</li> <li>• instantaneous delivery</li> </ul>	<ul style="list-style-type: none"> <li>• low throughput / time consuming</li> <li>• technically challenging</li> <li>• variation in loaded amount</li> <li>• Invasive/ minor cell damage</li> </ul>
Scrape loading/ dye transfer	<ul style="list-style-type: none"> <li>• fast and simple</li> <li>• many cells analyzed at a time</li> </ul>	<ul style="list-style-type: none"> <li>• crude and unquantitative</li> <li>• invasive/major cell damage</li> <li>• only high density cultures</li> <li>• difficult with certain morphologies</li> </ul>
gap – FRAP	<ul style="list-style-type: none"> <li>• many tracers can be used</li> <li>• quantitative permeability data</li> </ul>	<ul style="list-style-type: none"> <li>• UV damage</li> <li>• photobleaches any non-FRAP dyes</li> </ul>
LAMP	<ul style="list-style-type: none"> <li>• high spatial precision</li> <li>• high temporal precision (ms)</li> </ul>	<ul style="list-style-type: none"> <li>• limited dye selection</li> <li>• expensive</li> </ul>
Electroporation	<ul style="list-style-type: none"> <li>• only high density cultures</li> </ul>	<ul style="list-style-type: none"> <li>• unsuitable for poorly adherent cells</li> <li>• cell health concerns</li> </ul>
Microfluidic loading/ dye transfer	<ul style="list-style-type: none"> <li>• capability of spatially localizing any membrane-permeable molecule (not just dyes)</li> <li>• scalable technology</li> <li>• yields quantitative data</li> <li>• low reagent consumption</li> </ul>	<ul style="list-style-type: none"> <li>• requires specialized equipment</li> <li>• only suitable for monolayer forming cells</li> <li>• permeabilization issues, may be difficult to adapt for non-membrane permeable molecules</li> </ul>

We measure the extent of dye spread and effective diffusivities through gap junction connected cells using a quantitative microfluidic cell biology platform. After loading dye by hydrodynamic focusing of calcein/AM, dye transfer dynamics into neighboring, unexposed cells can be monitored via timelapse fluorescent microscopy. By using a selective microfluidic dye loading over a confluent layer of cells, we found that high expression of gap junctions in C6 cells transmits calcein across the monolayer with an effective diffusivity of  $3.4 \times 10^{-13} \text{ m}^2/\text{s}$ , which are highly coupled by Cx43. We also found that the gap junction blocker 18 $\alpha$ -GA works poorly in the presence of serum even at high concentrations (50  $\mu\text{M}$ ); however, it is highly effective down to 2.5  $\mu\text{M}$  in the absence of serum. Furthermore, when the drug is washed out, dye spread resumes rapidly within 1 minute for all doses, indicating

the drug does not affect transcriptional regulation of connexins in these Cx43+ cells, in contrast to previous studies. This integrated microfluidic platform enables the in situ monitoring of gap junction communication, yielding dynamic information about intercellular molecular transfer and pharmacological inhibition and recovery.

## ***2.2 Principle of Operation***

This device operates by hydrodynamic focusing of dye to spatially target the delivery of calcein dye into some cells, while leaving their immediate neighbors unperturbed. Thereafter, the subsequent transfer of dye from the targeted cells to their neighbors can be attributed to direct cytosolic transfer (Figure 2-1c). For our chosen channel geometries, the Peclet number is on the order of  $10^5$ , indicating that advective transport dominates over diffusive transport.

In our experiments we used the calcein/acetomethoxy (AM) dye which has many useful properties for our application. Calcein, a normally anionic protein, is not permeable to cell membranes. However, the AM ester modifies the carboxyl groups on the molecule, rendering it nonfluorescent and also nonpolar so that the molecules can penetrate the cell membrane. Once inside the cell, however, intracellular esterases cleave off the AM ester, thus uncaging the fluorescence and rendering the dye membrane-impermeable again. Calcein (623 Da) is known to permeate through many types of gap junctions<sup>13</sup> and can be used as a tracer in microinjection experiments<sup>23</sup>.

The properties of calcein/AM are extremely useful for our assay because once a dye molecule is loaded into a cell membrane, it can no longer diffuse back out into the extracellular environment (Figure 2-1d). Thus, any spread in fluorescence is restricted to lateral transmission through gap junctions. By timelapse-imaging the cells after dye loading, we can spatiotemporally observe the process of gap-junction mediated dye transfer. Image processing of the data yields biophysical measurements on the rate of dye transfer.

## ***2.3. Methods***

### ***2.3.1 Microfluidics Device Fabrication***

The microfluidic devices were fabricated by casting polydimethylsiloxane (PDMS) (Dow Corning Sylgard 184) against a negative master. The master was made by photolithographically patterning SU-8 2035 on a silicon wafer. The SU-8 was spincoated to a thickness of 40  $\mu\text{m}$  and exposed using a contact aligner. The masks were designed in AutoCAD and printed on mylar (40,640 DPI, Fine-line Imaging). Wafers were hard baked for 30 minutes at 150 °C and treated with trichloromethylsilane (Sigma) for 20 minutes by vapor deposition to facilitate easy removal of PDMS.

PDMS elastomer was mixed with curing agent at a standard ratio of 1:10. The polymer was then cast onto the silicon masters and cured at 60 °C for one hour. After the devices

were cut and punched with fluidic inlets, they were treated with an oxygen plasma for twenty seconds and bonded onto large #2 glass coverslips. The entire device was then bonded onto bottomless polystyrene 96-well plates (Evergreen Scientific), which served as fluid reservoirs for the inlets. A pressure controller with a manifold for 96-well plates was then used to control the pressure of the fluidic inlets (ONIX, CellASIC Inc).

### 2.3.2 Cell Culture

All HeLa and C6 cell lines are maintained in DMEM with 4.5 g/L of glucose, 10% FBS, and 1% penicillin/streptomycin at 37°C with 5% CO<sub>2</sub>. Cells are passed at 70% confluency using 0.05% trypsin with EDTA (GIBCO).

### 2.3.3 Device Operation

Assembled microfluidic devices were first UV-sterilized for two hours, then loaded with 10 µg/mL fibronectin and incubated at room temperature for 1 hour. Cells are trypsinized (0.25% trypsin with 1 mM EDTA (GIBCO)) and seeded into the culture chambers at high density (10 million cells/mL) from the outlet at 0.1 PSI. The device is then detached from the manifold and the cells are cultured to confluence (about 2-4 days) in a standard incubator (37 °C and 5% CO<sub>2</sub>). Gravity-driven flow of the media (400 µl) provided at the inlet reservoirs ensures that the cells are continually perfused with fresh media at a flow rate of approximately 0.2 µL/s, as measured by particle tracking inside the chambers.

Once the cells grow to confluence, all reservoirs are loaded with CO<sub>2</sub>-independent medium (GIBCO), supplemented with 1% penicillin/streptomycin (GIBCO), to replace the original DMEM media. An additional 0.05% DMSO is added to the media to control for the additional DMSO when the gap junctional blocker 18α-glycyrrhetic acid is added. Calcein/AM (Invitrogen) is dissolved in DMSO (Sigma-Aldrich) and diluted into the culture medium to 20 µM. In some experiments, the lipophilic DiI dye is also added to this dye solution to a final concentration of 5 µM. This dye solution is then loaded into the central reservoir. The dye is hydrodynamically focused over the cultured cells by applying high pressure (3.1 PSI) onto the side channels and low pressure (0.1 PSI) into the middle channel. After 5 minutes of dye loading, the dye stream is stopped and timelapse images are taken at 1 frame per minute for 25 minutes. Forward pressure in the buffering streams is maintained at 0.11 PSI to prevent backflow of dye-laden solution.

For 18α-glycyrrhetic acid (18α-GA) experiments, cells are treated with the drug in a cell culture incubator for 30 minutes. All 18α-GA stocks are prepared the day of the experiment, to a stock concentration of 100 mM. After treatment, the cells are then subjected to the same dye focusing protocol as detailed above. After the dye loading and 25 minute timelapse, fresh media is flowed through to wash out the 18α-GA concurrently with continued imaging.

### 2.3.4 Fluorescence Imaging and Data Analysis

Quantitative fluorescence imaging of cells was performed using a Zeiss AxioObserver Z1 microscope with a Hamamatsu 9100-13 EMCCD camera. Image acquisition was automated using iVision (BioVision Technologies). Five line profiles per data set were chosen manually based on high fluorescence in the dye-loaded cells, to ensure a high signal-to-noise ratio and so that no cell was represented twice.

## 2.4. Results

### 2.4.1 Device Design, Simulation, and Characterization

The design of the device was constrained by the target width of dye focusing, the minimum pressure that can be applied by our flow controller and the maximum shear that can be reasonably experienced by C6 glioma cells. Previous research has shown that glioma cells can be cultured under shear conditions up to 32 dynes/cm<sup>4</sup>, so we chose a threshold of at most 5 dynes/cm. The target width of the dye stream is approximately the width of one adherent cell, in this case, 25 μm. Although subcellular resolution has been achieved<sup>20</sup>, those widths are unnecessary for our application, since we are investigating transport between cells.

We use a pneumatic flow controller to actuate the liquid in our devices. Because the digital resolution of our pneumatic flow controller is 0.1 PSI, or around 0.7 kPa, the effective fluidic resistance of the device must be high in order to supply low flowrates. Using lumped element modeling and assuming a Poiseuille flow profile, we approximate the resistance of a fluidic channel by:

$$R = \frac{12L\eta}{Wh^3} \quad (2-1)$$

where  $\eta$  is the viscosity of solution,  $L$  is the length of the channel,  $W$  is the width, and  $h$  is the height<sup>24</sup>. Using this equation and the constraints on flowrate ratios, we designed serpentine channel resistors (49 x 0.1 x 0.05 mm) at each inlet (Figure 2-1e), with resistances up to 790 Pa/(uL/min), resulting in a final flow velocity in the cell culture chamber of approximately 0.07 cm/s (3 dynes/cm<sup>2</sup>). Empirical characterization of the bare devices showed that 25 μm dye widths can be achieved by applying 0.1 PSI of pressure at the central inlet and 3.1 PSI of pressure at the outer inlet (Figure 2-2a-b).

With these parameters, finite element simulations also verified hydrodynamic focusing of the central dye stream with sharp boundaries (Figure 2). Simulations were run assuming incompressible Navier-Stokes flow and a diffusion constant of 2.5 x 10<sup>-10</sup> m<sup>2</sup>/s for calcein<sup>25</sup> (Figure 2-1f)

One central concern was that a cell monolayer on the bottom surface of the device chamber would introduce topographical variations that would disturb the flow profile

significantly. Experimental validation shows that even with HeLa cells cultured in the chambers, the dye is still focused with sharp boundaries to  $24 \pm 6 \mu\text{m}$  (mean  $\pm$  SD,  $n = 4$ ) using the pressures previously determined (Figure 2-2-d). HeLa cells are reported to have downregulated connexin expression, so after 5 minutes of dye loading, and 10 minutes of incubation, the calcein dye is concentrated in the middle of the chamber. DiI dye, a lipophilic membrane dye, was also used as a control to track the spatial localization of the central dye stream (Figure 2-2e).

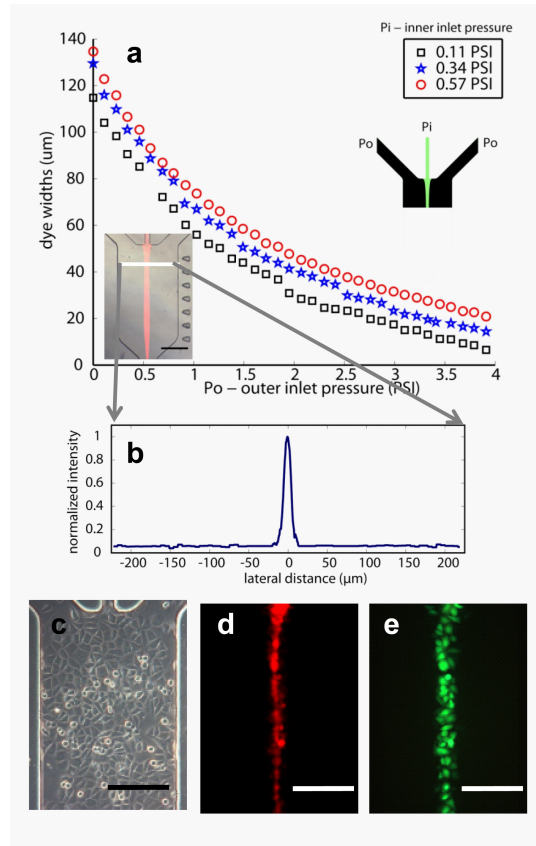


Figure 2-2. Dye focusing in bare devices and over confluent cells. Various widths of dye focusing can be achieved with the device by modulating the pressure at the outer inlets with respect to the inner inlet (a). At  $P_i = 0.11$  PSI, and  $P_o = 3.1$  PSI, dye in bare channels can be focused to a width of  $20 \mu\text{m}$  (b). Dye focusing over HeLa cells show that calcein/AM and DiI dye can be focused over cells in the center of the channel (c-e). Scale bar:  $200 \mu\text{m}$ .

Because DiI is restricted to the membrane and cannot be transferred to adjacent cells, the DiI serves as a control to ensure that dye streams are not mixing in the chamber. The DiI fluorescence is more concentrated to the middle of the chamber, indicating that HeLa cells may have some low level of gap junction expression. However, it is more likely that this result reflects the much lower diffusivities of DiI in solution ( $2.5 \times 10^{-11} \text{ m}^2/\text{s}$ ) or in cell membranes ( $3.8 \times 10^{-12} \text{ m}^2/\text{s}$ ).

Although the presence of cells on the bottom surface of the microfluidic device does not significantly affect sharpness of the dye peak, the cells do disturb the path of the central

dye stream, offsetting it from the center of the chamber, or introducing a slight curvature. These disturbances are unavoidable and in subsequent dye transfer experiments, we account for this variation simply by measuring all dye spread distances from the peak, even if the peak deviates from the center.

One major advantage of the microfluidic approach is that dye loading can be accomplished in an entirely noninvasive way, while also yielding dynamic information about the process of dye transfer. In addition, the operation of this device is extremely simple, requiring no syringe pumps or tubing, which can be bulky to transport and can introduce deleterious bubbles into the system, as explained below.

With a pneumatic pressure controller, bubbles rise to the air-liquid interface which is separated from the fluidic inlet by the height of liquid present in the reservoir. Since it is easy to disengage the device from the pressure flow controller, extended periods of cell culture can be performed on-chip, without the potential bubble problems that can arise when re-interfacing microfluidic chips with tubing for syringe pumps. Though we use a commercially available pressure controller to actuate the flow inside the microdevice, it is entirely possible to actuate the device by simply applying a vacuum at the outlet, requiring no more than a standard vacuum line and a vacuum controller or vacuum gauge. Additionally, master molds of this feature size can easily be fabricated using simple materials such as shrinky dinks<sup>26</sup> or through a public foundry<sup>27</sup>. Thus, the technique is extremely accessible even to researchers outside of the microfluidics community.

#### *2.4.2 Dye Transfer in Cx43+ C6 Glioma*

After validating that dye focusing is intact even over confluent cells, we investigated the dynamic spread of dye in C6 glioma cells stably transfected with connexin43 (Cx43). As typical of many cancer cell types, the wildtype C6 glioma cells have downregulated the expression of gap junctions. Biochemical characterization of Cx43 protein levels has been previously performed elsewhere<sup>17</sup>.

We characterized the spread of calcein dye in Cx43+ C6 cells, wildtype C6 cells, and Cx43+ C6 cells which have been treated with the gap junction blocker, 18 $\alpha$ -glycyrrhetic acid. The Cx43+ C6 cells show extensive lateral transfer of calcein dye (Figure 2-3b, Figure 2-4b), compared to the wildtype cells (Figure 2-3a, Figure 2-4a). After treatment with 18 $\alpha$ -GA, the same Cx43+ cells are assayed, revealing a drastic reduction in dye spread (Figure 2-3c, Figure 2-4c). The fluorescence profiles across the chamber are given for multiple points along the chamber (Figure 2-3) and over time (Figure 2-4), yielding dynamic information about gap junctional transfer of dye.

By plotting the average dye spread over time (Figure 2-5a), we can see that calcein travels approximately 50  $\mu\text{m}$  through the Cx43+ C6 cells in 25 minutes. We discovered in these experiments that dye transfer is greatly reduced, but not completely abolished, when incubated with 50  $\mu\text{M}$  18 $\alpha$ -GA in serum-containing media. Using the equation for the diffusion length,  $L = \sqrt{4Dt}$ , we can calculate an effective diffusivity, plotted in Figure 5b. This calculation yields an effective diffusivity of  $3.4 \times 10^{-13} \text{ m}^2/\text{s}$  for the Cx43+ cells, translating to a reduction of two

orders of magnitude in the diffusivity of calcein in cell cytosol<sup>27</sup>. When gap junctions are blocked by 18 $\alpha$ -GA, the diffusivity drops slightly, to approximately  $1.2 \times 10^{-13} \text{ m}^2/\text{s}$ .

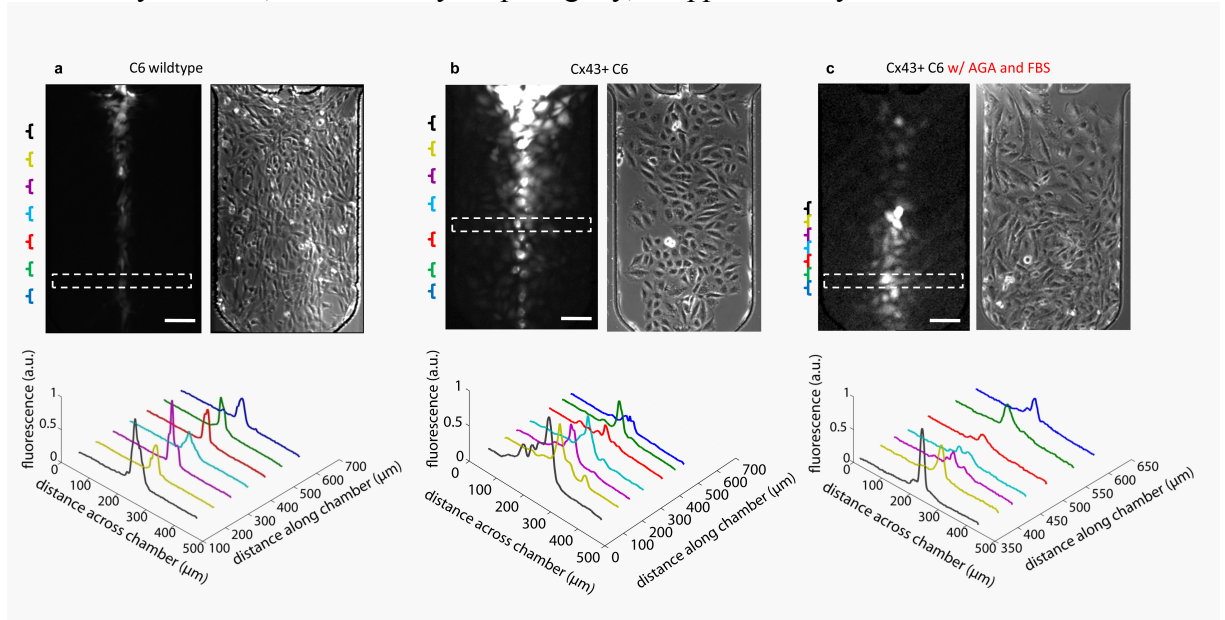


Figure 2-3 Fluorescence intensity profiles across the cell chamber, 30 minutes after dye loading. Each profile is the column average of the area Cx43-negative wild-type C6 cells (a) do not exhibit any dye spread, at any point along the chamber. Cx43+ C6 cells (b) show extensive dye transfer, as evidenced by the multiple fluorescent peaks across the chamber. The presence of gap junction blocker 18 $\alpha$ -GA inhibits dye transfer (c). Fluctuations in peak intensity can be attributed to fluctuations in the intensity of the illumination source. Scale bar: 100  $\mu\text{m}$

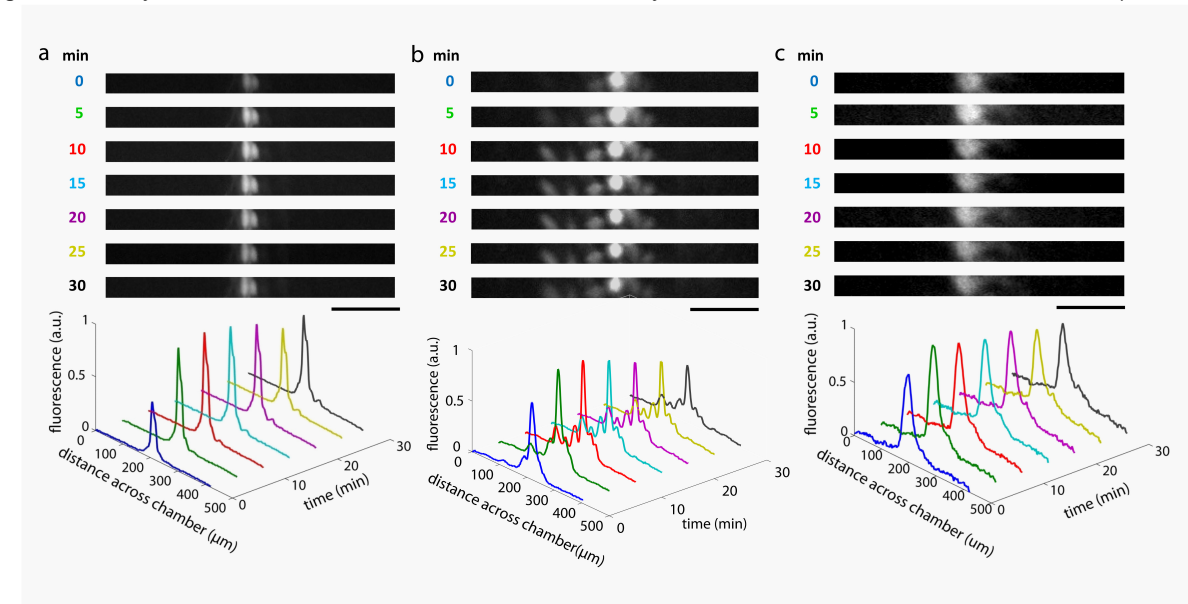


Figure 2-4 Fluorescence intensity profiles over time of a given region-of-interest for the different cell types. The profile plotted is a column average of the area (20 pixels width) given in the white dashed box in Figure 3. Wildtype C6 cells (a) show no spreading over 30 minutes, while Cx43+ cells (b) show a decrease in the fluorescence of the central peak, with a corresponding increase in the fluorescence of neighboring cells. 18 $\alpha$ -GA exposure inhibits dye spread (c). Scale bar: 100  $\mu\text{m}$

However, we found that when the Cx43+ cells are treated in 18 $\alpha$ -GA in the absence of serum, the efficacy of the drug is greatly increased (Figure 2-6). Without serum, dye transfer was completely blocked down to 5  $\mu$ M (Figure 2-6e). The observation that serum blocked the activity of the inhibitor corroborates with the studies done on alveolar epithelial cells<sup>28</sup> and on fibroblasts<sup>29</sup>. Both of these studies showed that the presence of serum required concentrations of 18 $\alpha$ -GA over 50  $\mu$ M in order to block gap junction activity.

In the dose response study, we found that the drug is half-maximally effective at 0.5  $\mu$ M. At this concentration, the pEC50 was  $3.8 \times 10^{-14}$  m<sup>2</sup>/s, about halfway in between the maximum ( $3.4 \times 10^{-13}$  m<sup>2</sup>/s with no drug), and the minimum ( $1.78 \times 10^{-15}$  m<sup>2</sup>/s for 50  $\mu$ M).

After 25 minutes of incubation in the drug-containing media, we washed out the drug using serum-containing media and continue the timelapse for another 25 minutes. These experiments showed that the dynamics of recovery are extremely fast for all doses. Within one minute of the washout, lateral dye spread was detectable for all doses, asymptotically approaching the maximum within 25 minutes (Figure 2-6a-d). The fast dynamics of this recovery for all doses indicates that the primary blocking action of glycyrrhetic acid is biochemical and not transcriptional in nature, as seen in other cell types at high concentrations<sup>28</sup> (see Section 1.5).

The low effective value of calcein diffusivity provides good evidence that any spread of fluorescence is not a result of lateral calcein diffusion in the extracellular media, which would be much faster. Two other results which verify that the dye spread is indeed gap junction-mediated are shown in Figure 2-7. In one set of experiments using Cx43+ C6 cells, we see that a relatively isolated cluster of cells exhibits very low fluorescence compared to other cells at the same distance away from the center. This cluster is connected to the main body of cells through only one cell, thus drastically reducing the number of gap junctional connections that can be made. If the dye could travel by extracellular diffusion, then cellular fluorescence would be independent of membrane contact and dependent only on distance from the midline. Since we see almost no fluorescence in these isolated cells, we confirm that there is no extracellular diffusion. The second result is that membrane-localized DiI dye that is loaded concurrently with the calcein/AM dye shows no spread after 30 minutes of incubation, affirming that the apparent lateral diffusion is not an artifact of diffusive smearing in the laminar streams above the cells. Thus, we conclude that all diffusive spread of dye in our experiments is wholly dependent on direct cytosolic intercellular transfer.



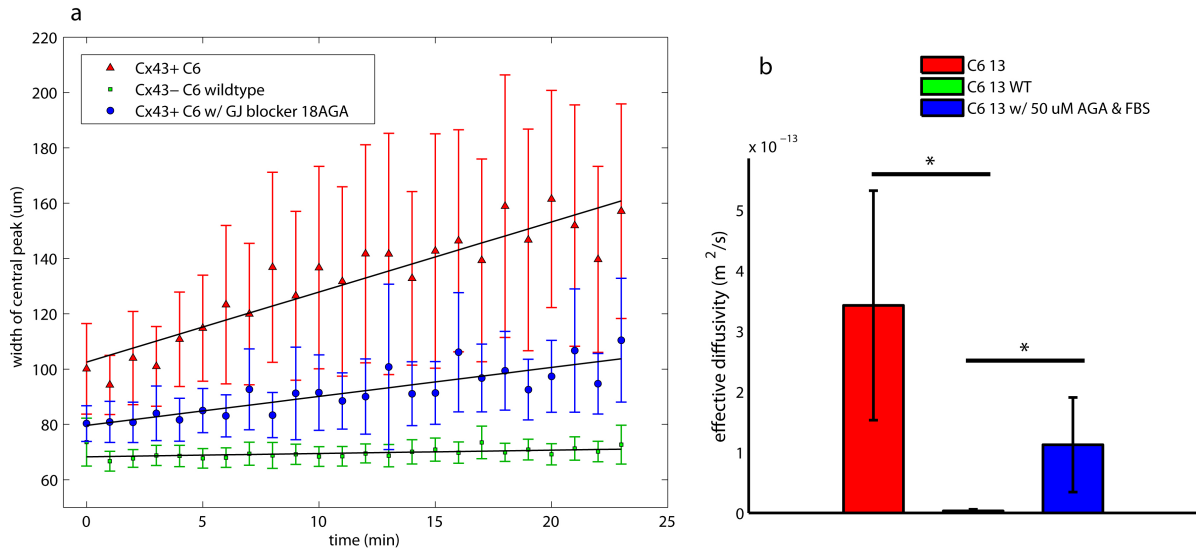


Figure 2-5 Dye spread and effective diffusivity for Cx43+ C6 cells, wildtype C6 cells, and Cx43+ cells that have been treated with the gap junction blocker 18 $\alpha$ -GA. For (a), dye spread is defined as width of the central fluorescent peak, measured at the point where the fluorescent intensity drops to 36.9% (1/e). Cx43+ C6 cells transfer the dye much further than wildtype C6 cells (error bars denote the standard deviation). Treatment of cells with 18 $\alpha$ -GA greatly decreases the dye spread, but does not completely abolish it. In (b), the effective diffusivity is shown, indicating an increase in two orders of magnitude from wildtype C6 cells to Cx43+ cells. Treatment of cells with 18 $\alpha$ -GA lowers the effective diffusivity by an order of magnitude. (n = 3 \* indicates p<0.05).

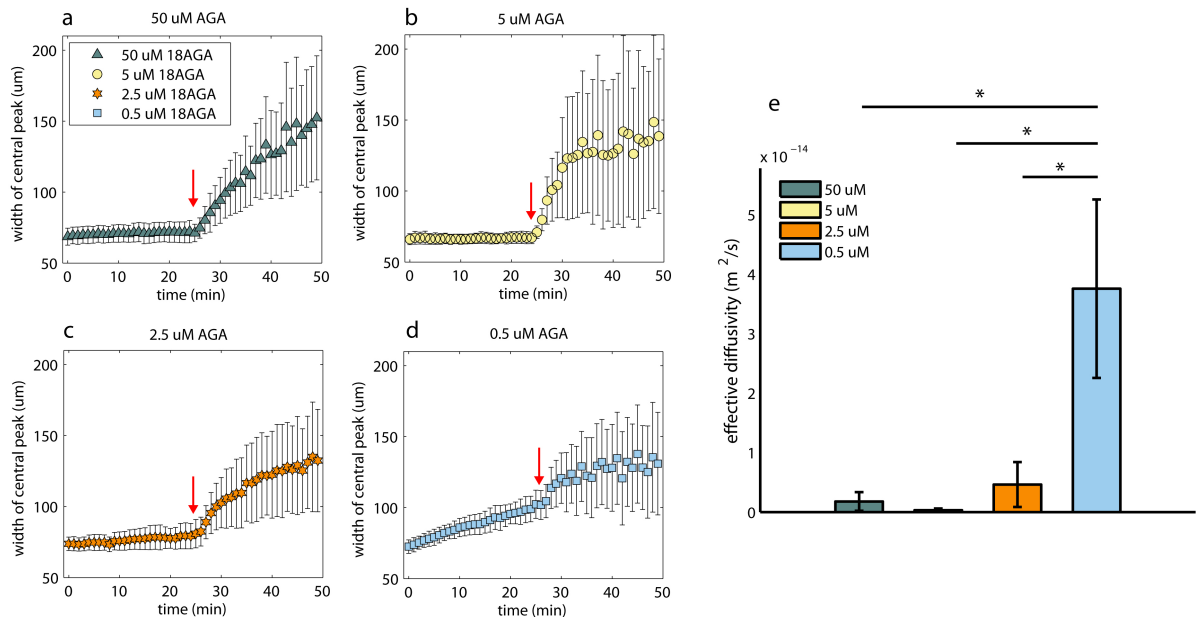


Figure 2-6 Dose response of 18 $\alpha$ -GA and washout experiment in medium without serum. Four concentrations of 18 $\alpha$ -GA were tested (50  $\mu$ M, 5  $\mu$ M, 2.5  $\mu$ M, and 0.5  $\mu$ M) (a). Dye spread (defined as in Figure 5) is inhibited for all concentrations except 0.5  $\mu$ M. Red arrows indicate the time of drug washout, at which point dye spread commences for all. Effective diffusivities are given in (b). (n = 3, \* indicates p<0.05).

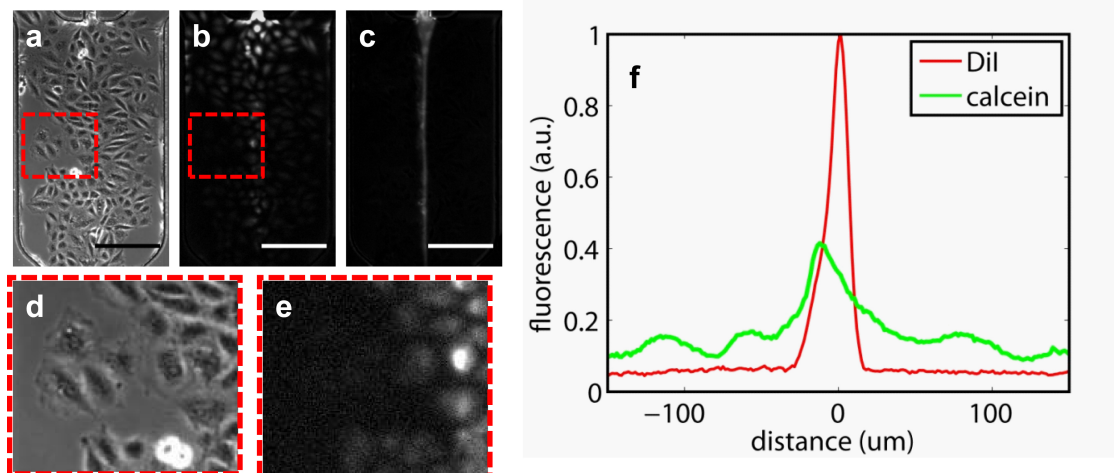


Figure 2-7 Further evidence that dye transfer is indeed gap junction mediated. An isolated 3-cell island shows little fluorescence due to a paucity of connections, showing that dye spread is indeed gap junction mediated (a, b, d, e). Additionally, 30-minute endpoint plots (f) of calcein fluorescence (b) and DiI (c) fluorescence in the chamber show that calcein is distributed across the entire chamber whereas the membrane-localized DiI dye is only present in cells in the middle of the chamber. This data set was not included in the analysis for Figure 5.

## 2.5 Discussion

The quantitative studies done here show that gap junction connected cells allow the transfer of small molecules, such as calcein dye, with an effective diffusivity of  $3.4 \times 10^{-13} \text{ m}^2/\text{s}$ . The gap junction blocker  $18\alpha\text{-GA}$ , though clearly inhibiting gap junction communication, does not completely block gap junction communication, resulting in a final effective diffusivity of  $1.2 \times 10^{-14} \text{ m}^2/\text{s}$ .

The results of the washout study contrasts with a dose response study done in alveolar cells<sup>28</sup>, in which high doses ( $> 10 \mu\text{M}$ ) of  $18\alpha\text{-GA}$  maintained for 30 minutes resulted in the disassembly of gap junctional plaques. Removal of the drug in this case did not induce the reassembly of gap junction plaques. However, our results show that Cx43+ C6 cells do not experience long-term reduction in gap junction coupling when treated with  $18\alpha\text{-GA}$ . In fact, these cells begin exhibiting dye spread immediately ( $< 1 \text{ min}$ ) after the drug washout, completely independent of the initial drug dose. The faster dissociation of the drug in our device could be a direct result of the physical shear from continuous flow of fresh media during washout. Future iterations of this device with finer resolution on flow speed could elucidate the shear-dependence of this recovery. Another possible explanation for the discrepancy in results could be that the drug induces transcriptional feedback to downregulate gap junction expression in the other cells, but not in C6 cells. More detailed comparative studies are required to confirm these possible interpretations.

In our study, we restrict the analysis of dye transfer to the x-dimension, based on the assumption that dye loading down the central column of cells is relatively even, and that dye transfer only occurs laterally. However, since diffusion occurs in 2D, the study can be easily extended by using more advanced image processing algorithms to detect individual cell boundaries and map the total

fluorescence in each cell at each timepoint to accurately measure the flux between cells. Connexin molecules can be GFP-tagged or stained *in situ* to provide yet another measure of the relative gap junctional density at each cell boundary.

Although our study investigates only the transfer of calcein/AM particles, many other types of molecules can also be potentially loaded by conjugating them to an AM moiety or potentially by encapsulating them in liposomes, which fuse with the cell membrane to deposit their contents inside the cell. The spatially defined delivery of these molecules allows researchers to visually track signal transduction through any lateral cell signaling pathway, such as through connexins, pannexins, adherens junctions, desmosomes, and Notch/Delta signaling. The microfluidic architecture, as opposed to microinjection for instance, is advantageous in these cases because the continuous flow can aid in decoupling lateral signaling from secreted factor signaling. Additionally this platform makes it simple to perform washout experiments *in situ*, enabling the continuous monitoring of physiological processes with very fast dynamics. Since the modulation of gap junctions in intercellular communication are potential pharmacological targets, our microfluidic platform for gap junction analysis can be useful for the multiplexed functional screening of connexin mutations.

## 2.5 References

- 1 Kunze, A. *et al.* Connexin expression by radial glia-like cells is required for neurogenesis in the adult dentate gyrus. *Proc Natl Acad Sci U S A* **106**, 11336-11341,(2009).
- 2 Jäderstad, J. *et al.* Communication via gap junctions underlies early functional and beneficial interactions between grafted neural stem cells and the host. *Proceedings of the National Academy of Sciences of the United States of America* **107**, 5184-5189,(2010).
- 3 Lodish, H. F. *Molecular Cell Biology*. (W.H. Freeman, 2008).
- 4 Clair, C. *et al.* Investigation of the roles of Ca<sup>2+</sup> and InsP<sub>3</sub> diffusion in the coordination of Ca<sup>2+</sup> signals between connected hepatocytes. *J Cell Sci* **114**, 1999-2007,(2001).
- 5 Reinecke, H., MacDonald, G. H., Hauschka, S. D. & Murry, C. E. Electromechanical coupling between skeletal and cardiac muscle. Implications for infarct repair. *J Cell Biol* **149**, 731-740,(2000).
- 6 Haefliger, J.-A., Meda, P. & Nicod, P. Contribution of connexins to the function of the vascular wall. *Cardiovasc Res* **62**, 345-356,(2004).
- 7 Rohr, S. Role of gap junctions in the propagation of the cardiac action potential. *Cardiovasc Res* **62**, 309-322,(2004).
- 8 Holder, J. W., Elmore, E. & Barrett, J. C. Gap junction function and cancer. *Cancer Res* **53**, 3475-3485,(1993).
- 9 Winterhager, E. *Gap junctions in development and disease*. (Springer-Verlag, 2005).
- 10 Robinson, Vaney, D. I., Hampson, E. C. & Munro, M. N. Unidirectional coupling of gap junctions between neuroglia. *Science* **262**, 1072-1074,(1993).
- 11 Chang, C. C., Trosko, J. E. & el-Fouly, M. H. Scrape-loading and dye transfer. A rapid and simple technique to study gap junctional intercellular communication. *Experimental Cell Research* **168**, 422-430,(1987).
- 12 Doolittle & McKarns. Limitations of the scrape-loading/dye transfer technique to quantify inhibition of gap junctional intercellular communication. *Cell Biology and Toxicology* **8**, 89-103,(1992).
- 13 Abbaci, M., Barberi-Heyob, M., Blondel, W., Guillemin, F. & Didelon, J. Advantages and limitations of commonly used methods to assay the molecular permeability of gap junctional intercellular communication. *BioTechniques* **45**, 33-52, 56-62,(2008).
- 14 Trosko, J. E., Schindler, M. & Wade, M. H. A fluorescence photobleaching assay of gap junction-mediated communication between human cells. *Science* **232**, 525-528,(1986).
- 15 Dakin, K., Li, W.-H. & Zhao, Y. LAMP, a new imaging assay of gap junctional communication unveils that Ca<sup>2+</sup> influx inhibits cell coupling. *Nat Meth* **2**, 55-62,(2005).
- 16 Anagnostopoulou, A., Vultur, A., Cao, J., Firth, K. & Raptis, L. Examination of gap junctional, intercellular communication by in situ electroporation on two co-planar indium-tin oxide electrodes. *Molecular Oncology* **1**, 226-231,(2007).
- 17 Naus, C. *et al.* In Situ Bipolar Electroporation for Localized Cell Loading with Reporter Dyes and Investigating Gap Junctional Coupling. *Biophysical Journal* **94**, 469-479,(2008).
- 18 Canatella, P. J., Karr, J. F., Petros, J. A. & Prausnitz, M. R. Quantitative study of electroporation-mediated molecular uptake and cell viability. *Biophys J* **80**, 755-764,(2001).
- 19 Jan, L., Lee, L. P., Hung, P. J., Lee, P. J. & Shaw, R. Microfluidic application-specific

- integrated device for monitoring direct cell-cell communication via gap junctions between individual cell pairs. *Applied Physics Letters* **86**, 223902-223903,(2005).
- 20 Ingber, D. E. *et al.* Laminar flows: Subcellular positioning of small molecules. *Nature* **411**, 1016-1016,(2001).
- 21 Folch, A., Tourovskaia, A. & Figuroa-Masot, X. Differentiation-on-a-chip: A microfluidic platform for long-term cell culture studies. *Lab on a chip* **5**, 14-19,(2005).
- 22 Lu, C. *et al.* Microfluidic delivery of small molecules into mammalian cells based on hydrodynamic focusing. *Biotechnology and bioengineering* **100**, 150-158,(2008).
- 23 Eckert, R. Gap-junctional single-channel permeability for fluorescent tracers in mammalian cell cultures. *Biophysical Journal* **91**, 565-579,(2006).
- 24 Senturia, S. D. *Microsystem design*. (2001).
- 25 Lyman, W. J., Reehl, W. F. & Rosenblatt, D. H. *Handbook of chemical property estimation methods: environmental behavior of organic compounds*. (McGraw-Hill, 1982).
- 26 Chen, C. S. *et al.* Shrinky-Dink microfluidics: 3D polystyrene chips. *Lab Chip* **8**, 622-624,(2008).
- 27 Weibel, D. B., Whitesides, G. M. & DiLuzio, W. R. Microfabrication meets microbiology. *Nat Rev Micro* **5**, 209-218,(2007).
- 28 Martinez-Williams, C., Rannels, D. E., Gilbert, K. A. & Guo, Y. Inhibition of gap junction communication in alveolar epithelial cells by 18alpha -glycyrrhetic acid. *Am J Physiol Lung Cell Mol Physiol* **276**, L1018-1026,(1999).

## **Chapter 3: Trap and Corral: A Two-Step Approach For Constructing And Constraining Dynamic Cell Contact Events In Differentiating Progenitor Cell Populations**

---

### ***3.1 Introduction***

Cells are constantly subjected to a host of external signals which can influence their state, and thus phenotype and behavior. Mammalian cells are dependent on signals from surrounding cells to maintain viability, proliferate, and coordinate their actions. During developmental and regenerative processes, these lateral signals between cells provide instructive cues informing stem cells how, when, and where to differentiate.

Localized intercellular cues can formally be categorized into paracrine and juxtacrine signals. In paracrine signaling, the signaling molecules are diffusible ligands, which are secreted by the sender cell. The docking of ligands to the receptors of the target cell triggers the signal transduction cascade that eventually regulates the gene transcription of the target cell and drives differentiation. In juxtacrine signaling, direct cell-to-cell contact is required for the signaling to take place because both ligands and receptors are membrane-bound. Many canonical juxtacrine signaling pathways, such as the Notch pathway<sup>1</sup>, the Wnt pathway, and the Eph-Ephrin pathway<sup>2,3</sup> play crucial roles in specifying fates during early development and regenerative processes during adulthood<sup>4</sup>.

To study these juxtacrine signaling processes *in vitro*, it is desirable to be able to controllably place individual cells into contact. Most methods to create small-scale cell assemblies are

based on microfabrication technologies (although cellular self-assembly using DNA-conjugated surface proteins have also been reported<sup>5</sup>). In general, two types of approaches have been used to bring discrete numbers of cells together. In one approach, surface micropatterning is used to create cytophobic and cytophilic regions. Surface patterning is typically done using self-assembled monolayers of thiols on gold<sup>6-8</sup>, selectively masked vapor deposition of metals<sup>9</sup>, laser ablation<sup>10</sup>, direct-write processes<sup>11,12</sup>, or photolithographic processes<sup>13,14</sup>. The other approach is to constrain cells mechanically using 3D structures such as microwells<sup>15,16</sup> and microfluidic traps<sup>17,18</sup> to arrange cells into spatial proximity.

Self-assembled monolayers (SAMs) patterned in bowtie shapes have been used successfully to study the effect of cell-cell contact in endothelial cell proliferation<sup>7</sup>. However, thiol patterning techniques generally suffer from low yield and degrade over time<sup>19</sup>. Similar approaches using poly-ethyleneglycol(PEG) hydrogels resist degradation but still suffer from poor efficiency in their ability to pair cells<sup>8,16</sup>. Typically, the distribution for each type of pattern follows a Poisson distribution with lambda equal to the desired number of cells. Thus, the best reported efficiencies for capturing two cells peak at around 35-40%<sup>7,8</sup>. Microscopy-based *in situ* photolithography<sup>13</sup> appears to have good capture efficiencies but the exact numbers are not reported.

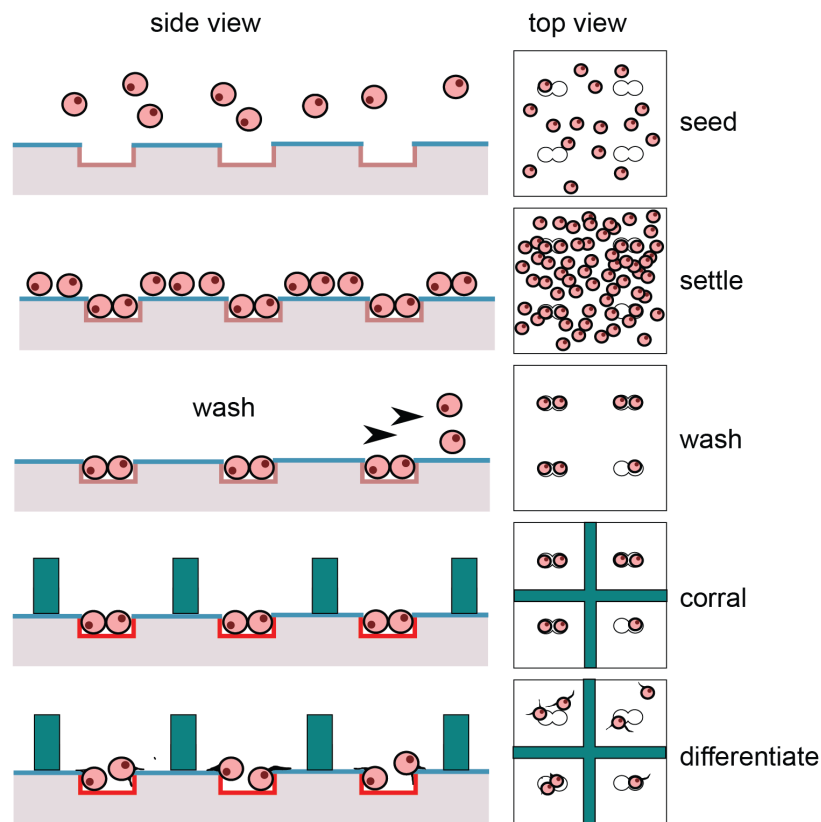


Figure 3-1 The experimental scheme showing cells seeded onto the microwells at high density before washing and corralled. Differentiating these cells in mixed differentiation medium results in outward migration (shown in the bottom panel) over the course of several days.

Three-dimensional structures are more successful at capturing well-defined numbers of cells. Skelley et al. achieved up to 70% pairing efficiencies using a microfluidic design for high-yield electrofusion. However, the patterning is not preserved after long-term culture in the device (up to 3 days)<sup>18</sup>.

While these microdevices and substrates can place cells in proximity, cell contact is generally difficult to constrain for long periods *in vitro* without influencing viability or artificially altering cell state, especially for durations of time that are likely necessary to bias fate decisions. Often, markers of differentiation are not detectable by mRNA screening methods or immunocytochemistry until 2- 5 days after the initial stimulus to differentiate. Moreover, both *in vivo* and unconstrained *in vitro* experiments, differentiating cells often experience cell-cell contact events interspersed with bouts of motility, process extension and multicellular aggregation<sup>1</sup> which are not recapitulated in simple cell capture devices<sup>17</sup>.

Specifically, we are interested in understanding how cell-cell contact events bias differentiation in adult neural stem cells of various population sizes prior to the emergence of neuronal, glial and oligodendrocytic precursors. We address this problem by using a two-step process involving microwells to trap cells with high efficiency followed by the alignment of a PDMS mesh around the cells to corral them after the trapping. The microwells trap single cells and paired cells with the highest reported efficiencies, up to 90% and 80%, respectively. After seeding, the PDMS mesh is brought down using an alignment jig to create a 150  $\mu\text{m}$  x 150  $\mu\text{m}$  corral around each trap so that when cells migrate out of the well, they cannot make contact with cells from neighboring traps. The corraling must be done in liquid after seeding because the seeding requires high cell densities to achieve near-full occupancy in the wells. Low-density seeding of the PDMS corrals alone can result in two cells being trapped in each well, but in those conditions, the two cells often engage in very little contact or none at all (and seeding obeys a non-desirable Poisson distribution). By contrast, trapping cells and then corraling them proves to elicit higher contact times.

## **3.2. Materials and Methods**

### **3.2.1 Polystyrene Microwell Fabrication**

A preliminary experiment using PDMS microwells to trap NPCs showed that over 50% of trapped NPCs exhibited apoptosis over 4 days. We assumed that this phenomenon was a result of the accumulation of excess contaminants and toxic intermediates (See Chapter 1.3) including low-molecular weight PDMS oligomers. Thus, we used the same dimensions of microwells but fabricated them out of PS, which is known to be permissive for cell growth.

The polystyrene (PS) microwells are fabricated according to a previously published hot embossing technique<sup>20</sup>. The technique uses PDMS pillars as a mold, because PDMS is elastically deformable and does not melt at the high temperatures necessary to emboss polystyrene. During this process, the polystyrene must be heated to 180°C (above the  $\sim 100^\circ\text{C}$ <sup>21,22</sup> glass transition temperature but below its melting point of 240°C).



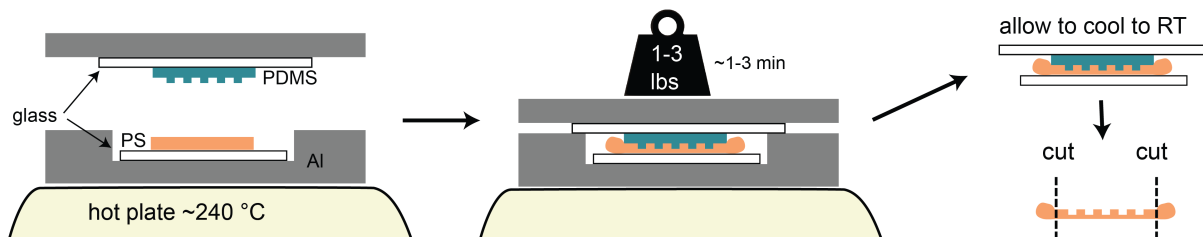


Figure 3-2 The fabrication of microwells in polystyrene is done by hot embossing a PDMS master onto polystyrene. The assembly is sandwiched between a set of custom-milled aluminum blocks, on which free weights are placed to apply pressure.

An inexpensive benchtop press is constructed using a laboratory hot plate (Thermo Scientific, Cimarec) and two flat blocks of aluminum. The bottom block is milled to create a 2 cm x 2 cm x 0.3 cm indent for holding a glass slide cut to size. The glass slide is clean and ensures that the bottom surface of the polystyrene will be flat and optically clear after embossing. Four holes are drilled in the corners of the aluminum blocks and metal dowels are inserted as guide rails. The hot plate is heated to 250-270°C, so that the surface temperature on the bottom block is 180°C (measured with a thermocouple).

Polystyrene coupons are cut to 1.5cm x 1.5 cm and washed in IPA and water. A clean glass slide is inserted into the indent and a PS coupon is quickly placed in the center of the slide. A 0.28 mm thick PDMS mold that has been plasma bonded to a large glass slide is then inverted on top of the PS coupon. The top block of aluminum is aligned on top using the guide rails and gently brought down onto the assembly. A 1-lb free weight is then placed on top, resulting in a final pressure of 32 kPa. After two minutes, two more 1-lb weights are placed on top, resulting in a final pressure of 72 kPa. After 5 minutes, the weights are removed and the entire assembly is quickly taken off the heated aluminum block. After cooling, the embossed chip is removed and cut to size by scoring the edges and breaking the edges carefully with a pair of pliers. The PDMS mold can be reused >30 times.

The PDMS pillars used for embossing the PS coupons are made using standard soft lithography protocols. Briefly, an SU-8 mold is made by spinning SU-8 2015 to a thickness of 10 μm on a silicon test wafer using a Headway spinner. The wafer is then soft-baked and exposed on a Karl Suss MA6 Mask Aligner. After post-baking the wafer is developed in SU-8 developer and washed with IPA and water. The wafer is hard-baked at 150°C for 10-30 minutes to anneal thermal cracks and to improve adhesion to the substrate. The wafer is then coated with trichloro(1H,1H,2H,2H-perfluorooctyl)silane (Sigma) by vapor deposition under a vacuum-trapped house vacuum line for 1 hour. This step is integral because if the wafer is incompletely coated, PDMS does not release from the mold, resulting in defective pillars and a permanently damaged SU-8 mold. PDMS is cured to a height of 0.28 mm on the wafer in a convection oven at 60 °C for 1 hour.

### 3.2.2 Alignment Jig Fabrication and Assembly

The alignment jig is designed in AutoCAD Student 2010 (See Appendix B) and rapidly prototyped in an aluminum alloy (First Cut). Because the alloy contains reactive metals that

form salt precipitates with the anions that are typically present in any cell culture medium, the entire jig is coated in parylene, a chemically inert and biologically compatible polymer. The jig is sonicated in IPA for 30 minutes, and washed 3X in DI water, before coating with 10  $\mu\text{m}$  of parylene C in the Parylene Deposition System 2010 LabCoter 2.

The top part of the alignment jig is aligned onto the mesh within a 100- $\mu\text{m}$  wide square of SU-8 that has been patterned to match the size of the ridge on the underside of the top piece. Then the entire assembly is cured at 60  $^{\circ}\text{C}$ . The top piece of the alignment jig is then peeled off the SU-8 mold carefully, bringing the PDMS mesh with it.

The polystyrene microwells are aligned under the mesh using a stereomicroscope (Zeiss) and held in place by conformal contact. PDMS is applied to a small ring around the viewing hole on the bottom piece and the bottom and top pieces of the alignment jig are then brought together. The assembly is then cured in the convection oven at 60  $^{\circ}\text{C}$  for 1 hour. When the top part of the jig is removed, the polystyrene microwells remain adhered to the bottom piece of the jig.

### *3.2.3 Mesh Fabrication*

Briefly, a 1 cm x 1 cm array of square 150  $\mu\text{m}$  posts with a 200  $\mu\text{m}$  pitch is made in SU-8 (SU-8 3050). The mold for the PDMS corralling mesh is also fabricated using standard photolithography techniques as described above. For thicker layers of SU-8, the resist formulations have much higher viscosities. Thus, the only modification to the technique is that a thin layer of low-viscosity SU-8 2002 is spun on to the bare wafer first, and then soft-baked. This layer of SU-8 makes the high viscosity SU-8 spread more evenly.

The array of posts is centered within a square ridge of  $\sim 1.5$   $\mu\text{m}$  in size and 100  $\mu\text{m}$  in width. The purpose of the square ridge is to firmly align a matching ridge (Figure 3-3d) on the top piece of the alignment jig so that the jig sits precisely centered around the post array. Because we were not sure of the fabrication tolerances of the rapid prototyping company, we made three sizes for the square ridge, one that was 99% of 1.5 cm along each side, one that was exactly 1.5 cm along each side, and one that was 101% of 1.5 cm along each side. We discovered that the ridge which was exactly 1.5 cm in size fit the matching ridge of the alignment perfectly, with no allowances for lateral movement once the piece was seated.

To create the mesh, 24  $\mu\text{L}$  of 10:1 PDMS is deposited onto the edge of the developed SU-8 mesh. PDMS wicks into the features by capillary forces to create a mesh with square through-holes that are 150  $\mu\text{m}$  x 150  $\mu\text{m}$ .

### *3.2.4 Cell Culture*

Adult rat hippocampal progenitor cells are originally isolated from the subgranular zone of the rat hippocampus. They are maintained in a cell culture incubator in DMEM/F-12 media (Gibco), supplemented with N2(Gibco) and 20 ng/mL FGF (Peprotech). Cells are kept in a

tissue culture incubator at 37°C and 5% CO<sub>2</sub>. Media is changed every 2 days. Cells are used at passage number 30-38.

Mixed differentiation media containing 1% fetal bovine serum (FBS) (Gibco) and 1  $\mu$ M retinoic acid (RA) (Enzo Life Sciences) and 1% penicillin/streptomycin is prepared fresh from stocks on each day it is used. RA is prepared in dimethyl sulfoxide (DMSO) to a stock concentration of 1 mM and stored frozen at 20°C in aliquots until use. FBS is also aliquoted and stored frozen at 20 °C until use.

### *3.2.5 Trap and Corral Experimental Procedure*

For all experiments, the polystyrene microwells must be coated with ECM to promote cell adhesion. First, the top surface of the embossed polystyrene microwells are blocked using 10 mg/mL BSA (Sigma) for 30 minutes at 37 °C. The BSA solution does not enter the microwells due to surface-tension mediated liquid pinning. Then the microwells are washed 3 times in PBS and a 10  $\mu$ g/mL laminin solution in PBS is added. The wells are then vacuumed for two minutes so that the laminin solution can fill the wells. The bubbles that remain on the surface are knocked off with gentle pipetting. Then the microwells are incubated in the cell culture incubator overnight.

For experiments without the corrals, the microwells are anchored to a 3.5 cm dish or 12 well plate using PDMS and UV-sterilized before coating. To count the capture efficiencies of the microwells, the cells are stained with Hoeschst in PBS for 10 minutes, and washed before imaging. Progenitor cells are dissociated from the dish by replacing the media with Accutase (Innovative Cell Tech.) at 37 °C for about 2-3 minutes and spun down at 1000 rpm for 2 minutes. They are then resuspended in media to a high density, passed through a 40- $\mu$ m nylon cell filter (BD Falcon) to ensure a single-cell suspension, and counted using a hemocytometer.

The cells are then seeded onto the microwells at a density of 300,000 cells/cm<sup>2</sup>. They are incubated for 10 minutes at 37 °C in the incubator and then triturated gently to disrupt cell adhesion to the top surface. This incubation/trituration sequence is repeated 2-3 times until the wells are filled and there is minimal cell adhesion to the top surface of the polystyrene. Then the cells are washed 5 times in PBS.

The top piece of the alignment jig is then placed face-down onto a sterile glass slide and plasma oxidized (Harrick Plasma) at high power (30W). This prevents the bottom surface of the PDMS from being made hydrophilic. The top piece is then snapped into the bottom piece using UV-sterilized plastic push-in fasteners (MicroPlastics). Then the PBS in the device is replaced with mixed differentiation media (1% FBS, 1  $\mu$ M retinoic acid, 1% penicillin/streptomycin prepared in DMEM/F12) and then taken to the imager. An overview of the experimental scheme using the alignment jig is shown in Figure 3-1e-f.

Some cells are seeded into PDMS meshes without the microwells. In these experiments, the PDMS meshes are conformally sealed to tissue culture polystyrene dishes and seeded with cells at low density.

### *3.2.6 Timelapse Microscopy*

The cells are imaged for up to two days on a Zeiss AxioObserver Z1 in a humidity, temperature, and CO<sub>2</sub>-controlled live imaging chamber. For microwell experiments without the corrals, the cells are imaged using 10X (35 μm spacing) or 5X objectives (90 μm spacing). The PlasDIC objective filter is used for enhanced contrast. Images are taken on a QImaging 5MPix Micropublisher camera every 10 minutes.

### *3.2.7 Data Processing*

Well occupancy data is tabulated by hand into a spreadsheet. In this analysis, we are primarily concerned with how well the initial contact state is maintained. When cells leave the well, the occupancy of the well is reduced by the number of cells that leave. When cells migrating along the top surface make contact with the cells in the microwell, the effective cell count in that well is reduced to 0, to reflect that the initial state has been disturbed. Cells migrating into empty wells do not increase the count for that well. This occupancy data is then parsed into residence times using a custom Matlab script implementing the aforementioned rubric (Appendix A-1).

### *3.2.8 Scanning Electron Microscopy*

The samples are fixed in 2% glutaraldehyde in 0.1M sodium cacodylate buffer at pH 7.2 for 1 hour and then rinsed 3 times for 15 minutes in the buffer. After post-fixing in 1% Osmium tetroxide for 1 hour, they are rinsed again 3 times in 0.1 M sodium cacodylate buffer. The samples are dehydrated in a succession of ethanol rinses (35%, 50%, 70%, 80%, 95%, 100%, 100%), each for 10 minutes. The samples are then dried in a critical point dryer and mounted onto stubs. Gold is sputtered onto the sample to a thickness of 35 nm and they are then scanned in a Hitachi S-5000.

### *3.2.9 Immunostaining*

In preparation for immunostaining, the cells are cultured in the corrals for 4 additional days after the imaging, with half-media changes every day. The cells are fixed in 4% paraformaldehyde in PBS at room temperature for 10 minutes. They are washed 3 times and then blocked with 5% donkey serum(Sigma) in tris-buffered saline (TBS) at pH 7.4, with 0.3% triton-x-100 (Sigma) for permeabilization. After blocking for one hour at room temperature on a shaker, the cells are then washed 3 times in the buffer and incubated overnight at 4 °C with primary antibody - chicken anti-GFAP (Abcam) – at 1:2000 dilution. The next day, the sample is washed 3 times and then incubated with secondary antibody – Dylight 488-donkey anti-chicken(Jackson Immuno) – for 1 hr at room temperature on a shaker. The samples are washed 3 times in TBS, with the last wash containing DAPI (diluted 1:500 from 5mg/mL stock). The sample is then mounted with a glass coverslip using Prolong Gold Antifade reagent (Invitrogen).

### **3.3. Results**

#### *3.3.1 Material Choice in Rapid Prototyping*

To make our alignment jig, we turned to rapid prototyping, an inexpensive way to produce precision manufactured 3D parts with a fast turn-around time (<1 week). Additive fabrication methods, which are more common, involves printing successive layers of precursor material that are then fused through the inkjet deposition of binding agents (3D printing), the rastering of high power lasers (selective laser sintering) or electron beams (electron beam melting). Stereolithography works similarly by incrementally lowering a platform into a vat of UV-curable resin. Each layer of the final object is cured by drawing a UV laser across the top. However, the materials available for additive fabrication technologies are usually proprietary polymers with relatively low glass transition temperatures (< 100 °C), high porosity and undetermined cytocompatibility

We found that the polymers which could be prototyped by stereolithography to the ~100 µm resolution we desired also had major deficiencies for our application. Namely, we specified our devices to be made from MicroFine Green and DSM Somos WaterShed XC 11122 by the rapid prototyping company FineLine Prototyping. We chose these materials for two reasons 1) DSM Somos WaterShed was stated to be biocompatible and 2) MicroFine Green had a resolution limit of 30-40 µm, well below our resolution limit of 100 µm. We found that DSM Somos showed poor cytocompatibility for NPCs. We also found that the MicroFine Green absorbed PDMS curing agent when PDMS was cast on the surface, thus inhibiting an essential part of our original process. Additionally, additive manufacturing suffers from a stair-stepping effect that is a result of the layer-by-layer construction, essentially invalidating its claims to <50 µm resolution.

By contrast, subtractive rapid prototyping, which removes material by computer programmed machine tools, does not suffer from this same problem. In subtractive rapid prototyping, a 3D design file is automatically translated into toolpaths that can be programmed into a computer numerical control (CNC) mill. For our second iteration, we chose to fabricate the jig (Figure 3-3) out of aluminum because it is heat resistant (which is useful for curing PDMS at high temperatures) and can be coated in a variety of metals and polymers.

Although pure aluminum oxide is highly corrosion resistant and supports the growth of cells<sup>23</sup>, the machining processes in rapid prototyping use aluminum alloys. These alloys have a high content of metallic impurities – iron, copper, manganese, chrome and zinc – which corrode and form salt precipitates in the cell culture media, which have high salt concentrations.

To address this problem, we coat the entire device in 10 µm of parylene by chemical vapor deposition. Parylene deposits in a highly conformal layer, is chemically inert and safe for cell culture. After deposition of parylene, no salt precipitation was observed when the jigs were incubated in cell culture medium for up to 5 days. Although this solution suited our needs, a

preferable, but more costly, approach would be to machine the device from a material known to be cytocompatible, such as Teflon or stainless steel.

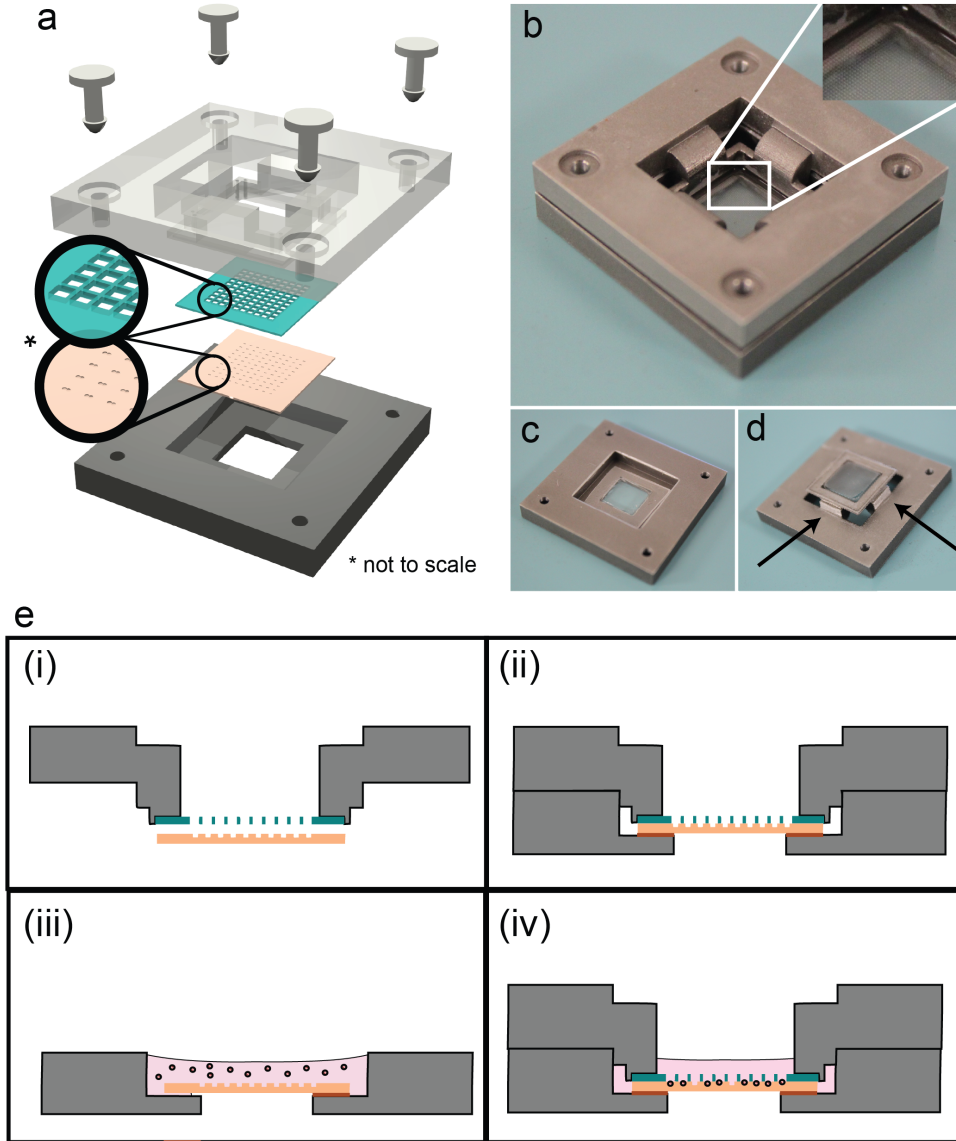


Figure 3-3 Trap and corral alignment jig. (a) In this 3D rendering, the top piece is displayed in a transparent material to show the layers below. A PDMS mesh is cured onto the bottom of the top piece (blue) and aligned onto a polystyrene substrate (pink), which has been affixed to the bottom of the jig. Plastic push-in fasteners are used to keep the assembly together. (b) Macro photographs of the assembled jig with a blowup of the mesh as the inset. (c) The bottom piece of the jig, with the polystyrene microwells affixed. (d) The top piece of the jig has a ridge (arrows) for aligning onto the SU-8 mold for the PDMS mesh. (e) To assemble the device, we (i) pre-align the mesh onto the microwell substrate, (ii) snap the top assembly into the bottom piece using PDMS adhesive between the microwell substrate and the bottom piece, (iii) cure the adhesive layer and remove the PDMS mesh before seeding cells, and (iv) corral with the pre-aligned mesh after seeding and washing.

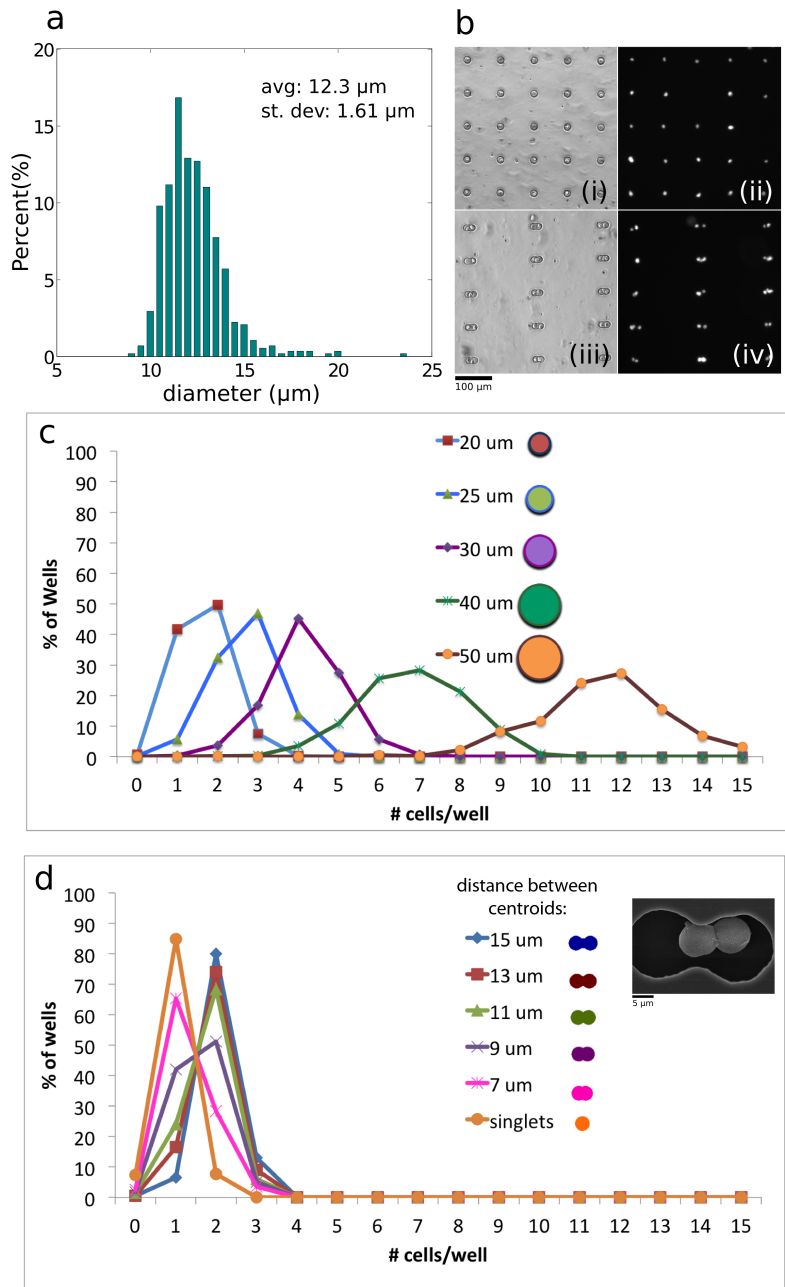


Figure 3-4 Microwells achieve high efficiencies in trapping single and paired cells. (a) The rat hippocampal progenitor cells are relatively uniform in size, averaging  $12.3 \pm 1.6 \mu\text{m}$ . (b) Rat hippocampal progenitor cells trapped in single cell wells (i-ii) or double cell wells (iii-iv). Phase images are on the left (i, iii) and Hoescht stained nuclei are shown on the right (ii, iv). (c) Varying the diameters of circular microwells tunes the average number of cells captured in each well but the distributions are broad. None of these well sizes are capable of capturing cell pairs with greater than 50% efficiency. (d) Round microwells (15  $\mu\text{m}$ ) can capture single cells with greater than 90% efficiency. Hourglass-shaped wells, which are essentially the union of two adjacent single-cell traps, can capture two cells with over 80% efficiency. The optimal separation between the centroids of the two halves was found to be 15  $\mu\text{m}$ .

### *3.3.2 Microwell Traps Achieve High Efficiency in Cell Pairing*

The adult hippocampal progenitor cells exhibit a tight distribution in their size ( $12.3 \pm 1.6 \mu\text{m}$ ) (Figure 3-4a). This size monodispersity enables us to capture single cells and paired cells with high efficiency. Phase and DAPI images of the Hoescht stained cells are shown in Figure 3-4b(i)-(iv). Over 90% of the  $15 \mu\text{m}$  microwells captures single cells (Figure 3-4d). Approximately 80% of the hourglass shaped microwell traps captured paired cells (Figure 3-4d).

The size of these microwells must be tightly tuned to the size of the cells of interest. Increases in the size of the round microwells results in increasingly broadening distributions in the number of cells captured (Figure 3-4). Additionally, adjusting the spacing between the centroids of the two circles comprising the halves of the microwell results in altered captured efficiencies. We find that a separation of  $15 \mu\text{m}$ , equal to the diameter of the single trap, results in the best trapping efficiencies for pairs of cells. For all further experiments, we used the  $15 \mu\text{m}$  diameter microwells for single cells and the hourglass traps with the  $15 \mu\text{m}$  spacing for paired cells.

An SEM scan is shown in the inset demonstrating cells trapped in proximity in the microwell making membrane contact. Some volumetric shrinking of the cells is observed due to the fixation and drying process used in the SEM preparation protocol.

### *3.3.3 Outward Migration in NPC Differentiation Medium*

After the cells are trapped into the microwells, the media is changed to one that results in mixed differentiation (1% FBS,  $1 \mu\text{M}$  retinoic acid, 1% penicillin/streptomycin) down all three lineages: neurons, astrocytes, and oligodendrocytes. In this medium, the cells begin to migrate outwards from the wells, and sometimes will crawl over and adhere to cells in neighboring wells (Figure 3-5a). This disrupts the isolated or contact state of single cells or paired cells respectively. Tracking of the residence times of cells in the microwells shows that the initial trapping state is fully maintained for about 420 minutes (for wells with  $90 \mu\text{m}$  spacings) (Figure 3-5b).

The pitch of the microwells affects the maintenance of the initial state. The further apart that the microwells are spaced, the slower the cells migrate outwards. (Figure 3-5c-d). For a  $35 \mu\text{m}$  spacing, the cells have a mean residence time of approximately 380 minutes, which increases to 1150 minutes for a spacing of  $90 \mu\text{m}$ . However, when cells are in hourglass traps separated by  $90 \mu\text{m}$ , they still migrate outwards quickly, with a residence time of 470 minutes (Figure 3-5d).

This outward migration demonstrates that microwells themselves are insufficient for constraining cell contact for the lengths of time necessary to see early markers of fate commitment, which usually peak at 1-2 days after the initial stimulus to differentiate. Although it is possible to fabricate deeper wells, cell viability is very low [data not shown].



Thus, our approach is to align additional corrals on top of the traps after the cells have been seeded.

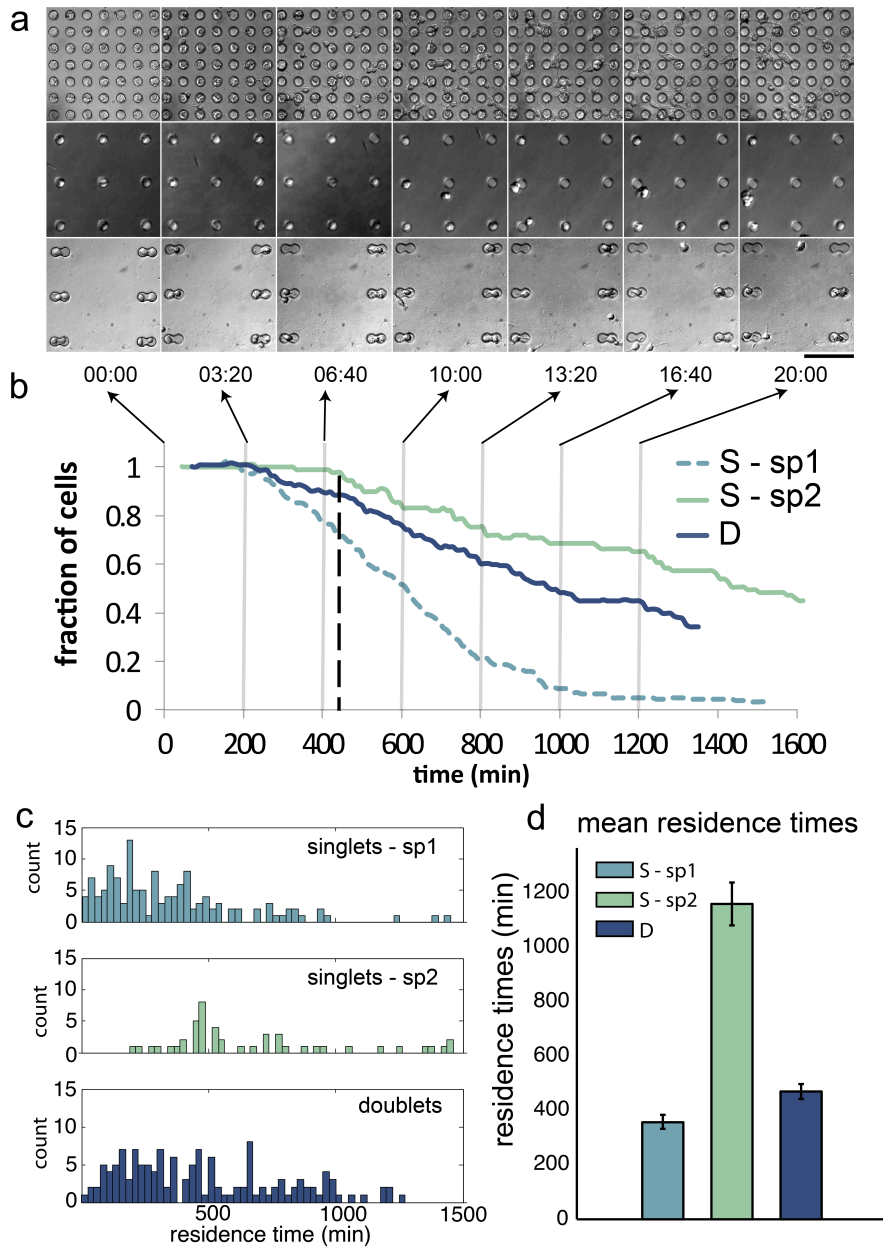


Figure 3-5 Outward migration from microwells in mixed differentiation media. (a) Timelapse data of cells trapped in single microwells with spacings of 35  $\mu\text{m}$  (top) and 90  $\mu\text{m}$  (middle) or hourglass microwells (bottom). (b) The maintenance of the initial separation or contact state decays over time. Single microwells with 90  $\mu\text{m}$  retain the trapping state for the longest time, until approximately 420 minutes after the mixed differentiation media is added. (c) Histogram of the residence times in each of the microwell conditions. (d) The mean residence times of cells in microwells is increased by over 800 minutes when the center-to-center spacing is increased from 35  $\mu\text{m}$  to 90  $\mu\text{m}$ . However, traps with more cells show more outward migration. The differences in distribution are significant by the Kolmogorov-Smirnov test (\*\*,  $p < 10^{-9}$ , \*,  $p < 0.005$ ). Error bars show  $\pm$  SEM. Scale bar: 100  $\mu\text{m}$ .

### 3.3.4 Fabrication of PDMS Mesh With Through-Holes

We made thin PDMS layers with  $150\ \mu\text{m} \times 150\ \mu\text{m}$  through-holes to serve as a physical corral to microwell-trapped neural progenitor cells. To accomplish this, we took advantage of capillary action to wick PDMS into the channels between an array of  $150\ \mu\text{m} \times 150\ \mu\text{m}$  square posts on an SU-8 mold (Figure 2-6). Although the SU-8 features are fabricated to a height of  $120\ \mu\text{m}$ , the thickness of the resulting PDMS film is measured to be  $85\text{-}95\ \mu\text{m}$ . The spread of PDMS is fairly fast, filling a  $4 \times 8$  array of nodes (Figure 2-6b) in a little over 1 minute. A blow-up of one of the edges (Figure 2-6c) shows that the flow can be turbulent (panel 3 at 32s). Because the Reynolds number of PDMS flow through an ideal open channel of our dimensions is very small ( $2 \times 10^{-6}$ ), we believe this turbulence to be the result of a combination of capillary action, gravity-driven flow (due to the high volume of the PDMS ring at the edge), and surface roughness in the SU-8 layer.

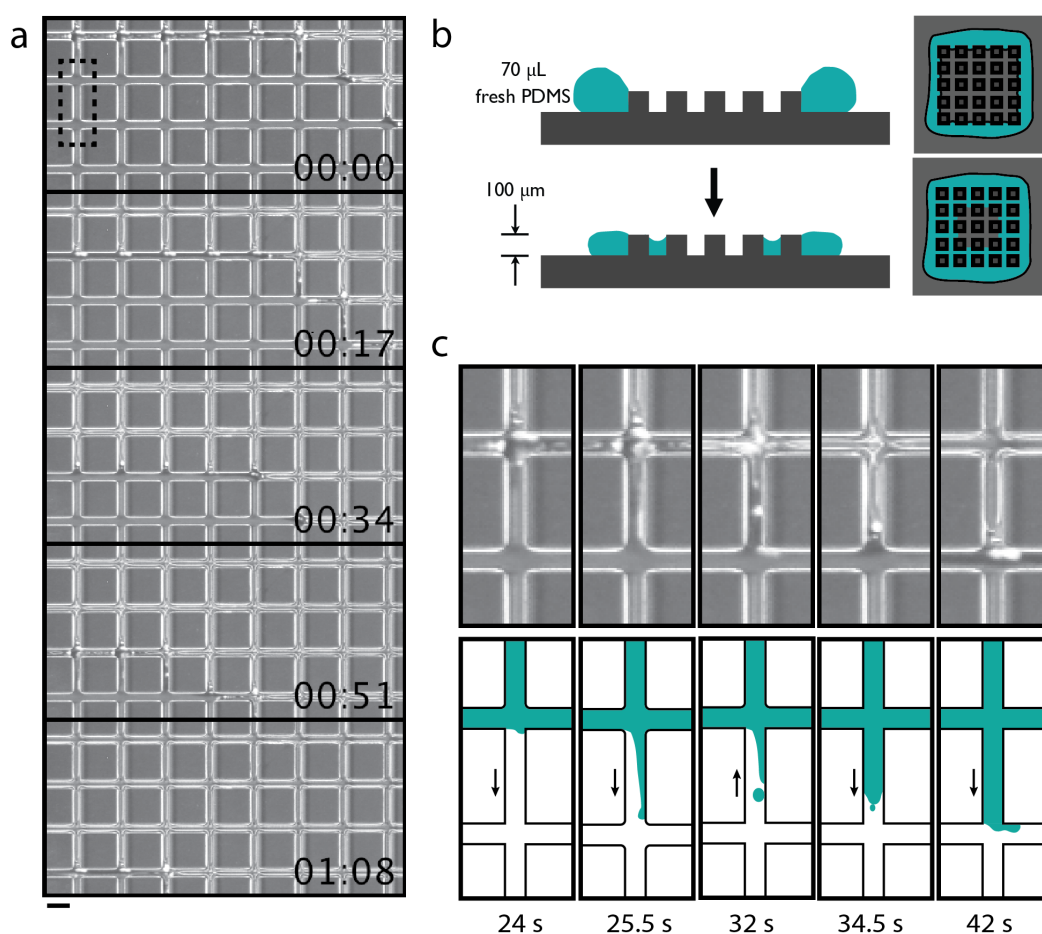


Figure 3-6 PDMS mesh fabrication. (a) A time-series shows that a  $4 \times 8$  array of nodes is filled from the top right (where the nearest corner is) in about 1:08. (b) Immediately after mixing, PDMS is pipetted along the edge of an SU-8 mold with  $150 \times 150 \times 100\ \mu\text{m}$  square posts. Capillary action causes the PDMS to wick through the channels between posts, filling the entire  $1\text{cm} \times 1\text{cm}$  array within 5-10 minutes. Cartoon is not to scale. (c) The area within the dotted line in (a) is blown up and shows that flow through the channels is turbulent (third frame at 34s shows retraction of fluid boundary).

Once the PDMS has spread throughout the entire area, we place the upper piece of the alignment jig within the alignment square and allowed the entire assembly to cure at room temperature overnight. Slower rates of polymerization result in higher PDMS elasticity, which is beneficial for our application because the PDMS mesh must deform approximately 1 cm in the z-axis during the removal process. After curing, slow, careful removal of the alignment piece from one corner could peel the PDMS mesh away from the mold, while keeping it attached to the aluminum alignment piece.

We found that the application of uncured PDMS to the SU-8 mold must take place immediately after mixing the base prepolymer and curing agent. In our experience, at room temperature, changes to the viscosity of PDMS were appreciable within minutes. If we applied the PDMS 5-10 minutes post-mixing to the mold, capillary action would not be sufficient to fill the grid channels within the 1cm x 1cm mold area. We also discovered a biphasic relationship between surface modifications by trichloroperfluorosilane and capillary filling. Although the mold needed to be rendered hydrophilic by trichloroperfluorosilane in order for capillary filling to take place, overnight deposition of silane under vacuum proved to be too long and the mold would not fill completely. We found 30 minutes of silanization under house vacuum to be an adequate length of time.

In general, the fabrication of PDMS layers with through-holes is extremely useful for 3D microfluidic applications. Precisely aligned holes can form interconnects between multiple layers of microfluidic channels, enabling high-throughput microfluidic applications that would be difficult to assemble in one plane. The low-throughput method to producing holes is to manually punch holes in a PDMS layer using a thin metal tube.

Another method that has been widely reported on in the literature is high-speed spinning of PDMS on molds to achieve thin films. However, the problem with high-speed spinning is that sometimes PDMS will coat the top surface of the mold posts, generating a residual thin membrane occluding the through-hole<sup>24</sup>. Some have tried to alleviate this effect by air-blowing<sup>25</sup> or high-pressure squeezing of the residual PDMS using an intermediate adhesive layer<sup>26</sup>, but these methods are unnecessary given the natural tendency of PDMS to flow around tall SU-8 posts as a result of surface tension. A recently published paper uses manual removal of SU-8 posts after spinning to eliminate the residual membrane problem, but the extreme drawback of this method is that the SU-8 mold can only be used once. Other published methods for forming through-holes in PDMS membranes using mechanical tearing<sup>27</sup>, gas plasmas for surface treating PDMS<sup>28</sup>, and SF<sub>6</sub>/O<sub>2</sub> reactive ion etching of PDMS itself<sup>29</sup> can cause damage to the integrity of the device, create unwanted debris, or involve chemical processing steps that are not necessary.

Although our purpose for our technique is to create a regular array of through holes in a thin PDMS membrane, we believe it may be possible to adapt this technique to non-grid formations of through-holes by using lower viscosity PDMS (diluted in a solvent such as toluene) or low-speed spinning of small amounts of liquid PDMS placed at strategic locations relative to the through-hole features. Low-speed spinning can facilitate the spread of the thin rim of PDMS (made possible by surface treating silicon to be hydrophilic) to the mold

features so that surface tension can take over. This facilitated spreading also speeds the process before enough polymerization has taken place such that the viscosity of the uncured polymer has increased appreciably. One thing to keep in mind is that the top surface of the PDMS membrane near the SU-8 is not flat because of surface tension effects. Thus, this method will only be useful for producing through-holes that are smaller in cross-sectional area than the channels that are being connected, so that bonding can occur away from the hole where the surface is not flat. Despite this small limitation, to our knowledge, this is the simplest method for making thin PDMS films with through-holes and the development of this technique may be very useful for the microfluidics field at large.

### *3.3.5 PDMS Sealing Under Liquids*

PDMS is a very hydrophobic material that forms a reversible conformal seal to a variety of materials by van der Waals forces. This conformal seal can resist up to 30 kPa of pressure and can be used for low-pressure microfluidics applications<sup>30</sup>. However, when immersed in liquid, PDMS is subject to a buoyant force due to the lower density of PDMS (0.965 g/mL) versus the surrounding liquid medium (usually slightly higher than 1.0 g/mL, the density of water).

For thicker pieces, this buoyant force can be large enough to lift the piece up away from the surface to which it has been sealed. However, for thin films of PDMS (such as the mesh in these experiments), the buoyant force is small enough to be insignificant. Thus, for the 85  $\mu\text{m}$  thick PDMS meshes, the seal remains undisturbed in cell culture medium for at least 7 days.

Due to the small dimension of the holes in the mesh and the hydrophobicity of PDMS, air bubbles get trapped in the meshes when they are immersed in aqueous solutions. To alleviate this problem, we make the PDMS surface hydrophilic by exposing it to oxygen plasma at 30W of RF power for 2 minutes (Harrick Plasma, PDC-32G). However we have found that hydrophilic PDMS does not seal well with the polystyrene surface under water. We suggest that the failure to form a seal is a result of water molecules forming a lubricating layer that prevents the PDMS from making contact with the polystyrene surface. To protect the bottom surface of PDMS from being oxidized, we press the mesh to a clean glass slide during plasma oxidation, leaving that surface hydrophobic.

Meshes that have a hydrophilic top and sides are able to wet thoroughly and also seal to a polystyrene surface in water. However, no seal can be achieved in cell culture media due to undetermined interactions with the molecular constituents of cell culture media. We found that phosphate buffered saline, an isotonic salt solution suitable for cells, does not present the same problem. Thus our protocol calls for replacing the media with PBS before aligning the mesh on top of the seeded cells.

### *3.3.6 Trap and Corral*

Timelapse imaging of the cells that have been trapped and corralled indicate that they maintain contact for up to a day after seeding (Figure 3-7b). Low-density seeding of the PDMS corrals alone can result in two cells being trapped in each well, but in those conditions,

the two cells often engage in very little contact or none at all (Figure 3-7a). We show that the cells can be cultured for up to six days, enough time for cells to start expressing markers of differentiation (Figure 3-8).

Occasionally, we observe that cells will migrate vertically up the walls of the corrals and migrate along the top surface of the mesh. Though many remain on the top surface of the PDMS mesh, some will descend into the same or a different corral. Since we use time-lapse microscopy to monitor cell migration, we exclude any cases where this happens. We anticipate that this problem can be easily avoided by blocking the surface of the top and sides of the PDMS mesh using PLL-PEG, a cytophobic surface coating.

Since the PDMS meshes are only  $\sim 100 \mu\text{m}$  thick, they can deform when brought down on top of the underlying substrate. Two features of the device design prevent them from deforming significantly. The first is that the entire mesh remains attached to the top part of the alignment jig as it is peeled away from the mold (Figure 1d). Thus the top part of the jig maintains the mesh in a stretched, flat state so that it is easy to handle. The other feature is that the sides of the top part (arrows in Figure 3-3d) fit snugly against the sidewalls in the recession of the bottom part. This restricts the motion of the top piece vertically so that there is no lateral deformation of the mesh as it is brought down. When the meshes are positioned by hand (such as when they are sealed to unembossed polystyrene), deformation can be prevented by bringing the mesh down gently, allowing one side to seal against the substrate before slowly lowering the other side.

This corral alignment method is adaptable to many types of patterned substrates. Since the corrals are aligned on top of the substrate after the cells have been seeded, any substrate to which PDMS can conformally seal in aqueous solutions can be used. Conformal sealing is necessary to prevent cells and processes from burrowing through to adjacent chambers. In this paper, we track homotypic interactions between cells, but the technique can easily be extended to heterotypic cell interactions to repertoire of signals that a stem cell may receive *in vivo*. For example, *in situ* addressable photopatterning<sup>13</sup> can be used to create heterotypic multicellular assemblies, which may then be cultured in isolation for extended periods of time using this architecture.

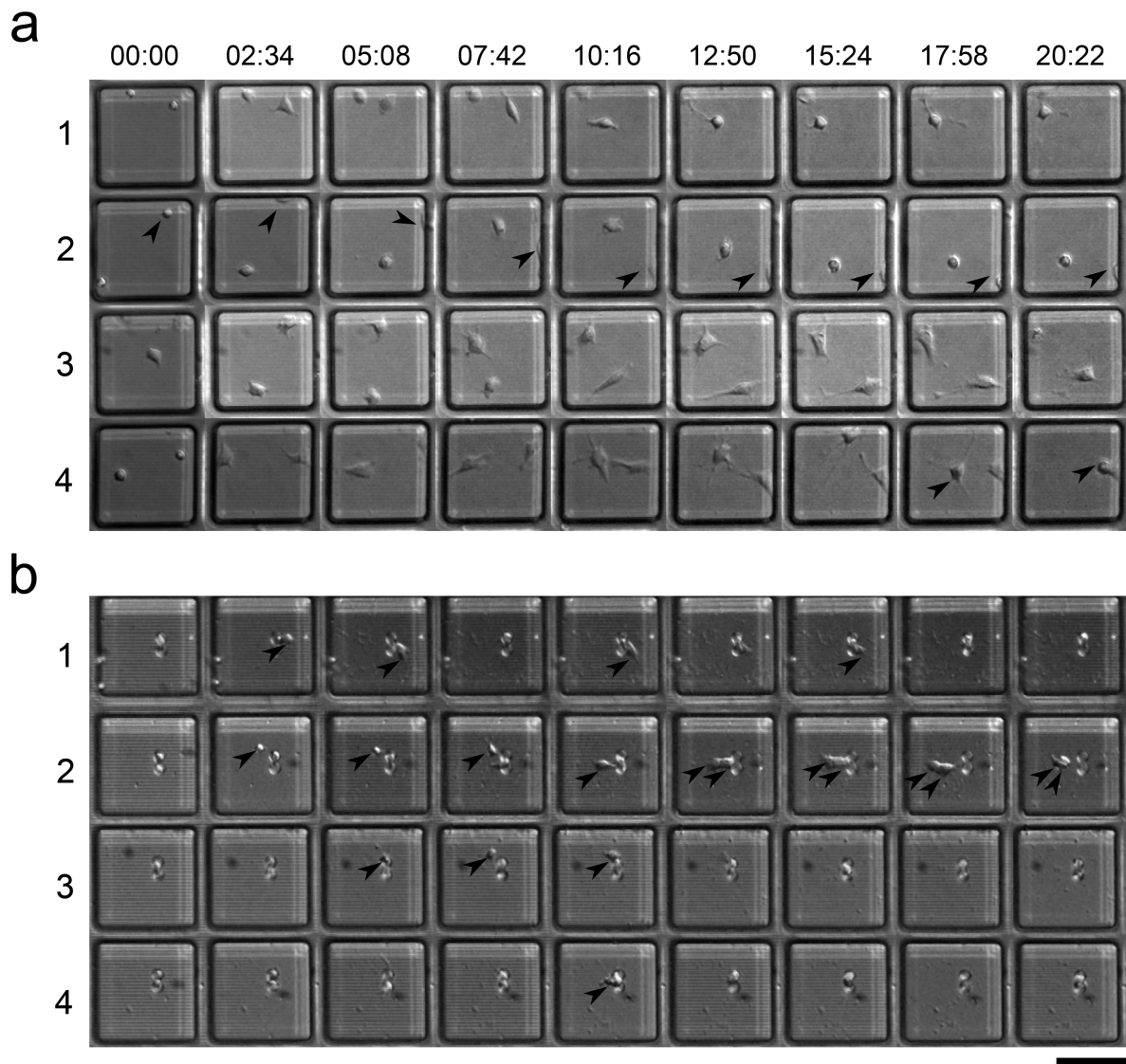


Figure 3-7 Migration of cell pairs when seeded into corrals (a) or trapped in microwells first and then corralled (b). Cells that are randomly seeded into corrals rarely make contact over a 24 hour period but cells which have been pre-trapped maintain the contact state. In (a), arrows show the position of cells that are difficult to decipher from still images. In (b) arrows are added to show the position of cells which have crawled out of the microwells. Though the cells often try to migrate away, they often bounce back (1,3,4) or both cells migrate out together (2).

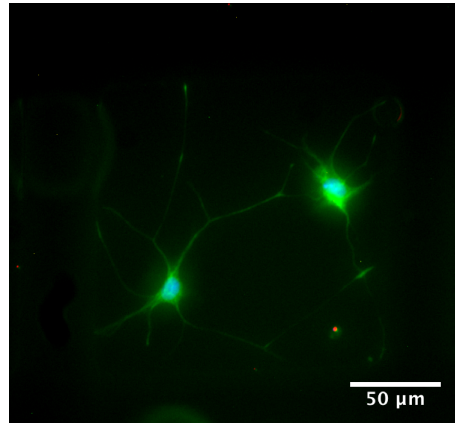


Figure 3-8 Immunostained cells in corrals. GFAP, an astrocytic marker, is in green and DAPI is in blue.

### ***3.4 Conclusions***

The technology presented here possesses two important features. First of all, the cells can be trapped as single cells or cell pairs with high efficiency. This efficiency can be easily extended to trapping higher numbers of cells by modifying the spatial geometries of the traps. Secondly, cells can continue to be cultured for many days after trapping, without significant change to the initial contact or separation state. Although sometimes paired cells will separate, the cells are generally observed to maintain their contact state for up to a day. Additionally, they will not migrate into neighboring wells because the PDMS mesh acts as a contact barrier. Although it is possible to seed one or two cells randomly into the corrals, the cells often never make contact over a 1-day period because they are likely to be seeded far apart.

The conjunction of these two features – high efficiency, and long-term maintenance of the initial state – means that the technology can be used to dissect the downstream effects of contact-mediated signaling days after the cell-cell contact was initially specified. This is crucial because markers of these initial differentiation decisions often take from 1 to 6 days to become detectable. For these hippocampal progenitor cells, immunochemical staining cannot detect fate commitment until >4 days after fate induction by chemical inducers. The known markers, such as glial fibrillary acidic protein and beta-tubulin III, are cytoskeletal proteins that take many days to be expressed to adequate levels.

Alternatively, the detection of mRNA levels, either by mRNA microarray screens or qPCR, can be used earlier (at about 1-2 days) to detect changes in the expression levels of transcription factors that are markers of fate commitment. These mRNA detection methods generally require a substantial amount of starting material, the equivalent of approximately  $10^3 - 10^6$  cells. Thus, the high efficiency of cell pairing in our method enables us to use mRNA detection techniques to probe the early transcriptional changes that occur as a result of cell-contact mediated signaling processes.

### 3.5 References

- 1 Gage, F. H. Mammalian Neural Stem Cells. *Science* **287**, 1433-1438,(2000).
- 2 Conover, J. C. *et al.* Disruption of Eph/ephrin signaling affects migration and proliferation in the adult subventricular zone. *Nature neuroscience* **3**, 1091-1097,(2000).
- 3 Kullander, K. & Klein, R. Mechanisms and functions of Eph and ephrin signalling. *Nature reviews. Molecular cell biology* **3**, 475-486,(2002).
- 4 Tavazoie, M. *et al.* A specialized vascular niche for adult neural stem cells. *Cell stem cell* **3**, 279-288,(2008).
- 5 Gartner, Z. J. & Bertozzi, C. R. Programmed assembly of 3-dimensional microtissues with defined cellular connectivity. *Proceedings of the National Academy of Sciences of the United States of America* **106**, 4606-4610,(2009).
- 6 Chen, C. S., Mrksich, M., Huang, S., Whitesides, G. M. & Ingber, D. E. Micropatterned surfaces for control of cell shape, position, and function. *Biotechnology progress* **14**, 356-363,(1998).
- 7 Nelson, C. M. & Chen, C. S. Cell-cell signaling by direct contact increases cell proliferation via a PI3K-dependent signal. *FEBS Letters* **514**, 238-242,(2002).
- 8 Tang, J., Peng, R. & Ding, J. The regulation of stem cell differentiation by cell-cell contact on micropatterned material surfaces. *Biomaterials* **31**, 2470-2476,(2010).
- 9 Letourneau, P. C. Cell-to-substratum adhesion and guidance of axonal elongation. *Developmental biology* **44**, 92-101,(1975).
- 10 Thissen, H. *et al.* Nanometer thickness laser ablation for spatial control of cell attachment. *Smart Materials and Structures* **11**, 792-799,(2002).
- 11 Piner, R. D. "Dip-Pen" Nanolithography. *Science* **283**, 661-663,(1999).
- 12 Roth, E. a. *et al.* Inkjet printing for high-throughput cell patterning. *Biomaterials* **25**, 3707-3715,(2004).
- 13 Kim, M. *et al.* Addressable micropatterning of multiple proteins and cells by microscope projection photolithography based on a protein friendly photoresist. *Langmuir* **26**, 12112-12118,(2010).
- 14 Thomas, C. H., Lhoest, J. B., Castner, D. G., McFarland, C. D. & Healy, K. E. Surfaces designed to control the projected area and shape of individual cells. *Journal of biomechanical engineering* **121**, 40-48,(1999).
- 15 Folch, A. & Toner, M. Microengineering of cellular interactions. *Annual review of biomedical engineering* **2**, 227-256,(2000).
- 16 Parekkadan, B. *et al.* Cell-cell interaction modulates neuroectodermal specification of embryonic stem cells. *Neuroscience* **438**, 190-195,(2008).
- 17 Di Carlo, D., Wu, L. Y. & Lee, L. P. Dynamic single cell culture array. *Lab on a chip* **6**, 1445-1449,(2006).
- 18 Skelley, A. M., Suh, H., Voldman, J., Kirak, O. & Jaenisch, R. Microfluidic control of cell pairing and fusion. *Nature methods* **6**, 147-152,(2009).
- 19 Nelson, C. M., Raghavan, S., Tan, J. L. & Chen, C. S. Degradation of Micropatterned Surfaces by Cell-Dependent and -Independent Processes. *Langmuir* **19**, 1493-1499,(2003).
- 20 Dusseiller, M. R., Schlaepfer, D., Koch, M., Kroschewski, R. & Textor, M. An



- inverted microcontact printing method on topographically structured polystyrene chips for arrayed micro-3-D culturing of single cells. *Biomaterials* **26**, 5917-5925,(2005).
- 21 Sharp, J. & Forrest, J. Free Surfaces Cause Reductions in the Glass Transition Temperature of Thin Polystyrene Films. *Physical Review Letters* **91**, 1-4,(2003).
- 22 Rieger, J. The Glass Transition Temperature of Polystyrene: Results of a round robin test. *Journal Of Thermal Analysis* **46**, 965-972,(1996).
- 23 Hoess, a., Teuscher, N., Thormann, a., Aurich, H. & Heilmann, a. Cultivation of hepatoma cell line HepG2 on nanoporous aluminum oxide membranes. *Acta biomaterialia* **3**, 43-50,(2007).
- 24 Kartalov, E. P., Walker, C., Taylor, C. R., Anderson, W. F. & Scherer, A. Microfluidic vias enable nested bioarrays and autoregulatory devices in Newtonian fluids. *Proceedings of the National Academy of Sciences* **103**, 12280-12284,(2006).
- 25 Joo, H. K., Eujin, U. & Je-Kyun, P. Fabrication of a poly(dimethylsiloxane) membrane with well-defined through-holes for three-dimensional microfluidic networks. *Journal of Micromechanics and Microengineering* **19**, 045027,(2009).
- 26 Folch, A., Jo, B. H., Hurtado, O., Beebe, D. J. & Toner, M. Microfabricated elastomeric stencils for micropatterning cell cultures. *J Biomed Mater Res* **52**, 346-353,(2000).
- 27 Mosadegh, B., Agarwal, M., Torisawa, Y. S. & Takayama, S. Simultaneous fabrication of PDMS through-holes for three-dimensional microfluidic applications. *Lab Chip* **10**, 1983-1986,(2010).
- 28 Jongchan, C., Kyeong-Hwan, L., Choi, J. A., Sun Hwa, L. & Sung, Y. in *Micro Electro Mechanical Systems (MEMS), 2011 IEEE 24th International Conference on*. 304-307.
- 29 Chen, W., Lam, R. H. W. & Fu, J. Photolithographic surface micromachining of polydimethylsiloxane (PDMS). *Lab on a chip* **12**, 391-395,(2012).
- 30 Kuncová-Kallio, J. & Kallio, P. J. PDMS and its suitability for analytical microfluidic devices. *Proceedings of the 28th IEEE EMBS Annual International Conference* **1**, 2486-2489,(2006).

## Chapter 4: Micropatterning Persistent Interactions Between Neural Progenitor Cells Reveals Single Cell Influences On Cell Fate

---

### 4.1 Introduction

Adult neural stem cells found in the hippocampus have the capacity to regenerate new neurons and glia throughout life<sup>1,2</sup>, playing a critical role in learning and memory<sup>3,4</sup>. They are found embedded in the subgranular zone of the dentate gyrus where they are mostly quiescent and occasionally divide asymmetrically to form astrocytes and neuronal precursors<sup>5</sup> at roughly equal propensities. How and when these cells decide to differentiate depends largely on the the environment around them.

Through immunostaining, EM studies<sup>6</sup>, and fate tracing, this microenvironment is known to be composed mostly of other progenitor and stem cells, granule neurons, non-pluripotent astrocytes and blood vessel components<sup>7,8</sup>. *In vivo* and *in vitro* studies have shown that these niche components play important but complex roles in regulating stem cell fate. For instance, non-radial glia astrocytes have been shown to induce neuronal cell fates through the Wnt3a pathway<sup>9</sup> and the Eph-ephrin pathway<sup>10</sup> and neurons have been shown to induce oligogenesis<sup>11</sup>. Sonic Hedgehog<sup>12</sup> and Notch signaling<sup>13,14</sup> have also been shown to maintain pluripotency and regulate proliferation in uncommitted stem and progenitor cells. In the face of so many different cues, of which some may be contradictory, how does a cell make a concerted choice to differentiate down one of many lineages, remain quiescent, or self-renew? Do single neighbors possess the capacity to significantly bias cell fate?

In this work, we aim to study how single neighboring cells can affect stem cell differentiation *in vitro* using micropatterns to enforce persistent interactions between cells on the same pattern. Since seeding on these surfaces is random, we can correlate initial cell number with final cell fate by imaging the cells in brightfield every day using a high-throughput imager. Analysis of the brightfield images reveal that the initial cell state is maintained until day 2 by approximately 50-75% of all patterns before the cell division occurs.

Based on the previous findings that astrocytes induce neurogenesis and neurons induce oligogenesis, we anticipated that neural progenitor cells cultured in pairs may induce the opposite fate in their neighbors. Surprisingly, we discovered that paired NPCs exhibit a lower percentage of fate asymmetry in their progeny than expected. We also found that the initial number of neural progenitor cells does not affect the overall distribution of Tuj1+ neurons or GFAP+ astrocytes, indicating that the reduced fate asymmetry is not the result of the preference of paired cells for specific fate outcomes. To the best of our knowledge this is the first time single cells have been shown to exert significant biases on stem cell fate decisions in a medium that promotes multilineage differentiation. It remains to be shown whether the observed fate symmetry is the consequence of one cell repressing the differentiation of its neighbor or inducing the same fate.

## **4.2. Materials and Methods**

### **4.2.1 Cell Culture**

Progenitor cells can be isolated from dissociated hippocampal tissue and propagated in FGF-2, resulting in cell cultures that are tripotent for astrocytes, neurons, and oligodendrocytes given the right media conditions. Since the progenitors are GFAP-, nestin+, and Sox2+, they are assumed to exist on a spectrum between type II transit-amplifying progenitors, which have only been observed *in vivo* to differentiate into neurons<sup>5,15</sup>, and GFAP+ radial glia, which can generate all three subtypes.

The cells are maintained in a cell culture incubator in DMEM/F-12 media (Gibco), supplemented with N2(Gibco) and 20 ng/mL bFGF (Peprotech). Cells are kept in a tissue culture incubator at 37°C and 5% CO<sub>2</sub> and maintained without the use of antibiotics to prevent the introduction of latent infections. Media is changed every two days and cells are used for experiments at between passage number 32 and 37. Only cultures with phase-bright round cells that have few and short processes are used.

Hippocampal astrocytes are isolated from the adult rat hippocampus. They are grown on poly-ornithine/laminin coated plates in a cell culture incubator in DMEM/F-12 media (Gibco), supplemented with 1% N-2(Gibco), 10% FBS, and 0.5% penicillin/streptomycin.

Mixed differentiation media with 50% conditioned media, 1% fetal bovine serum (FBS) (Gibco) and 1 uM retinoic acid (RA) (Enzo Life Sciences) and 1% penicillin/streptomycin is prepared fresh from frozen stocks on each day it is used. RA is prepared in dimethyl sulfoxide (DMSO) to a stock concentration of 1 mM and stored frozen at 20°C in aliquots until use.

FBS is also aliquoted and stored frozen at 20°C until use. Conditioned media is collected from NPCs grown on 10 cm dishes at 2 days after FGF addition or passage and frozen at -20°C until use. Since cells are seeded at a low effective cell density on the micropatterned substrates, the cytokines from conditioned media (such as glycosylated Cystatin C<sup>16</sup>) are necessary for maintaining survival.

#### *4.2.2 Imaging*

Automated imaging is performed on a MDS ImageXpress High-Throughput Imager using the 10X objective and DAPI, FITC, and Cy3 filters. Brightfield imaging is performed on the Cy3 filter using a Fiber-Lite (Model 3100, Dolan-Jenner) inserted through the drug delivery port, supported in the upright position by a truncated copper pipe.

To find the overlap parameters to assure nearly perfect stitching between images, we performed calibration tests using a sample slide with fixed cells. A column overlap of 3 μm and a row overlap of 2 μm for the 10x objective produces images that has nearly no overlap error when pieced together.

For each day of the experiment, all micropatterned areas of plates were imaged in brightfield at 10x with the sample heater at 37°C. Since imaging of each plate took less than 1 hour and the media is HEPES-buffered, CO<sub>2</sub> incubation was not necessary. After imaging, cells were washed and the medium was replaced.

#### *4.2.3 Micropatterning*

Using microcontact printing of proteins onto polystyrene, we create 140 μm x 140 μm adhesive islands to constrain cell-cell interactions over the course of a 6-day differentiation period. PDMS posts used for microstamping poly-ornithine onto polystyrene substrates are made using standard soft lithography protocols. Briefly, an SU-8 mold is made by spinning SU-8 2015 to a thickness of 10 μm on a silicon test wafer using a Headway spinner. The wafer is then soft-baked and exposed on a Karl Suss MA6 Mask Aligner. After post-baking the wafer is developed in SU-8 developer and washed with IPA and water. The wafer is hard-baked at 150°C for 10-30 minutes to anneal thermal cracks and to improve adhesion to the substrate. The wafer is then coated with trichloro(1H,1H,2H,2H-perfluorooctyl)silane (Sigma) by vapor deposition under a vacuum-trapped house vacuum line for 1 hour. SU-8 is mixed at a 10:1 ratio of prepolymer to curing agent, poured onto the molds, and degassed until all bubbles at the features have risen to the top. The polymer is then allowed to cure on the benchtop overnight. The first mold after silanization is discarded.

PDMS stamps are then cut to size, washed briefly with IPA and distilled water, and then oxidized using an air plasma in a Harrick Plasma Cleaner (PDC-32G) for 1 minute to generate hydrophilic Si-OH groups at the surface. They are then quickly brought to the tissue culture hood, where they are sterilized under the germicidal UV lamp in the tissue culture hood for 5 minutes. Since uncrosslinked polymers within the PDMS stamp slowly repopulate the surface

rendering it hydrophobic again, it is imperative to ink the stamp within approximately 10-20 minutes of plasma oxidation.

The stamps are inked in a 50 ug/mL poly-ornithine solution diluted in PBS for 30 minutes (Figure 4-1a). The solution is aspirated and the surface of the stamp is then washed 2x in PBS and allowed to dry in the hood. Care must be taken to remove as much of the PBS as possible to prevent salt crystals from forming in the interstitial spaces between the PDMS posts.

The stamps are then inverted into the middle of each well in a 6-well plate (BD Falcon) using a template to ensure centered placement. Using flat-tipped tweezers, the stamps are gently pressed to ensure good transfer of poly-ornithine to the underlying polystyrene substrate. After allowing the stamps to sit for at least 1-2 minutes, they are removed in one stroke to prevent smearing. Approximately 80 uL of 0.1 mg/mL poly-l-lysine graft PEG (Susos AG Int, Germany) in 10 mM HEPES buffer (with 150 mM NaCl) is then pipetted in the center of the stamped region (Figure 4-1b), and allowed to incubate for 45 minutes at room temperature. The patterns are then washed 2x in HEPES buffer and once in PBS. Laminin solution (Gibco) at 10 ug/mL is then added to each well and allowed to incubate at 37°C overnight.

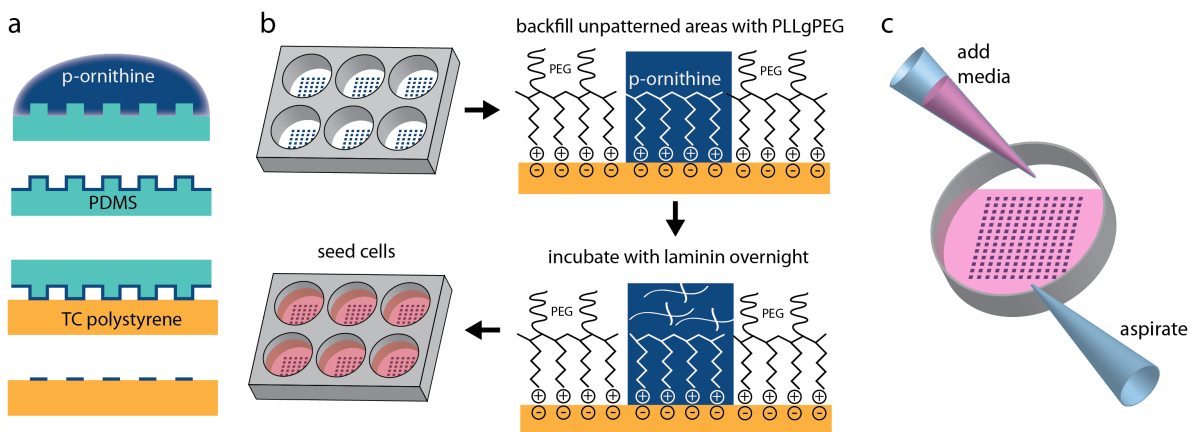


Figure 4-1 Micropatterns are generated by inking microstamps with poly-ornithine and stamping the polystyrene substrate in a 6-well plate (a). Unpatterned areas are blocked with PLL-graft-PEG which forms a protein-resistant brush-layer. Overnight incubation with laminin coats the poly-ornithine patterned areas, rendering the area adhesive to cells (b). To wash cells after seeding, old media must be aspirated at the same time as the addition of new media to create a continuous flow(c).

#### 4.2.4 Cell Seeding on Micropatterns

Neural progenitor cells and hippocampal progenitor cells are seeded onto micropatterned substrates at a cell density of 2000 cells/cm<sup>2</sup> and 1000 cells/cm<sup>2</sup> respectively in mixed differentiation medium. NPCs and hippocampal astrocytes are detached using Accutase (Innovative Cell Tech) and 0.25% Trypsin/EDTA (Gibco) respectively. They are allowed to attach for 12 hours without disturbance in the incubator.

After 12 hours, excess unattached cells are washed very carefully in the following manner: the plate is propped up on a folded paper towel to an angle of approximately 5-10°. At the same

time, add 1 mL of medium at the top of the well and aspirate medium from the bottom but stopping before all of the medium is added from above. At no point should the well be allowed to dry because the PEG coating is prone to dewetting, which delaminates the patterned cells and proteins<sup>17</sup>. At this point all medium used to wash and feed cells is composed of 50% conditioned medium, 1% FBS, 1uM retinoic acid, and 1% pen/strep.

As a control, we also seeded NPCs at varying densities and stoichiometric ratios to mimic the mixing ratios observed from the micropatterns. NPCs are seeded at 2000, 4000, and 8000 cells/cm<sup>2</sup>, resulting in approximately 2, 4, and 8 cells / 100 um<sup>2</sup>. For all conditions containing astrocytes, astrocytes are seeded at 1 cell/100 um<sup>2</sup>. Thus increasing NPC density decreases the astrocyte:NPC ratio. All micropatterned and control condition are run in triplicate.

For each day of the experiment, all micropatterned areas of plates were imaged in brightfield at 10x with the sample heater at 37°C. Since imaging of each plate took less than 1 hour and the media is HEPES-buffered, CO<sub>2</sub> incubation was not necessary. After imaging, the media was replaced.

#### *4.2.5 Immunostaining*

Cells were fixed and immunostained 6 days post-seeding using the following antibodies: mouse anti-Tuj1 at 1:1000 (Sigma), rabbit anti-GFAP at 1:1000 (Abcam) donkey anti-mouse-Alexa 488 at 1:250 (Jackson), donkey anti-rabbit-Cy3 at 1:250 (Jackson). DAPI was used at 1:1000 dilution. Blocking buffer containing 5% donkey serum (Sigma) and 2% BSA in tris-buffered saline (pH 7.4) was used to pre-block the samples and during the primary incubation step. Primary incubation was carried out at room temperature for 1 hour on a Belly Button rocker (Denville Sci. Inc) and overnight at 4C with no rocking. Secondary incubation was performed at room temperature for one hour on the rocker. Cells were washed and stored in PBS until imaging (Figure 2).

#### *4.2.6 Automated and Manual Image Processing*

After image acquisition, we constructed aligned montages of each micropatterned well using MetaXpress. A regular grid corresponding to the pitch of each pattern was then aligned onto the montaged image and stacks were generated from these grids using the MetaXpress “MeasureGrid” function in conjunction with a custom-made journal that copies and pastes each ROI in the grid to a running stack. The low alignment error in plate positioning in the automated imager guaranteed that images from each day were only tens of microns apart in alignment. For each set of images, we manually aligned the first pattern of each grid to the exact same pattern to ensure that all stacks are in register.

To quantify the number of cells on each pattern at each day prior to staining, we implemented a graphical user interface in Matlab that displays each image in the daily sequence for one pattern at a time. For each pattern, the user inputs the number of cells (both NPCs and hippocampal astrocytes) at each day. The GUI then automatically updates the data matrix and

loads images for the next pattern in the sequence. By displaying all images for the time sequence at once, we enable the user to make informed judgment calls when distinguishing between overlapping cells. Data can also be saved and reloaded between sessions. See Appendix A-2 for screenshot and code.

Fate scoring for all patterns was done using ImageJ and Excel. All images were rescaled to the same brightness levels during scoring. Population data from days 1-5 were then concatenated to fate scoring data and analyzed using a combination of Excel, Matlab, and GraphPad Prism. We pooled the data from all the micropatterned cells in three well replicates and binned the data according to the number of cells at day 1. Four bins were created, reflecting 1, 2, 3, or 4 initial cells at day 1. Patterns with decreasing populations for the first 2 days (death or detachment) and patterns with zero cells at staining (which may have detached during wash steps) were excluded from the analysis.

Fate scoring for control bulk cultures were performed using CellProfiler to extract cellular features and CellProfiler Analyst to train a classifier based on user-defined training set.

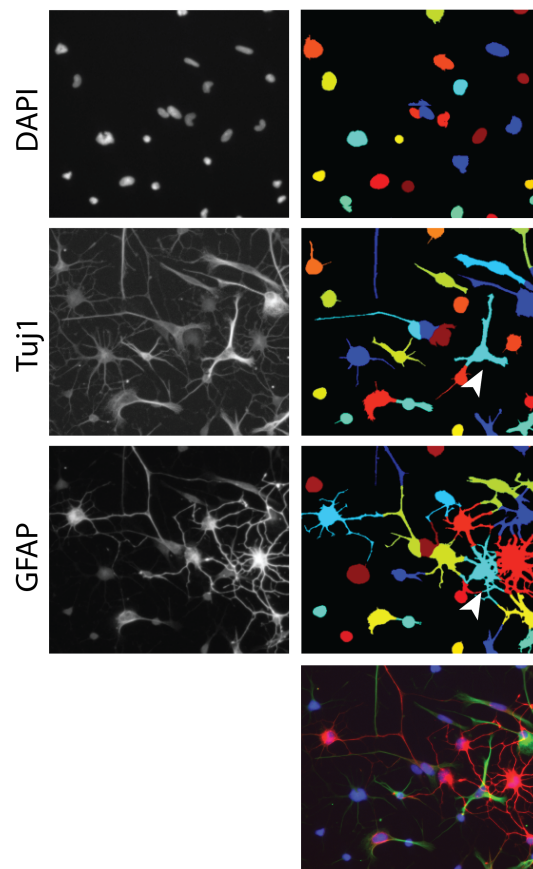


Figure 4-2 CellProfiler segmentation of differentiated NPCs at day 6. Following DAPI segmentation, cytoplasmic features in the FITC channel (Tuj1) and Cy3 channel (GFAP) are segmented using the parent nuclei as seeds in a Voronoi based segmentation algorithm. Segmentation can identify thin and long processes, but is not capable of resolving overlapping processes (see white arrow in color-labeled masks for Tuj1 and GFAP).

### 4.3. Results

#### 4.3.1 Image Processing

We investigated the use of CellProfiler<sup>18</sup> and CellProfiler Analyst for extracting high-content image features from our immunostained cells and classifying cells into appropriate categories based on support vector machine learning algorithms<sup>19</sup>. CellProfiler is an open source cell image analysis software that implements many basic image processing algorithms, which users can organize into a processing pipeline. Notably, the implementation of a Voronoi-based segmentation method<sup>20</sup> dramatically improves the segmentation of cellular cytoplasm, which unlike nuclei, often border on or overlap with adjacent cells.

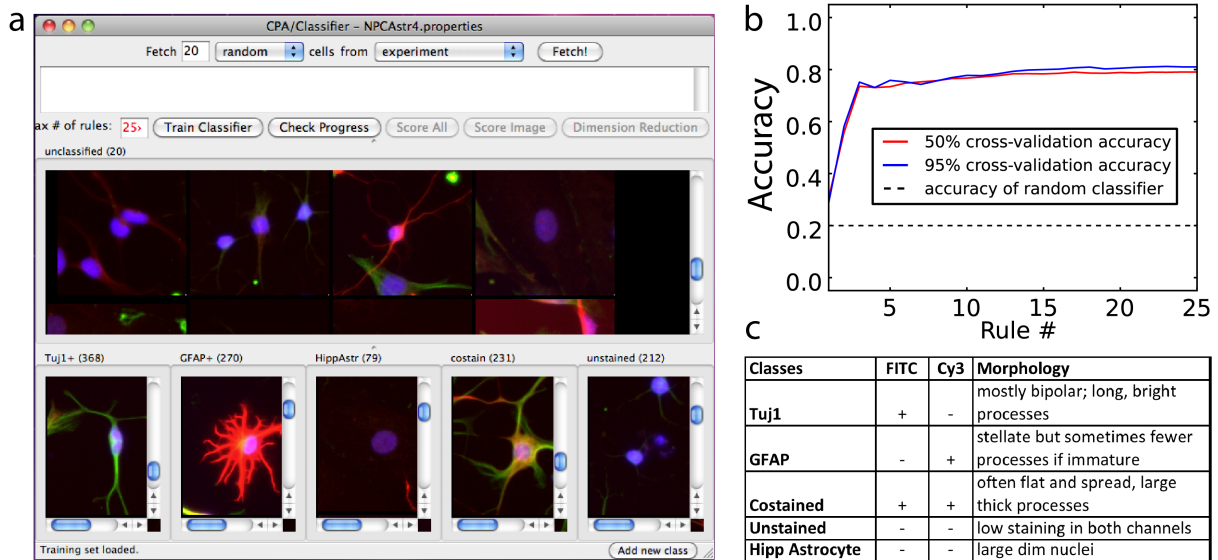


Figure 4-3 Training classifiers in the CellProfiler Analyst interface (a). A training set using approximately 200-300 cells of each type generates a classifier that is approximately 80% accurate when cross-validated (b). Five classifications are used based on the 4 classes of cell types observed in differentiated NPC cultures and the hippocampal astrocyte phenotype (c).

We found that CellProfiler performs well in segmenting immunostained NPCs despite their complex morphologies. In comparison to other intensity-based segmentation algorithms, such as those implemented in MetaXpress [data not shown], CellProfiler segments the Tuj1- and GFAP-stained cytoplasm with accurate morphological boundaries (Figure 4-2). Since morphology provides critical information for classifying cell fate in immunostained NPCs, good performance in this metric is critical. However, CellProfiler is often unable to separate cells that are overlapping such as the cell denoted by the white arrow in Figure 4-2. By eye, we can recognize that the designated cell is mostly Tuj1+ positive and that the bright GFAP+ processes traversing its cell body originate from neighboring GFAP+ cells. However, the



algorithm assigns the cell a GFAP+ cytoplasmic area based on these errant neighboring processes.

To classify the cells, we trained a SVM classifier in CellProfiler Analyst (Figure 4-3) using cells from our control experiment. We created 5 categories with general characteristics as detailed in the table in Figure 4-3c and trained the classifier with 200-300 cells for each category. Although we are primarily concerned with the Tuj1+ and GFAP+ phenotypes, we also separated the “costained” and “unstained” classes so that all elements of each class have similar phenotypes. Because hippocampal astrocytes spread to large areas on flat substrates, they do not appear bright in the GFAP channel. Thus, they are largely identifiable by their large dim nuclei. Cross-validation of the trained classifier resulted in an accuracy of roughly 80% (Figure 4-3b). Additionally, we compared the results from the automated classification to 10 manually classified images and calculated an error of less than 2% for Tuj1+ and GFAP+ percentages. Due to the high number of cells being counted for the control conditions (roughly 5,000 to 25,0000), we reasoned that this level of error would still generate reasonable estimates of population changes across conditions.

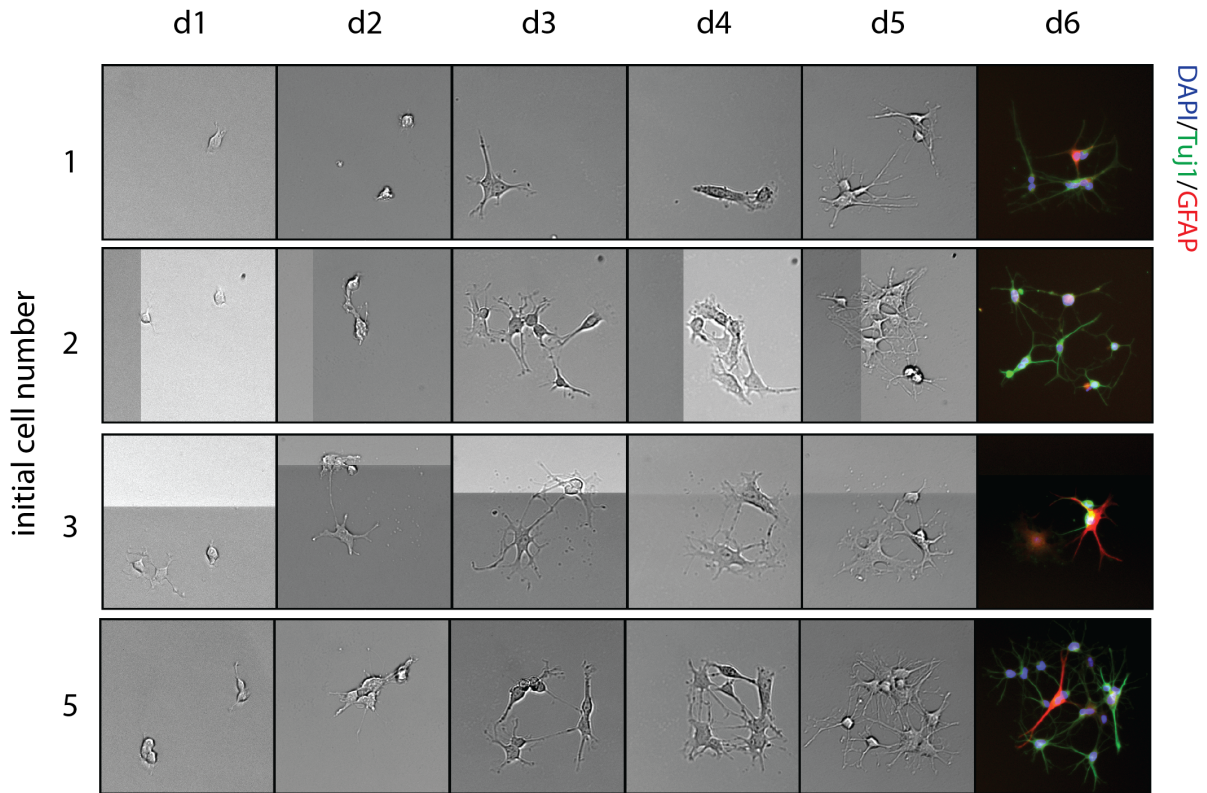


Figure 4-4 Individual patterns during 5 days of brightfield imaging and after immunostaining. Examples are shown for each initial cell number. Since the fate outcome of each pattern is highly stochastic, these images are not meant to be representative of all patterns in each condition. The boundaries between different fields of view can be seen in brightfield images, arising from the inconsistent intensities of the Fiber-Lite lamp.

However, the micropatterned cells exhibited a high degree of overlap due to their confinement in a small area (Figure 4-4). Additionally, after binning patterns by relevant criteria, each condition was represented by only approximately 100-300 samples. Thus, to guarantee higher data quality for these low-sample number conditions, we scored each micropattern manually, using the same visual criteria as defined in Figure 4-3c. Brightfield images from days 1-5 were scored manually as well due to their high degree of overlap and the inconsistencies in image quality resulting from the unorthodox brightfield setup.

#### 4.3.2 Neuronal Differentiation Increased at Higher Densities

As a control, we differentiated NPCs at varying densities to approximate the effect of increasing cell-cell interactions in bulk cultures. We discovered that increased cell density increases Tuj1+ differentiation, regardless of the inclusion of hippocampal astrocytes (Figure 4-5 - solid blue bars). Hippocampal astrocytes reduce Tuj1+ cells for all densities (Figure 4-5 - black patterned bars).

Previous unpublished results from the Schaffer lab report delayed neuronal differentiation with increased densities. However those experiments used higher than average densities (20,000 cells/cm<sup>2</sup>) and in neurogenic medium (1 uM RA, 1 uM forskolin). Thus our results may not be inconsistent with previous findings. The effect of density may be biphasic and/or medium dependent. In medium where Tuj1+ neurons and GFAP+ astrocytes occur at roughly similar proportions, increased cell density may be essential for the specification or maturation of Tuj1+ fates. At our relatively low densities, astrocyte differentiation is not significantly affected by increased densities (Figure 4-5).

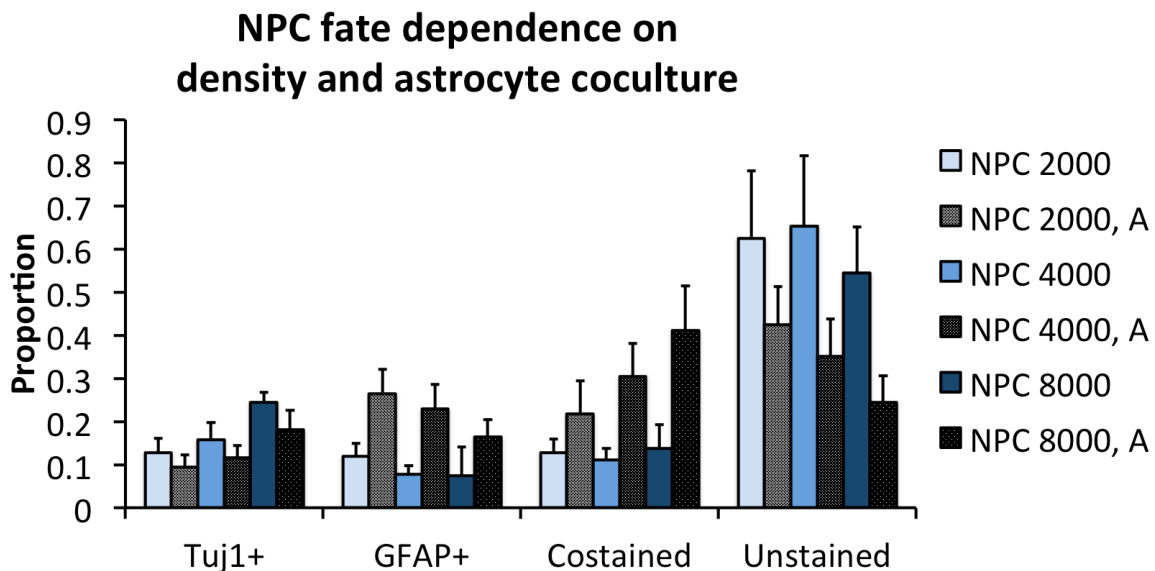


Figure 4-5 Control cultures show differentiation dependence on NPC density and astrocyte co-culture. In mixed differentiation medium (1% FBS and 1 uM RA), higher NPC densities results in higher rates of Tuj1+ neuronal differentiation both with (patterned bars) and without (solid blue bars) hippocampal astrocytes. The addition of hippocampal astrocytes increases GFAP+ astrocyte differentiation for all conditions. Error bars are estimated based on the 80% classification error reported in CellProfiler Analyst cross-validation.

### 4.3.3 Hippocampal Astrocytes Increase Astrocyte Differentiation

We also co-cultured NPCs with hippocampal astrocytes at varying stoichiometries to assess the effect of niche signals on NPCs. Again in contrast to previous findings<sup>11</sup>, we discovered that hippocampal astrocytes increase astrocytic differentiation in mixed differentiation medium. Previously published findings demonstrating that hippocampal astrocytes increase neuronal fate specification used growth factor withdrawal to induce differentiation. Thus it is unclear whether the neurogenic effects of astrocytes are due to increased neuronal fate specification or increased trophic support. By differentiating cells in an inducer concentration capable of supporting both fates, we find that GFAP+ astrocytes are preferentially specified. Additionally, increasing the NPC:hippocampal astrocyte ratio reduces this gliogenic effect (Figure 4-5, black patterned bars).

### 4.3.4 Population Dynamics of Micropatterned NPCs

After collecting and aligning data on NPC growth and final fate distributions on the micropatterns, we first analyzed the population dynamics of the patterns to gauge how long the initial condition is maintained before the first cell division. Assuming a logarithmic growth model described by:

$$P = P_0 * 2^{rt} \quad (4-1)$$

where P is the final population, P<sub>0</sub> is the starting population, r is the rate of proliferation, and t is the time in days, we calculate the proliferation rate r for each pattern in the experiment. We found that the average proliferation rate across all patterns was approximately 0.355 +/- 0.2 (mean +/- SD). By binning the patterns into separate categories defined by their initial numbers of cells (Figure 4-6a), we discovered that patterns with two initial cells exhibited a lower rate of proliferation (p=0.0167, Kruskal-Wallis). Single cells had an average proliferation rate of 0.3872 +/- 0.23 (/day, mean +/- SD) and paired cells had a proliferation rate of 0.3145 +/- 0.205 (/day, mean +/- SD). By these numbers, approximately 30% of single-cell patterns and 40% of paired-cell patterns will have at least one cell division after 24 hours. We generated survival plots for each of the initial cell number conditions and conclude that approximately 50-75% of the patterns have not yet divided by day 2 (Figure 4-6d-g).

We also calculated the average proliferation rate of single cells that only generated Tuj1+ progeny or GFAP+ progeny. Intriguingly, we discovered that single cells with a neuronal bias proliferated more than single cells with a GFAP+ bias (0.4577 +/- 0.232 vs 0.3620 +/- 0.177, p = 0.01, t-test with Welch's correction) (Figure 4-6b). Proliferation rates for patterns with single founder cells varied by day, showing a substantial decrease in proliferation at day 4 (Figure 4-6c). The reason for this difference is unclear but could partly reflect differences in the exact image acquisition time between days.

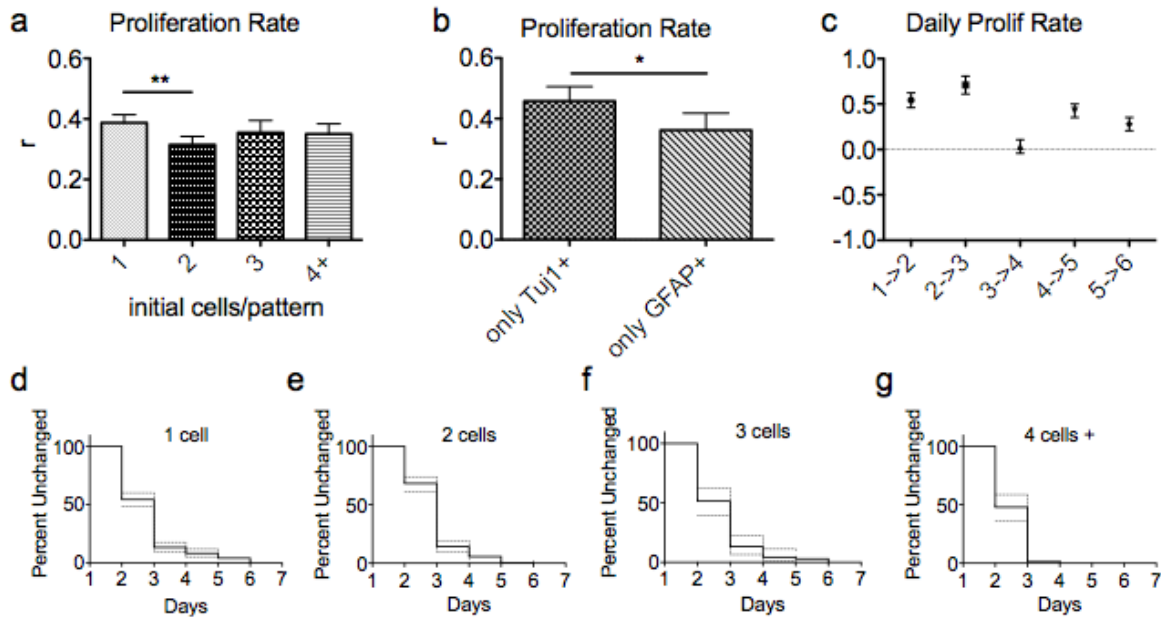


Figure 4-6 Proliferation rate depends on initial number of cells and cell fate propensity. Patterns with 2 initial cells exhibit a lower rate of proliferation than patterns with other numbers of cells ( $p < 0.05$ , Kruskal-Wallis) (b). Tuj1+ biased single cells also exhibit a higher rate of proliferation than GFAP+ biased single cells ( $p < 0.05$ , unpaired t-test with Welch's correction). (c) Daily proliferation rate was assessed for single cell patterns, showing that proliferation decreases at day 4. (d-g) Survival graphs of cell patterns show that approximately 50% (1, 3, and 4+ initial cells) and 75% (2 initial cells) of patterns maintain the initial cell number by day 2 (i.e. cell division has not yet taken place). Dotted lines indicate 95% confidence intervals.

#### 4.3.5 Initial Cell Number Does Not Affect Overall Fate Distributions In Micropatterned NPCs

Results from fate scoring analysis indicate that the initial number of cells on a micropattern does not affect the final distribution of Tuj1+ neurons and GFAP+ astrocytes (Figure 4-8a). We pooled cell counts for all fate classes and calculated percentages for each cell number bin. We discovered that the percentage of final cells that are Tuj1+ and GFAP+ remain at roughly 21% and 7.5% respectively across all sample conditions. The overall fate distributions of Tuj1+ and GFAP+ cells in our micropatterned cultures appear to match the distributions measured at around 8000 initial NSCs/cm<sup>2</sup> for bulk cultures. Although the micropatterns are seeded at 2000 cells/cm<sup>2</sup>, the laminin coated adhesive area is only a fraction (~0.17) of the substrate area. After scaling for the concentrating effect of the micropatterns, the effective cell density of the micropatterned cells is around 9600 cells/cm<sup>2</sup>. The result that single cells do not exhibit significant differences in their final fate distribution is intriguing because it suggests that juxtacrine signals in the first 1-2 days of differentiation are not strictly necessary for initiating differentiation processes. Indeed, in the course of our data analysis, we observed a few examples of single cells differentiating into astrocytes or neurons without any division (Figure 4-7).

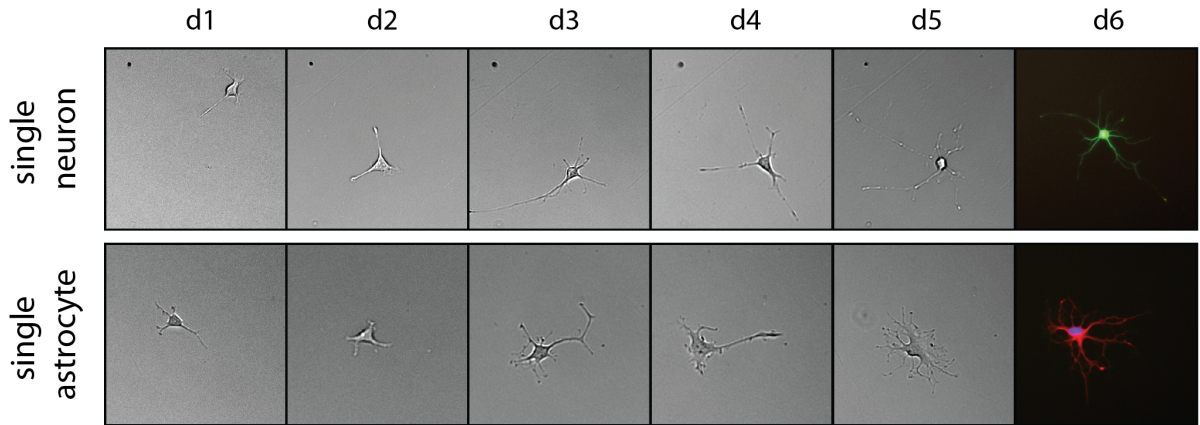


Figure 4-7 Single NPCs differentiating into Tuj1+ neurons (top) or GFAP+ astrocytes. The two share morphological features until day 3 when astrocyte processes begin to look more curved and flattened. Neuronal processes remain thin and relatively straight.

#### 4.3.6 Paired Cells Yield Unexpectedly Low Fate Asymmetry

Since no differences in fate distribution were observed for single, paired, triplet and quadruplet+ cells, one might conclude that a single differentiating NSC has no effect on its neighbor. However, we were also interested in the frequency of fate asymmetry on each pattern and tallied the number of patterns for each condition exhibited asymmetric fates (that had at least one Tuj1+ and GFAP+ cell), only Tuj1+ cells, only GFAP+ cells, or had no differentiated cells (Figure 4-8b). Only 10% of patterns with one initial cell produced mixed progeny, which is lower than the 16.69% value (Figure 4-8c) resulting from a simple simulation treating each cell at day 6 as an independent, identically distributed random variable whose propensities for differentiation are set to the measured percentages for the single cell dataset. This result is not surprising given that fate restriction probably already occurred before division. Indeed studies using embryonic cortical stem cells suggest that even in proliferative conditions (i.e. with bFGF) neural stem cells experience fate restriction such that their progeny have correlated fates<sup>21</sup>.

We then used the percentages of classified patterns from the single cell case to explicitly calculate the probabilities that a pattern with  $n$  initial cells will have a set of mixed progeny by day 6:

$$pAsym_2 = (1 - (1 - pAsym_1)^2) + 2 * (pTuj1_1 * pGFAP_1) \quad (4-2)$$

$$pAsym_3 = (1 - (1 - pAsym_1)^3) + 3 * (pTuj1_1 * pGFAP_1 * (1 - pAsym_1)) \quad (4-3)$$

$$pAsym_4 = (1 - (1 - pAsym_1)^4) + 4 * (pTuj1_1 * pGFAP_1 * (1 - pAsym_1)^2) \quad (4-4)$$



For example, the expected probability that paired cells will exhibit fate asymmetry is the probability that at least one of the mother cells exhibits fate asymmetry (first term, 4-1) plus the probability that one cell only produces Tuj1+ cells while the other only produces GFAP+ cells (second term, 4-1). The subscript specifies the initial number of founder cells. These calculations yielded expected probabilities plotted as black bars in Figure 4-8c.

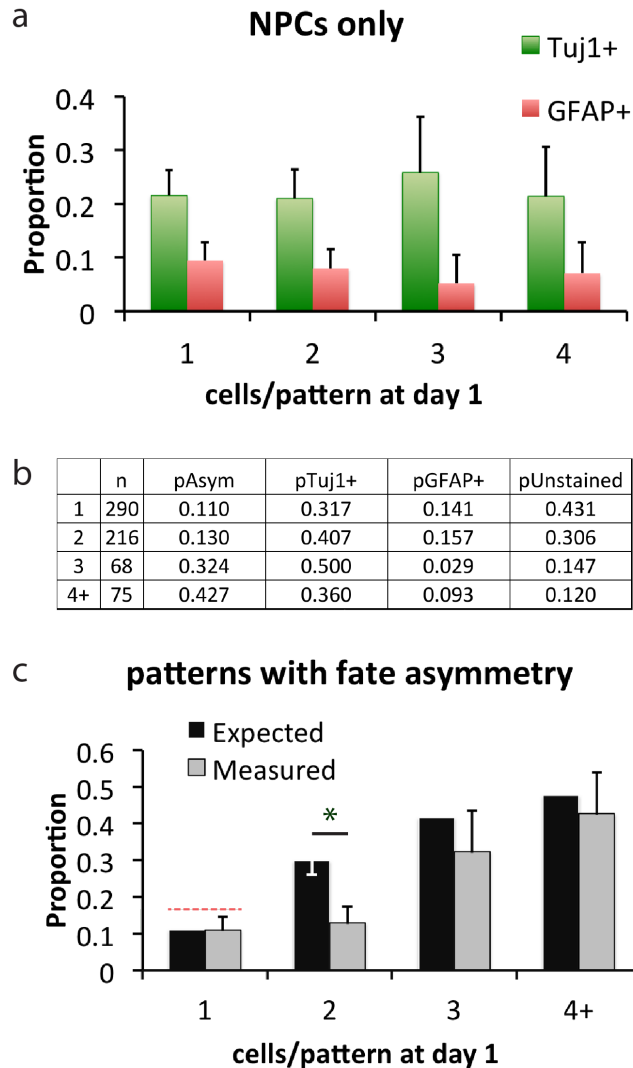


Figure 4-8 Fate distributions of micropatterned NPCs. We observe no differences in overall fate distributions for Tuj1+ and GFAP+ stained cells as a function of the starting numbers of cells (a). We also calculated the percentages of patterns that had fate asymmetry (at least one of each differentiated cell type), Tuj1+ only progeny, GFAP+ only progeny, or no staining (b). Using the probabilities obtained for patterns with a single cell founder, we calculated expected probabilities for the observation of patterns with fate asymmetry for the other conditions. We found that initially paired cells exhibited a significantly lower percentage of fate asymmetry than expected ( $p < 0.001$ , Chi-square). The red line also denotes the expected probabilities of mixed fate patterns for single cells, given the overall fate distributions measured in (a), indicating that single founder also exhibit reduced fate asymmetry in their progeny. This result is expected given that fate restriction probably occurred before division. For (a) and (c), error bars denote 95% confidence intervals ( $n$ =number of patterns for each).

Surprisingly, we discovered that initially paired cells exhibited significantly less fate asymmetry than expected (Figure 4-8c). In fact, the percentage of patterns with asymmetric fates is nearly the same as for the single cell condition (12% vs 10%) (Figure 4-8b-c). For 3 and 4+ initial cells, there are no significant differences between the observed and expected frequencies. These data provide evidence that signaling from a single cell can significantly bias the fate decisions of its neighbor.

We acknowledge that it may be possible that some of our cell pairs are actually the daughter cells of a single cell that divided between cell seeding and imaging at day 1. However, according to our average proliferation rate, only 20% of single cell patterns will theoretically undergo a single cell division within 12 hours. Additionally, we believe this number should be lower given that cells in suspension take approximately 2 hours to fully attach and reboot their cellular machinery. Even if assuming that 20% of the paired patterns originated from single cells, the expected probability of fate asymmetry is only reduced by 5% (white lower error bar, Figure 4-8c), which is still significantly greater than the observed frequency.

Additionally, the absence of any biasing effects in Figure 4-8a lends further support to the idea that the signaling influence of a neighboring cell does not derive from one fate type's trophic requirement for local signals from a neighboring cell. The effect of NPC density on NPC fate (Figure 4-5) seen in bulk cultures is not evident in small micropatterned populations. That is, since the overall fate distributions are the same for a single cell and for a pair of cells, we can reasonably assume that the reduction in fate asymmetry is not simply a matter of all cell pairs preferring one fate type to another.

#### *4.3.7 Single Hippocampal Astrocytes Promote Neuronal Differentiation in Single NPCs*

We found that single hippocampal astrocytes promoted the neuronal cell fate when paired with a single NPC (Figure 9b), but did not yield statistically significant differences for other conditions due to the paucity of hippocampal astrocytes that remained attached to the substrate (Figure 9a). Each condition yielded very few samples, ranging from 8 to 72. The inadequate adhesion of hippocampal astrocytes to micropatterned surfaces may stem in part from the fact that hippocampal astrocytes prefer to spread to very large areas on flat substrates (Figure 9c). Previous work has shown that cells are sensitive to surface area irrespective of the total amount of ECM-integrin engagement. Cells grown on patterns with insufficient area were found to have low viability<sup>22</sup>. Future studies testing single astrocyte influences on NPC fate will need to adjust the adhesion area to accommodate their size.

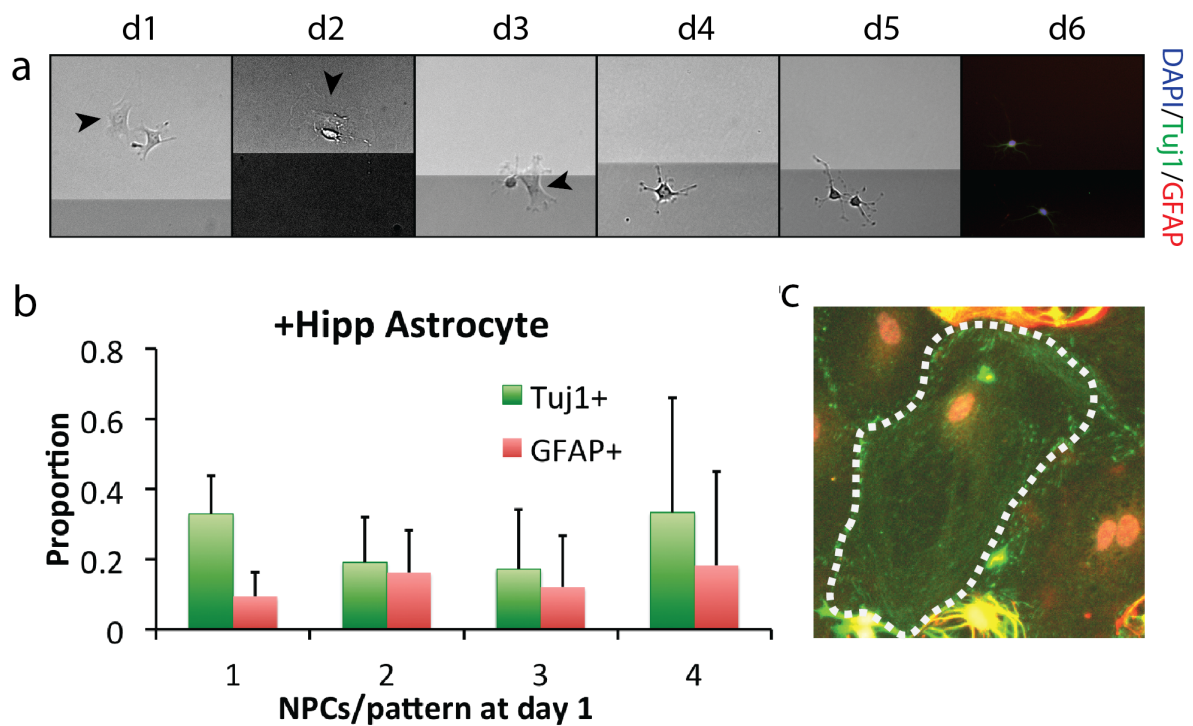


Figure 4-9 Patterns with mixed populations of NPCs and hippocampal astrocytes do not show significant fate biases as a function of NPC:astrocyte stoichiometry, due to poor astrocyte adhesion onto patterns. An example of astrocyte detachment is shown in (a), where an astrocyte (arrowhead) observed at day 1 is detached by day 4. Measured fate distributions as a function of initial NPC number is given in (b). No differences are significant by a two-tailed t-test except for the difference between Tuj1+ and GFAP+ propensities for single NPCs paired with a single hippocampal astrocyte ( $p < 0.05$ , t-test). In (c), astrocytes grown on unpatterned surfaces occupy a large area (dotted line), measuring approximately  $22,000 \text{ um}^2$ , larger than the area of our patterns.

#### 4.4 Discussion

In this work, we present evidence that signaling from single neural progenitor cells can significantly affect the fate decisions of a single neighboring cell. Cells grown on micropatterned islands are constrained to the same interaction partners throughout the course of the 6-day differentiation process. The initial number of cells on each of these micropatterns does not affect the overall distribution of Tuj1+ neurons or GFAP+ cells. However, the percentage of patterns that exhibit fate asymmetry (defined as having more than one of each differentiated cell type) is significantly lower than expected for patterns starting from one cell pair, indicating that persistent cell-cell interactions between two single NPCs can bias fate outcomes of their progeny.

To the best of our knowledge, this is the first time that non-trophic, homotypic single cell influences on mammalian stem cell fates has been reported. Previous work using PEG-hydrogels to pattern defined numbers of mesenchymal stem cells<sup>23</sup> showed that MSC propensities for both osteogenic and adipogenic differentiation increased with an increasing number of cell-cell contacts. However, these results do not necessarily prove that cell-cell



signaling biases cell fate, since the maturation of each fate type was assessed in its corresponding induction medium. Additionally, the shape of the graphs relating differentiation to cell contact number was similar for both cases, suggesting that cell-cell contact supplies trophic signals that are similarly beneficial for both osteogenic and adipogenic differentiation. Another study pairing undifferentiated and neuroectodermally specified embryonic stem cells showed that neuroectodermally committed cells induced Sox1 expression in the uncommitted cells<sup>24</sup>. However, this inductive effect was the result of soluble secreted signals, not cell-cell contact, suggesting that the effect would be similarly or more potent in bulk cultures.

Intriguingly, initial cell number has no effect on fate distributions averaged across all samples in each condition, suggesting that a single cell in a pair influences its neighbor's cell fate in a way that does not favor a particular fate outcome. The addition of a third or fourth neighbor seems to disrupt the signaling balance, resulting in expected numbers of patterns with fate asymmetry.

Unfortunately, we cannot currently arbitrate between two possible mechanisms responsible for the observed phenomenon. One possible mechanism is that single NPCs induce the same fate in their lone neighbor. The fact that previous studies highlighted the trans nature of differentiation cues (i.e. that astroglia enhance neurogenesis<sup>10,11</sup> and neurons enhance oligogenesis<sup>11</sup>) may be due to the fact that those studies induce differentiation by growth factor withdrawal. In addition to providing fate inducing cues, co-cultured astrocytes may also be supplying trophic factors that are differentially essential for different fate outcomes. Our experiments are performed using retinoic acid and FBS, which already provide the factors necessary to produce a mixed population. Theoretically, any observed differences in fate choice will be due to fate induction and not better nutrient availability. Indeed, we observed in our control cultures that NPCs co-cultured with astrocytes in mixed differentiation medium (1  $\mu$ M RA and 1% FBS) exhibited increased astrocytic differentiation for all densities of NPCs. However, we do not know if this kind of lateral induction can occur between single cells at such early stages in the differentiation process (i.e. the 1-2 days prior to the onset of cell division).

The second possibility is that the onset of differentiation in one cell triggers it to laterally inhibit differentiation in its neighbor, possibly through the Notch/Delta pathway<sup>25-28</sup>. Since patterned cells share the same bulk liquid medium, the molecular mechanism for our observed phenotype is likely to be juxtacrine in nature. Feedback in both transcriptional regulation<sup>29</sup> and membrane protein interactions<sup>30</sup> in the Notch/Delta pathway create a bistable heterotypic switch that is known to be responsible for cell fate patterning in the *Drosophila* eye<sup>31</sup> and the *C. Elegans* vulva<sup>32</sup> with single cell resolution. Additionally, Notch/Delta is well-established to be critical for inhibiting differentiation for neural stem cells<sup>33,34</sup> in many different locations<sup>35</sup> and developmental stages<sup>36</sup>. The proper functioning of this pathway is essential for regulating brain size by maintaining undifferentiated progenitor pools during embryonic development<sup>37</sup>.

Similarly, in the postnatal subgranular zone, overexpression of Notch in radial glia dramatically increases progenitor cell proliferation, while Notch ablation causes cell cycle

exit and the transition to neurons or transit amplifying neuronal progenitors<sup>14</sup>. Thus, Notch-mediated lateral inhibition is a likely possible explanation for our observed reduced fate asymmetry in the progeny of initially paired cells, which could serve as a useful *in vitro* model for observing the dynamics of symmetry-breaking in the lateral inhibition process between two cells.

To distinguish between these two possible mechanisms, future work using cell populations with distinct fluorescent transgenes can be used to untangle the relationships between day 6 progeny. Lateral fate induction should produce two subpopulations with correlated neuronal or glial cell fates, whereas lateral inhibition will preferentially produce one differentiated and one undifferentiated subpopulation. Additionally, the introduction of transgene-labeled cells will help us to eliminate cell pairs that may be the product of one cell division between cell seeding and the first imaging timepoint 12 hours later.

In addition to constraining interaction partners through time, micropatterning offers a simple and convenient way to track the behavior of single cells and their progeny at coarse time intervals without necessitating continuous timelapse imaging. By imaging samples at each day, we were able to generate survival graphs to gauge the preservation of the initial cell number across time, and measure proliferation rates for all individual samples and correlate them to their outcomes. Our finding that neuron-only patterns had a faster proliferation rate than astrocyte-only patterns may reflect *in vivo* observations that neurons go through a highly proliferative transit-amplifying stage whereas astrocytes are specified more directly from radial glia<sup>5</sup>. This difference in proliferation may need to be taken into account in assessing fate specification frequencies, as enhanced proliferation in transit-amplifying neuronal precursors may result in overestimates of neuronal fate induction. Indeed, analysis of radial glial-derived clones showed that astrocytes were specified at roughly equal proportions to neurons<sup>5</sup>, and not at a ten-fold lower frequency as estimated in previous lineage tracing experiments<sup>38</sup>.

Certainly, continuous timelapse imaging is ideal and would provide the most detailed information<sup>39</sup> regarding cell lineages, interaction times, and apoptosis (which we cannot currently measure). Micropatterned substrates add to this capability to keeping relevant cells within a microscope field of view<sup>21</sup>. In future work, we aim to make use of timelapse imaging to gain more accurate information about the duration and timing of cell-cell interactions, in conjunction with chemical agonists and blockers of specific pathways (such as Notch and Ephrin) to gain insight into the dynamics and mechanism of fate symmetry induction in paired cells.

## 4.5 References

- 1 Gage, F. H., Takahashi, J. & Palmer, T. D. The Adult Rat Hippocampus Contains Primordial Neural Stem Cells. *Molecular and Cellular Neuroscience* **8**, 389-404,(1997).
- 2 Ma, D. K., Bonaguidi, M. A., Ming, G. L. & Song, H. Adult neural stem cells in the mammalian central nervous system. *Cell Res* **19**, 672-682,(2009).
- 3 Gage, F., Kempermann, G., Song, H. & Laboratory, C. S. H. *Adult neurogenesis*. (Cold Spring Harbor Laboratory Press, 2008).
- 4 Zhang, C.-L., Zou, Y., He, W., Gage, F. H. & Evans, R. M. A role for adult TLX-positive neural stem cells in learning and behaviour. *Nature* **451**, 1004-1007,(2008).
- 5 Bonaguidi, M. A. *et al.* In vivo clonal analysis reveals self-renewing and multipotent adult neural stem cell characteristics. *Cell* **145**, 1142-1155,(2011).
- 6 Seri, B., Garcia-Verdugo, J. M., Collado-Morente, L., McEwen, B. S. & Alvarez-Buylla, A. Cell types, lineage, and architecture of the germinal zone in the adult dentate gyrus. *J Comp Neurol* **478**, 359-378,(2004).
- 7 Willhoite, A. R., Gage, F. H. & Palmer, T. D. Vascular niche for adult hippocampal neurogenesis. *The Journal of Comparative Neurology* **425**, 479-494,(2000).
- 8 Miller, F. D. & Gauthier-Fisher, A. Home at last: neural stem cell niches defined. *Cell stem cell* **4**, 507-510,(2009).
- 9 Lie, D.-C. *et al.* Wnt signalling regulates adult hippocampal neurogenesis. *Nature* **437**, 1370-1375,(2005).
- 10 Ashton, R. S., Conway, A. & Schaffer, D. V. *Astrocytes regulate adult hippocampal neurogenesis through ephrin-B signaling* (2012).
- 11 Song, H., Stevens, C. F. & Gage, F. H. Astroglia induce neurogenesis from adult neural stem cells. *Nature* **417**, 39-44,(2002).
- 12 Lai, K., Kaspar, B. K., Gage, F. H. & Schaffer, D. V. Sonic hedgehog regulates adult neural progenitor proliferation in vitro and in vivo. *Nat Neurosci* **6**, 21-27,(2003).
- 13 Aguirre, A., Rubio, M. E. & Gallo, V. Notch and EGFR pathway interaction regulates neural stem cell number and self-renewal. *Nature* **467**, 323-327,(2010).
- 14 Breunig, J. J., Silbereis, J., Vaccarino, F. M., Sestan, N. & Rakic, P. Notch regulates cell fate and dendrite morphology of newborn neurons in the postnatal dentate gyrus. *Proc Natl Acad Sci U S A* **104**, 20558-20563,(2007).
- 15 Tokunaga, A., Yoon, K., Mizutani, K.-i., Dang, L. & Gaiano, N. Differential Notch signalling distinguishes neural stem cells from intermediate progenitors. *Nature* **449**, 351-355,(2007).
- 16 Taupin, P. *et al.* FGF-2-responsive neural stem cell proliferation requires CCg, a novel autocrine/paracrine cofactor. *Neuron* **28**, 385-397,(2000).
- 17 They, M. & Piel, M. Adhesive micropatterns for cells: a microcontact printing protocol. *Cold Spring Harbor protocols* **2009**, pdb prot5255,(2009).
- 18 Carpenter, A. E. *et al.* CellProfiler: image analysis software for identifying and quantifying cell phenotypes. *Genome biology* **7**, R100,(2006).
- 19 Jones, T. R. *et al.* Scoring diverse cellular morphologies in image-based screens with iterative feedback and machine learning. *Proc Natl Acad Sci U S A* **106**,

- 1826-1831,(2009).
- 20 Jones, T. R., Carpenter, A. & Golland, P. in *Proceedings of the First international conference on Computer Vision for Biomedical Image Applications* 535-543 (Springer-Verlag, Beijing, China, 2005).
- 21 Ravin, R. *et al.* Potency and fate specification in CNS stem cell populations in vitro. *Cell stem cell* **3**, 670-680,(2008).
- 22 Chen, C. S., Ingber, D. E., Whitesides, G. M., Mrksich, M. & Huang, S. Geometric Control of Cell Life and Death. *Science* **276**, 1425-1428,(1997).
- 23 Guan, N., Yao, Y. & Ding, J. [Summary of national meeting on prevention and treatment of pediatric chronic kidney disease in 2009]. *Zhonghua er ke za zhi. Chinese journal of pediatrics* **48**, 371-372,(2010).
- 24 Parekkadan, B. *et al.* Cell-cell interaction modulates neuroectodermal specification of embryonic stem cells. *Neurosci Lett* **438**, 190-195,(2008).
- 25 Artavanis-Tsakonas, S. Notch Signaling: Cell Fate Control and Signal Integration in Development. *Science* **284**, 770-776,(1999).
- 26 Lewis, J. Notch signalling and the control of cell fate choices in vertebrates. *Seminars in Cell and Developmental Biology* **9**, 583-589,(1998).
- 27 Collier, J. R., Lewis, J. H., Monk, N. A. M. & Maini, P. K. Pattern Formation by Lateral Inhibition with Feedback: a Mathematical Model of Delta-Notch Intercellular Signalling. *Journal of Theoretical Biology* **183**, 429-446,(1996).
- 28 Weston, J. A., Maynard, T. M. & Wakamatsu, Y. Fate determination of neural crest cells by NOTCH-mediated lateral inhibition and asymmetrical cell division during gangliogenesis. *Development* **127**, 2811-2821,(2000).
- 29 Kopan, R. & Ilagan, M. X. G. The canonical Notch signaling pathway: unfolding the activation mechanism. *Cell* **137**, 216-233,(2009).
- 30 Sprinzak, D. *et al.* Cis-interactions between Notch and Delta generate mutually exclusive signalling states. *Nature* **465**, 86-90,(2010).
- 31 Fehon, R. G., Johansen, K., Rebay, I. & Artavanis-Tsakonas, S. Complex cellular and subcellular regulation of notch expression during embryonic and imaginal development of *Drosophila*: implications for notch function. *The Journal of cell biology* **113**, 657-669,(1991).
- 32 Lai, E. C. Notch signaling: control of cell communication and cell fate. *Development* **131**, 965-973,(2004).
- 33 Yoon, K. & Gaiano, N. Notch signaling in the mammalian central nervous system: insights from mouse mutants. *Nat Neurosci* **8**, 709-715,(2005).
- 34 Shimojo, H., Ohtsuka, T. & Kageyama, R. Oscillations in notch signaling regulate maintenance of neural progenitors. *Neuron* **58**, 52-64,(2008).
- 35 Nelson, B. R., Hartman, B. H., Lan, M. S., Georgi, S. A. & Reh, T. A. Transient inactivation of Notch signaling synchronizes differentiation of neural progenitor cells. *Developmental biology* **304**, 479-498,(2007).
- 36 Imayoshi, I., Sakamoto, M., Yamaguchi, M., Mori, K. & Kageyama, R. Essential roles of Notch signaling in maintenance of neural stem cells in developing and adult brains. *The Journal of Neuroscience* **30**, 3489-3498,(2010).
- 37 Chambers, C. B. *et al.* Spatiotemporal selectivity of response to Notch1 signals in mammalian forebrain precursors. *Development* **128**, 689-702,(2001).

- 38 Steiner, B. *et al.* Differential regulation of gliogenesis in the context of adult hippocampal neurogenesis in mice. *Glia* **46**, 41-52,(2004).
- 39 Schroeder, T. Imaging stem-cell-driven regeneration in mammals. *Nature* **453**, 345-351,(2008).

## Chapter 5: Concluding Remarks

---

In the subgranular zone of the adult mammalian dentate gyrus, a balance of signals from various sources instructs each resident stem cell to self-renew, differentiate, or remain quiescent. Many decades of *in vivo* and *in vitro* studies has produced a detailed picture of the anatomical features and signaling interactions governing these processes (See Chapter 1.2.2). Though still incomplete, the current model of adult neurogenesis identifies specific roles for niche cells (e.g. that astrocytes promote neurogenesis<sup>1</sup>, neurons promote oligogenesis<sup>1</sup>, and differentiating progenitor cells inhibit stem cell differentiation<sup>2</sup>) and highlights the molecular mediators of some of these effects (Wnt3a<sup>3</sup>, Notch<sup>2,4</sup>, Sonic Hedgehog<sup>5,6</sup>, etc). The recent development of sophisticated genetic techniques for tissue-specific labeling of individual stem cell clones<sup>7-9</sup> also provides an unprecedented glimpse into the natural progression of tissue regeneration in the SGZ, and in response to mutations in specific pathways (such as the PTEN tumor suppressor pathway)<sup>7</sup>.

However, what we are still missing is an understanding of how these complex, dynamic, and often contradictory influences on stem cell fate are integrated to form a concerted decision. Are signals from specific niche cells dominant over others? Or are signals instructing a particular fate decision dominant? Does each niche cell type display consistent fate regulatory signals or does each niche cell type itself promote contradictory fate outcomes? One review<sup>10</sup> highlighted the potential for astrocytes to induce oligogenesis by citing the finding that PDGFR signaling in radial glia increases oligogenesis<sup>11</sup>, and that astrocytes are known to secrete PDGFA. Characterizing the relative dominance of well-known instructive cues will also provide insight into the underlying stochasticity or determinism of differentiation and self-renewal processes.

These questions are not easy to address *in vivo*, where the signaling history of a particular clone is practically impossible to determine. Exogenous alterations in the signaling environment, through the introduction of conditional genetic knock-in/knockouts, establishes

in broad strokes how a particular pathway can affect stem cell differentiation by overexpressing or ablating specific genes. However, these techniques do not provide insight on how cells disambiguate between endogenous levels of contradictory signals. To observe the dynamic signaling environment of a neural stem cell, one would need to use long-term *in vivo* imaging in conjunction with appropriate fluorescent markers. Even with the improved tissue penetrance of long-wavelength light used in multiphoton imaging, *in vivo* timelapse imaging is an incredibly difficult technique<sup>12</sup> and has only been successfully implemented in a handful of stem cell studies<sup>13-15</sup>.

By contrast, the signaling environment of a single stem cell *in vitro* can be both controlled and monitored through a combination of micropatterning techniques and timelapse imaging, which is much more tractable *in vitro*. Microscale tools and devices made using photolithographic processes can exert positional control over cultured cells, down to a single cell<sup>16-19</sup>. Even simple capabilities such as substrate micropatterns<sup>20-22</sup> can enable critical functionalities such as the restriction of cell motility to a microscope-field-of-view or to enforce persistent interactions with a neighboring cell and its progeny. Already, these techniques have been used to great effect in tracing lineages in adult neural progenitors<sup>23,24</sup>, cortical neuronal precursors<sup>25</sup> and other cell types<sup>26</sup>, or for distinguishing between cell division rate and apoptosis in characterizing proliferation<sup>27</sup>. However, these studies have not systematically investigated the influence of neighboring cells in differentiation decisions, despite clear evidence of their interactions.

The goal of our work was two-fold: to develop methods for interrogating and constraining cell-cell interactions between limited numbers of cells (Chapters 2-4) and to demonstrate that these methods can be used to detect single-cell influences on neural stem cell fate *in vitro* (Chapter 4). We found that differentiating pairs of NPCs exhibited significantly reduced fate asymmetry, pointing to a possible mechanism of lateral fate induction or differentiation repression between two differentiating cells. This exciting discovery that single-cell interactions can exert significant biases on cell fate *in vitro* will pave the road for future work in elucidating the dynamics, and molecular mechanisms at play in mediating homotypic interactions between differentiating NPCs.

Importantly, these methods can also be used characterize how neighboring niche cells instruct NPC fate both in isolation and in combination. Though our initial studies using hippocampal astrocytes did not produce significant results due to astrocyte de-adhesion and low sample number, the micropatterning method can be optimized to improve the adhesion of astrocytes and other niche cell types (such as granule neurons<sup>28</sup>). Combinatorial co-cultures of single NPCs with other niche cell types will help us construct a better picture of how stem cells make decisions in the face of conflicting signals. Future efforts along these lines will be catalyzed by the development of improved automated data processing tools and statistical models that accurately characterize the discrete fate transitions that form the basis of our measurement.

In summary, *in vitro* reconstitution and continuous monitoring of the cellular components of the neural stem cell niche will allow us to better understand the complex local signals that

regulate stem cell differentiation and integration into a surrounding tissue. Dysregulation of the signaling microenvironment can cause a host of problems including the premature depletion of the stem cell population<sup>9,29,30</sup>, poor structural and functional integration of differentiating cells into their terminal destination<sup>31</sup>, or unchecked growth of stem cells containing latent oncogenic mutations<sup>32,33</sup>. From a scientific perspective, it will also be exciting to ascertain whether certain niche cell influences on stem cell fate dominate over others. The fine-grain mechanistic understanding of these stem cell niches will be useful in the design of cellular and molecular therapies for regenerative medicine.



## References

- 1 Song, H., Stevens, C. F. & Gage, F. H. Astroglia induce neurogenesis from adult neural stem cells. *Nature* **417**, 39-44,(2002).
- 2 Aguirre, A., Rubio, M. E. & Gallo, V. Notch and EGFR pathway interaction regulates neural stem cell number and self-renewal. *Nature* **467**, 323-327,(2010).
- 3 Lie, D.-C. *et al.* Wnt signalling regulates adult hippocampal neurogenesis. *Nature* **437**, 1370-1375,(2005).
- 4 Tokunaga, A., Yoon, K., Mizutani, K.-i., Dang, L. & Gaiano, N. Differential Notch signalling distinguishes neural stem cells from intermediate progenitors. *Nature* **449**, 351-355,(2007).
- 5 Lai, K., Kaspar, B. K., Gage, F. H. & Schaffer, D. V. Sonic hedgehog regulates adult neural progenitor proliferation in vitro and in vivo. *Nature neuroscience* **6**, 21-27,(2002).
- 6 Han, Y. G. *et al.* Hedgehog signaling and primary cilia are required for the formation of adult neural stem cells. *Nat Neurosci* **11**, 277-284,(2008).
- 7 Bonaguidi, M. A. *et al.* In vivo clonal analysis reveals self-renewing and multipotent adult neural stem cell characteristics. *Cell* **145**, 1142-1155,(2011).
- 8 Zong, H., Espinosa, J. S., Su, H. H., Muzumdar, M. D. & Luo, L. Mosaic analysis with double markers in mice. *Cell* **121**, 479-492,(2005).
- 9 Balordi, F. & Fishell, G. Mosaic removal of hedgehog signaling in the adult SVZ reveals that the residual wild-type stem cells have a limited capacity for self-renewal. *J Neurosci* **27**, 14248-14259,(2007).
- 10 Miller, F. D. & Gauthier-Fisher, A. Home at last: neural stem cell niches defined. *Cell stem cell* **4**, 507-510,(2009).
- 11 Jackson, E. L. *et al.* PDGFR alpha-positive B cells are neural stem cells in the adult SVZ that form glioma-like growths in response to increased PDGF signaling. *Neuron* **51**, 187-199,(2006).
- 12 Schroeder, T. Imaging stem-cell-driven regeneration in mammals. *Nature* **453**, 345-351,(2008).
- 13 Lo Celso, C. *et al.* Live-animal tracking of individual haematopoietic stem/progenitor cells in their niche. *Nature* **457**, 92-96,(2009).
- 14 Shinin, V., Gayraud-Morel, B., Gomes, D. & Tajbakhsh, S. Asymmetric division and cosegregation of template DNA strands in adult muscle satellite cells. *Nat Cell Biol* **8**, 677-687,(2006).
- 15 Kuang, S., Kuroda, K., Le Grand, F. & Rudnicki, M. A. Asymmetric self-renewal and commitment of satellite stem cells in muscle. *Cell* **129**, 999-1010,(2007).
- 16 Di Carlo, D., Wu, L. Y. & Lee, L. P. Dynamic single cell culture array. *Lab on a chip* **6**, 1445-1449,(2006).
- 17 Rettig, J. R. & Folch, A. Large-Scale Single-Cell Trapping And Imaging Using Microwell Arrays. *Analytical chemistry* **77**, 5628-5634,(2005).
- 18 Chung, K., Rivet, C. A., Kemp, M. L. & Lu, H. Imaging single-cell signaling dynamics with a deterministic high-density single-cell trap array. *Anal Chem* **83**, 7044-7052,(2011).
- 19 Skelley, A. M., Suh, H., Voldman, J., Kirak, O. & Jaenisch, R. Microfluidic control of

- cell pairing and fusion. *Nature methods* **6**, 147-152,(2009).
- 20 Chen, C. S., Mrksich, M., Huang, S., Whitesides, G. M. & Ingber, D. E. Micropatterned surfaces for control of cell shape, position, and function. *Biotechnology progress* **14**, 356-363,(1998).
- 21 Chen, C. S. & Raghavan, S. Micropatterned Environments in Cell Biology. *Advanced Materials* **16**, 1303-1313,(2004).
- 22 Théry, M. Micropatterning as a tool to decipher cell morphogenesis and functions. *Journal of cell science* **123**, 4201-4213,(2010).
- 23 Costa, M. R. *et al.* Continuous live imaging of adult neural stem cell division and lineage progression in vitro. *Development* **138**, 1057-1068,(2011).
- 24 Gomes, F. L. a. F. *et al.* Reconstruction of rat retinal progenitor cell lineages in vitro reveals a surprising degree of stochasticity in cell fate decisions. *Development* **138**, 227-235,(2011).
- 25 Ravin, R. *et al.* Potency and fate specification in CNS stem cell populations in vitro. *Cell stem cell* **3**, 670-680,(2008).
- 26 Eilken, H. M., Nishikawa, S. & Schroeder, T. Continuous single-cell imaging of blood generation from haemogenic endothelium. *Nature* **457**, 896-900,(2009).
- 27 Gilbert, P. M. *et al.* Substrate Elasticity Regulates Skeletal Muscle Stem Cell Self-Renewal in Culture. *Science* **1902**, 1078-1081,(2010).
- 28 Bilimoria, P. M. & Bonni, A. Cultures of cerebellar granule neurons. *CSH protocols* **2008**, pdb prot5107,(2008).
- 29 Depaepe, V. *et al.* Ephrin signalling controls brain size by regulating apoptosis of neural progenitors. *Nature* **435**, 1244-1250,(2005).
- 30 Imayoshi, I. & Kageyama, R. The role of Notch signaling in adult neurogenesis. *Mol Neurobiol* **44**, 7-12,(2011).
- 31 Bergami, M. *et al.* Deletion of TrkB in adult progenitors alters newborn neuron integration into hippocampal circuits and increases anxiety-like behavior. *Proc Natl Acad Sci U S A* **105**, 15570-15575,(2008).
- 32 Sanai, N., Alvarez-Buylla, A. & Berger, M. S. Neural stem cells and the origin of gliomas. *The New England journal of medicine* **353**, 811-822,(2005).
- 33 Wong, S. Y. & Reiter, J. F. Wounding mobilizes hair follicle stem cells to form tumors. *Proc Natl Acad Sci U S A* **108**, 4093-4098,(2011).

## Appendix A – Matlab Code

### *A-1 Reshist*

```
function residences = resHist(filename);
% resHist is used to plot a histogram of all the residence times
% that a cell spends in a well. The input data should be a
% numerical array, with each column representing the cell occupancy %
% of a single well over time.
%
% Counting Rubric
%
% Cell migrating out (cell body half way):           -1
% Cell division:                                     +1
% *External cell body touching cells in well:       - # cells
% Migration of cell into empty well:                 0
%
% To account for other cells entering the well, please construct a
% list of the wells to exclude, titles: 'list_excludelast.txt');
%
% columns corresponds to wells, rows correspond to movie frames

data = dlmread(filename);
exclude = dlmread('list_excludelast.txt');
colnum = size(data,2);
frnum = size(data,1);

oneResTimes = [];
twoResTimes = [];
threeResTimes = [];

for i = 1:colnum

    numbers = data(:,i);

    if exclude(i)
        x = find(numbers~=0);
        lastdigit = numbers(x(end));
        y = find(numbers == lastdigit);
        deriv = diff(y);

        %find any discontinuities in seq with only last digit

        if diff(y)>1
            seqstart = y(find(diff(y)>1)+1);
            numbers = numbers(1:seqstart-1);
        else
```

```

        numbers=numbers(1:y(1)-1);
    end
end

if ~isempty(numbers)
    s = sprintf('%d',numbers); %write the sequence as a string

    t1=textscan(s,'%s', ...
                'delimiter','0 2 3','multipleDelimsAsOne' , 1) ;
    d1 = t1{1};

    for k = 1:length(d1)

        % division checks if the sequence of 1's occurs right
        % before a cell division event. These sequences are
        % eliminated

        division = findstr(s, strcat(d1{k}, '2'));
        if isempty(division)
            resTime = 10*length(d1{k});
            oneResTimes = [oneResTimes resTime];
        end

    end

    t2=textscan(s,'%s','delimiter','0 1 , ...
                3','multipleDelimsAsOne',1);
    d2 = t2{1};

    for k = 1:length(d2)
        resTime = 10*length(d2{k});
        twoResTimes = [twoResTimes resTime];
    end

    t3=textscan(s,'%s','delimiter','0 1 2' , ...
                'multipleDelimsAsOne',1);
    d3 = t3{1};

    for k = 1:length(d3)
        resTime = 10*length(d3{k});
        threeResTimes = [threeResTimes resTime];
    end
end

end

subplot(3,1,1);
hist(oneResTimes, [1:max(oneResTimes)]);
xlabel('residence time (min)');

```

```

ylabel('# times');
axis([0 1500 0 5]);
title('one cell', 'FontWeight', 'bold');

subplot(3,1,2);
hist(twoResTimes, [1:max(twoResTimes)]);
xlabel('residence time (min)');
ylabel('# times');
axis([0 1500 0 5]);
title('two cells', 'FontWeight', 'bold')

subplot(3,1,3)
hist(threeResTimes, [1:max(threeResTimes)]);
xlabel('residence time (min)');
ylabel('# times');
axis([0 1500 0 5]);
title('three cells', 'FontWeight', 'bold')


figure;
h1 = barweb([mean(oneResTimes) mean(twoResTimes)
mean(threeResTimes)],...
            [std(oneResTimes) std(twoResTimes) std(threeResTimes)],0.6,
            [], 'mean residence times', [], 'residence time(min)', [], [], {'one
cell', 'two cells', 'three cells'});

residences = {oneResTimes, twoResTimes, threeResTimes};

```

# A-2 CellStackCounter

cellstackcounter



Astrocytes:

Day 1 NSCs:



Astrocytes:

Day 2 NSCs:



Astrocytes:

Day 3 NSCs:



Astrocytes:

Day 4 NSCs:



Astrocytes:

Day 5 NSCs:

Open

Partially processed?

Previous site

NPcAstrd\_p1\_A1\_d1\_stack.stik  
 NPcAstrd\_p1\_A1\_d2\_stack.stik  
 NPcAstrd\_p1\_A1\_d3\_stack.stik  
 NPcAstrd\_p1\_A1\_d4\_stack.stik  
 NPcAstrd\_p1\_A1\_d5\_stack.stik

Panel

Undo

Save

Slice #: 6

5	4	5	6	7
4	0	0	0	0
3	6	7	14	19
2	1	1	3	3
1	0	0	0	0

```

function varargout = cellstackcounter(varargin)
% CELLSTACKCOUNTER M-file for cellstackcounter.fig
%
% This simple program allows the user to quickly input the number % of
% cells at each slide in a stack, which is shown iteratively to % the user
% until the end of the stack is reached. Once the end of % the stack has
% been reached, the data should be saved using the
% save button, which generates a .mat file of the same name with
% the data table stored in it in variable x. The data table is an % nx2
% matrix where the first column stores the slice number and
% the second column stores the number of cells at each slice.
% Additionally, the user can save the data at any point and reload
% it by checking "partially processed" before opening the stack
% file. 'Undo' also scrolls back the images and data if the user
% has realized there he/she has made an error.

% Begin initialization code - DO NOT EDIT
gui_Singleton = 1;
gui_State = struct('gui_Name',      mfilename, ...
                  'gui_Singleton',  gui_Singleton, ...
                  'gui_OpeningFcn', @cellstackcounter_OpeningFcn, ...
                  'gui_OutputFcn',  @cellstackcounter_OutputFcn, ...
                  'gui_LayoutFcn',  [], ...
                  'gui_Callback',    []);
if nargin && ischar(varargin{1})
    gui_State.gui_Callback = str2func(varargin{1});
end

if nargout
    [varargout{1:nargout}] = gui_mainfcn(gui_State, varargin{:});
else
    gui_mainfcn(gui_State, varargin{:});
end
% End initialization code - DO NOT EDIT

% --- Executes just before cellstackcounter is made visible.
function cellstackcounter_OpeningFcn(hObject, eventdata, ...
                                     handles, varargin)

%Initialize CellStack Counter variables:

% Choose default command line output for cellstackcounter
handles.output = hObject;

% Update handles structure
guidata(hObject, handles);

```

```
% --- Outputs from this function are returned to the command line.  
function varargout = cellstackcounter_OutputFcn(hObject, ....  
                eventdata, handles)
```

```
% Get default command line output from handles structure  
varargout{1} = handles.output;
```

```
% --- Executes on button press in undo.  
function undo_Callback(hObject, eventdata, handles)
```

```
if handles.n == 1
```

```
    display('cannot go back');
```

```
else
```

```
    % roll n back by 1  
    handles.n = handles.n - 1;  
    n = handles.n;
```

```
    % roll displayed image back by 1  
    plotpictures(handles);
```

```
    % roll data in uitable1 back by 1  
    tabledata = get(handles.uitable1, 'Data');  
    tabledata = tabledata(2:n,:);  
    set(handles.uitable1, 'Data', tabledata);
```

```
end
```

```
guidata(hObject, handles);
```

```
uiresume();
```

```
% --- Executes on button press in save.  
function save_Callback(hObject, eventdata, handles)
```

```
tabledata = get(handles.uitable1, 'Data');  
x = flipud(tabledata);  
save([handles.pathname, handles.basename, '.mat'], 'x');  
guidata(hObject, handles);
```

```
% --- Executes on button press in open.  
function open_Callback(hObject, eventdata, handles)
```

```
[filename, pathname, filterindex] = uigetfile('.stk', 'Please select all
```



```

brightfield stack.', 'MultiSelect', 'On');
handles.filename = filename; %cell array of all filenames, by day
handles.pathname = pathname;
handles.basename = filename{1}(1:end-13);
handles.stkloaded = 1; % indicated whether stack is loaded
set(handles.fname, 'String', filename); %update filename in GUI

handles.totalnum = 841; %hard coded for now.

if get(handles.partialprocessed, 'Value');

    % load the value of the list
    load(strcat(handles.basename, '.mat'));

    % set uitable Data to data variable from mat file
    set(handles.uitable1, 'Data', flipud(x));

    % set n = size of data
    n = size(x,1)+1;
    handles.n = n;

    % set size number indicator
    set(handles.slicenum, 'String', num2str(handles.n));

    % load appropriate images into current windows
    plotpictures(handles);

else %nothing has been processed
    handles.n = 1;
    set(handles.uitable1, 'Data', []);
    plotpictures(handles);

end

guidata(hObject, handles);

% --- Executes on key press
function d5input_Callback(hObject, eventdata, handles)

if handles.n<=handles.totalnum
    if handles.stkloaded

        % Adds new input value into the Data variable in uitable1,
        % also flipped the table data because the table won't scroll %
        % to the bottom automatically. Thus, the table looks like a % LIFO
        % stack.

        tabledata = get(handles.uitable1, 'Data');

```

```

%read all inputs at each textbox
allrows = [handles.n];

for i=1:5
    handlename = strcat('handles.d', num2str(i), 'input');
    currhandle = eval(handlename);
    currstr = get(currhandle, 'String');
    currnum = str2num(currstr);
    allrows = [allrows currnum];
    set(currhandle, 'String', '0'); %set curr handle to 0.
end

%Add Astrocyte (day 1-day5) data to the matrix

for i=1:5
    handlename = strcat('handles.Astr_d', num2str(i), ...
                        'input');
    currhandle = eval(handlename);
    currstr = get(currhandle, 'String');
    currnum = str2num(currstr);
    allrows = [allrows currnum];
    set(currhandle, 'String', '0'); %set curr handle to 0.
end

tabledata = [flipud(tabledata); allrows];
set(handles.uitable1, 'Data', flipud(tabledata));

handles.n = handles.n+1;

%update slice label
set(handles.slicenum, 'String', num2str(handles.n));

if handles.n <= handles.totalnum

    plotpictures(handles);

else
    display('No more pictures!');
end
else
    display('No Stack Loaded')
end

end
else
    display ('No more pictures!')
end

guidata(hObject, handles);

```

```
% --- Executes during object creation, after setting all properties.  
function d5input_CreateFcn(hObject, eventdata, handles)
```

```
if ispc && isequal(get(hObject,'BackgroundColor'),  
get(0,'defaultUicontrolBackgroundColor'))  
    set(hObject,'BackgroundColor','white');  
end  
guidata(hObject, handles);
```

```
% --- Executes on key press with focus on d5input  
function d5input_KeyPressFcn(hObject, eventdata, handles)
```

```
if(strcmp(eventdata.Key,'return'))  
    set(handles.d5input, 'String', '');  
end  
  
guidata(hObject, handles);
```

```
% --- Plots all the pictures at n  
function plotpictures(handles)
```

```
%plot previous pictures in prev axes if n>1  
if handles.n>1  
    for i = 1:5  
  
        datastruct = tiffread2(handles.filename{i},(handles.n-1));  
        currIm = datastruct.data;  
        %rescale image by maximum within middle 450x450 subsection  
  
        cropIm = currIm(45:495,45:495);  
        high = double(max(max(cropIm)));  
        low = double(min(min(cropIm)));  
  
        currIm = mat2gray(currIm, [low high]);  
        handlename = strcat('handles.prev_axes', num2str(i));  
        currhandle = eval(handlename);  
        imshow(currIm, 'Parent', eval(handlename));  
    end  
end  
  
%plot current pictures in axes  
for i = 1:5  
  
    datastruct = tiffread2(handles.filename{i},handles.n);  
    currIm = datastruct.data;  
    %rescale image by maximum within middle 450x450 subsection
```

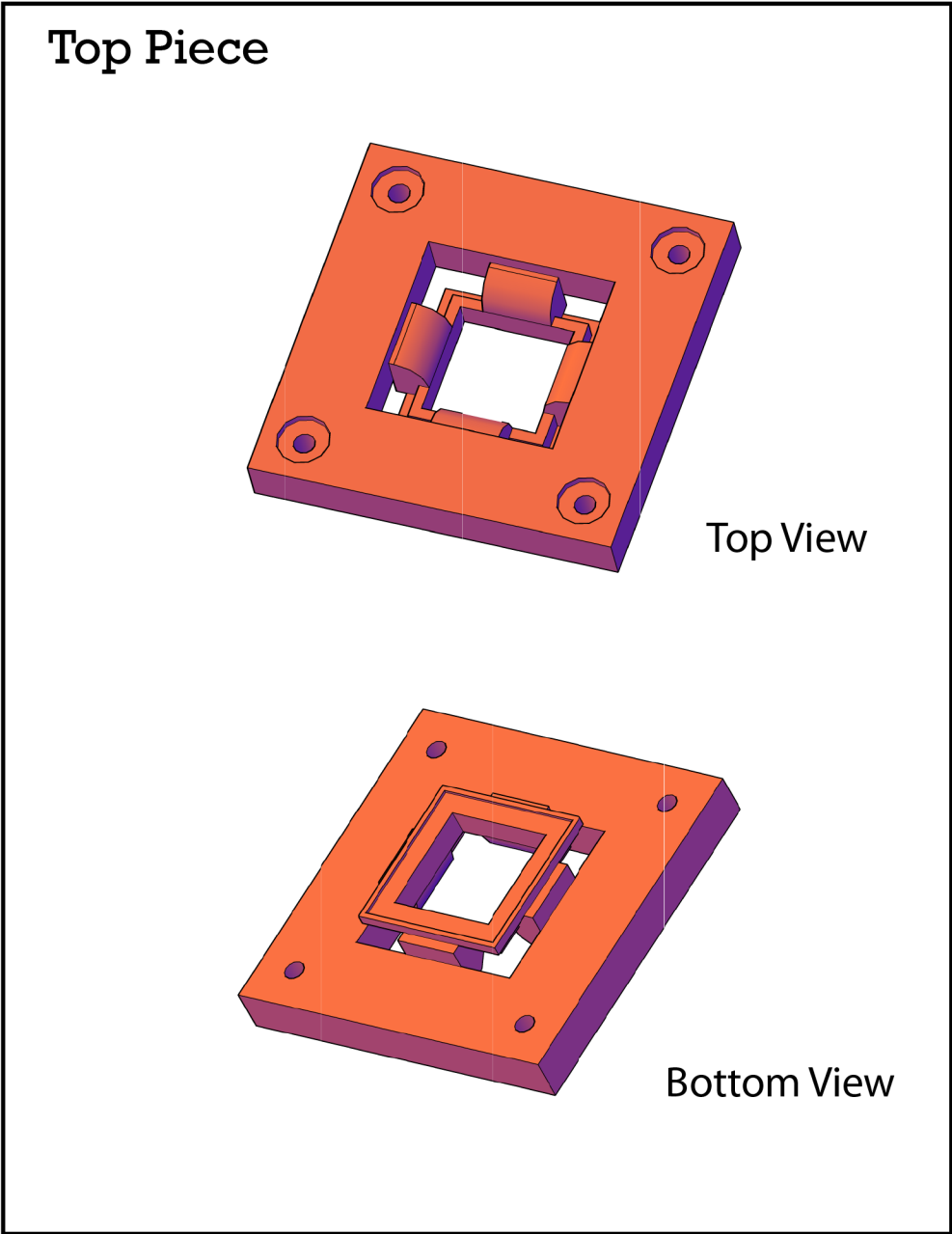
```
cropIm = currIm(45:495,45:495);
high = double(max(max(cropIm)))
low = double(min(min(cropIm)))

currIm = mat2gray(currIm, [low high]);
handlename = strcat('handles.axes', num2str(i));
currhandle = eval(handlename);
imshow(currIm, 'Parent', eval(handlename));
end

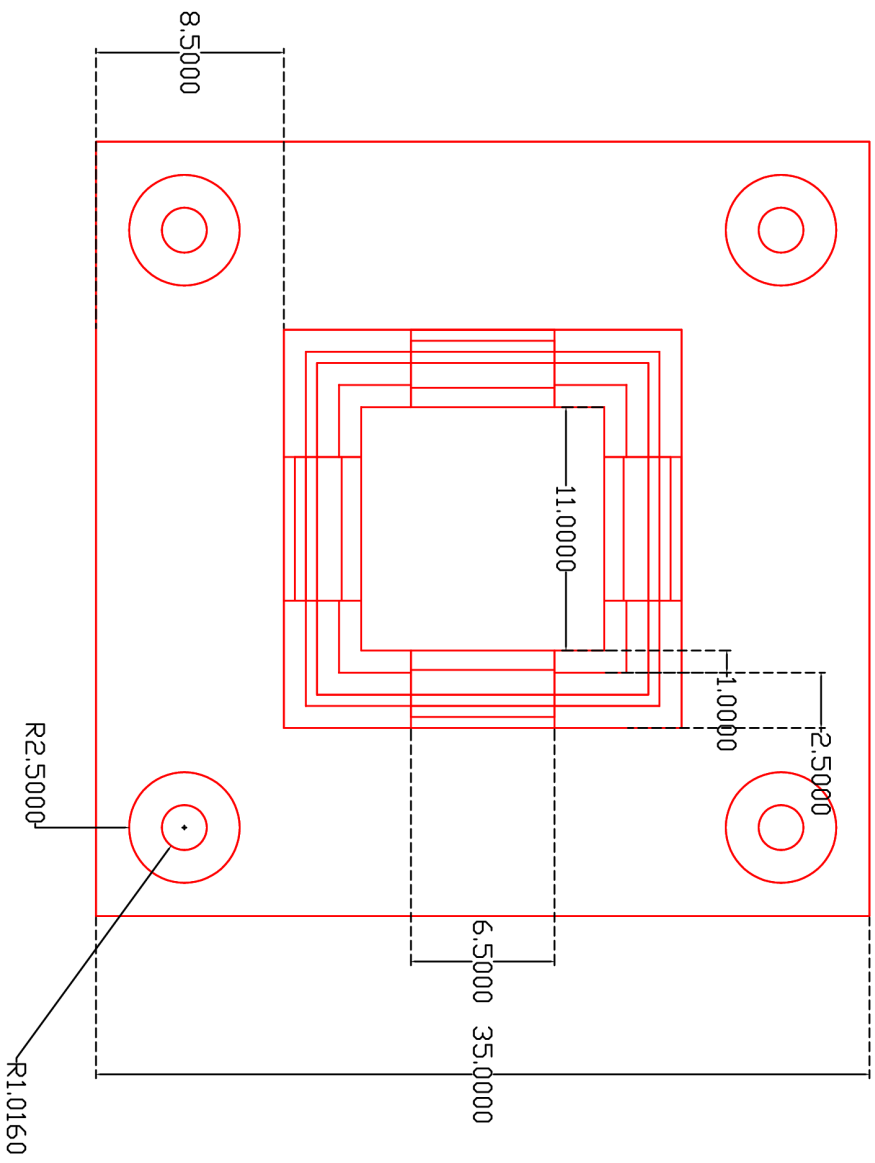
% All other elements do not have callbacks so they are not
% represented here.
```

# Appendix B – Annotated AutoCAD designs for Chapter 3

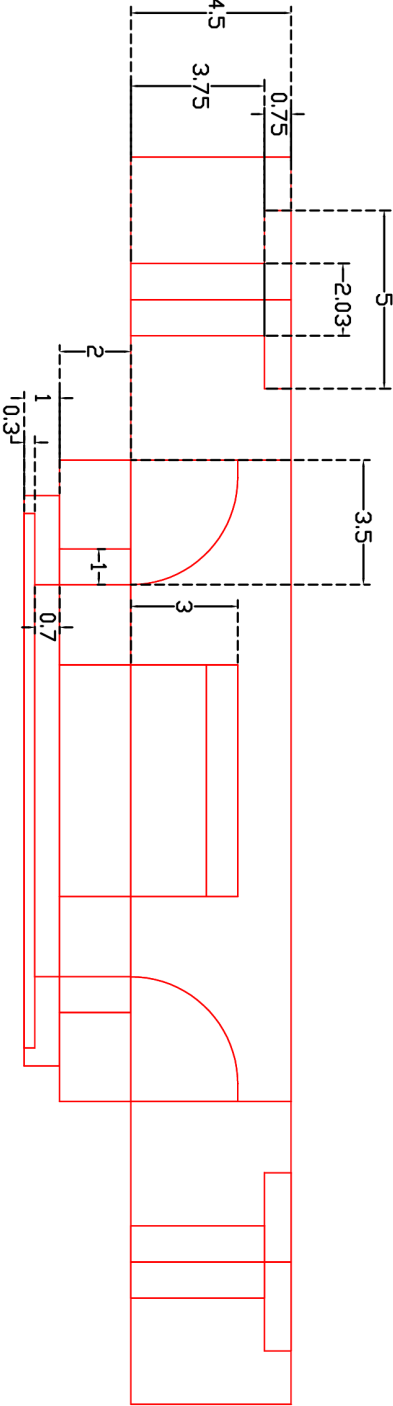
All annotations are in mm.



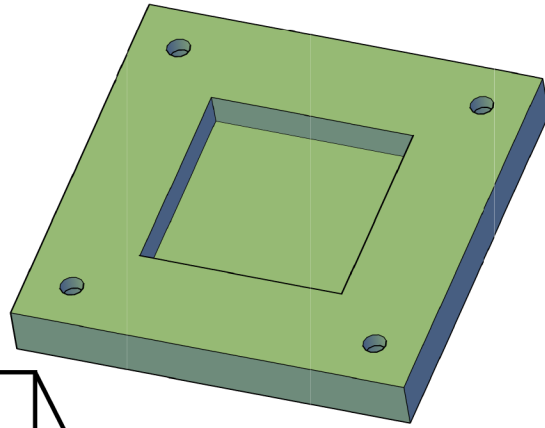
# Top Piece - Top Annotation



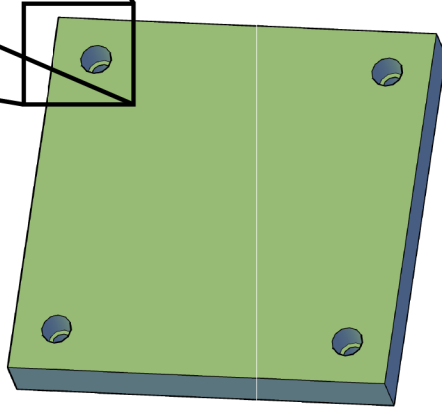
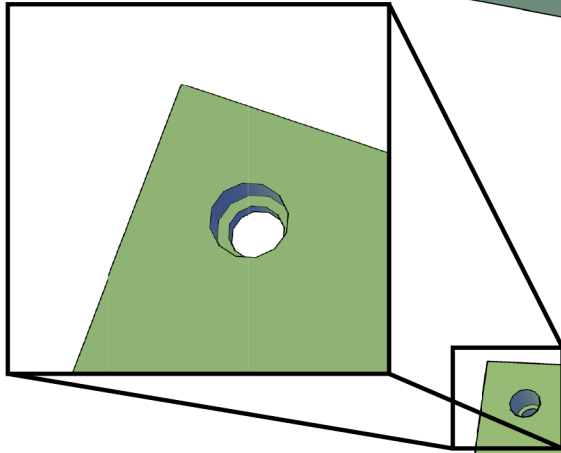
# Top Piece - Side Annotation



# Bottom Piece



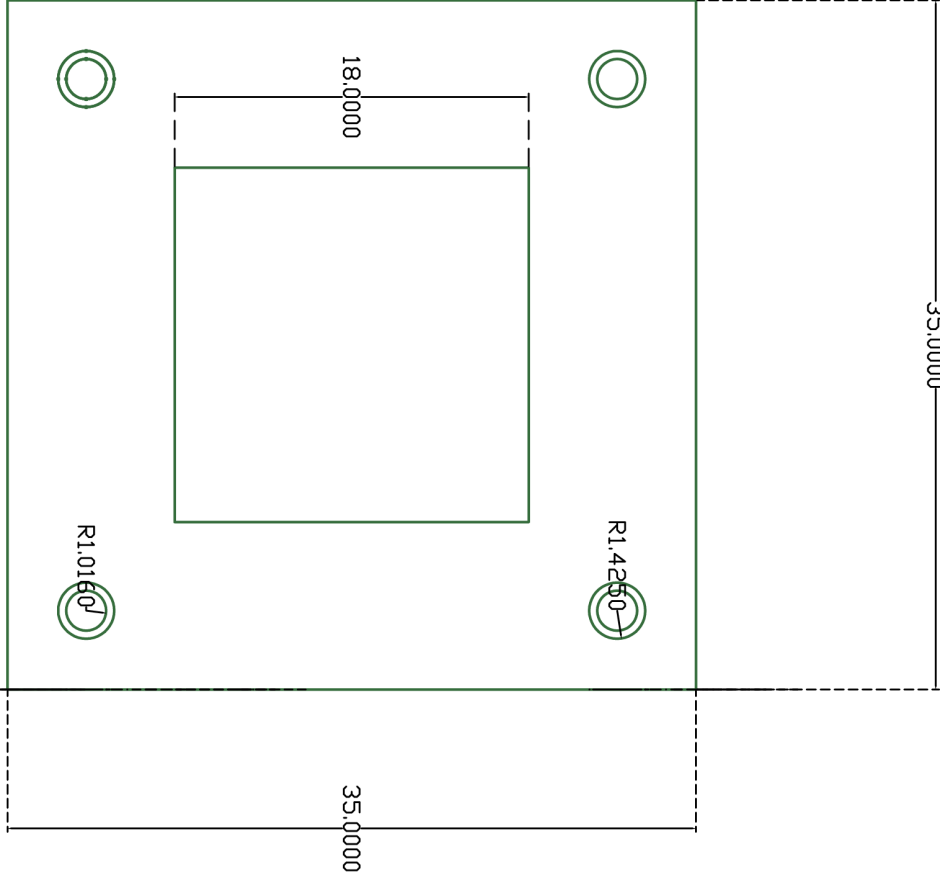
Top View



Bottom View



# Bottom Piece - Top Annotation



# Bottom Piece - Side Annotation

